October 2024

INTERNATIONAL STUDIES AND EVALUATIONS IN THE FIELD OF

ENGINEERING

EDITOR

PROF. DR. SELAHATTİN BARDAK

SERÜVEN YAYINEVİ

Genel Yayın Yönetmeni / Editor in Chief • C. Cansın Selin Temana

Kapak & İç Tasarım / Cover & Interior Design • Serüven Yayınevi

Birinci Basım / First Edition • © Ekim 2024

ISBN • 978-625-6172-44-9

Serüven Yayınevi / Serüven Publishing
Türkiye Adres / Turkey Address: Kızılay Mah. Fevzi Çakmak 1. Sokak
Ümit Apt No: 22/A Çankaya/ANKARA
Telefon / Phone: 05437675765
web: www.seruvenyayinevi.com
e-mail: seruvenyayinevi@gmail.com

Baskı & Cilt / Printing & Volume
Sertifika / Certificate No: 47083

NTERNATIONAL STUDIES AND EVALUATIONS IN THE FIELD OF ENGINEERING

October 2024

Editör

PROF. DR. SELAHATTİN BARDAK

CONTENTS

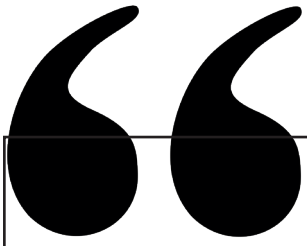

Chapter 1

SURROGATE BASED DESIGN OPTIMIZATION OF MULTIBAND ANTENNA FOR RF HARVESTING APPLICAITON

***Tarlan MAHOUTI*[1]**

***Merih PALANDÖKEN*[2]**

***Mehmet Ali BELEN*[3]**

1 Tarlan Mahouti, Yıldız Teknik University, https://orcid.org/0000-0001-5178-4878, tarlan.mahouti@gmail.com

2 Prof. Dr. Merih Palandöken, İzmir Katip Çelebi University, https://orcid.org/0000-0003-3487-2467, merih.palandoken@ikc.edu.tr

3 Assoc. Prof. Dr. Mehmet Ali Belen, İskenderun Teknik University, https://orcid.org/0000-0001-5588-9407, mali.belen@iste.edu.tr

INTRODUCTION

The rapid proliferation of wireless communication technologies and the Internet of Things (IoT) has underscored the critical need for sustainable power solutions. In response to this demand, Radio Frequency (RF) energy harvesting systems have emerged as a pivotal technology, offering a promising solution to the power challenges associated with energy-constrained electronic devices[1]. RF energy harvesting involves the conversion of ambient electromagnetic radiation into electrical power, providing a continuous and renewable energy source for wireless sensor networks, IoT devices, and other low-power electronic systems. This technology is particularly significant in scenarios where traditional power solutions are either impractical or prohibitively expensive. The ability to harvest RF energy from the environment not only reduces dependence on conventional power sources but also extends the operational life of battery-powered devices, contributing to the sustainability of wireless communication technologies. [2-3]

As the IoT continues to expand and the demand for efficient RF energy harvesting systems grows, multiband antennas have become integral components of these systems. These antennas enable energy capture across various frequency spectrums, enhance adaptability to different environments, and support multiple wireless communication standards [4-6]. In the dynamic landscape of wireless communication, multiband antennas allow devices to operate across multiple frequency bands, supporting a wide range of applications from mobile communication to radar and satellite systems, and most notably, RF energy harvesting systems. [7].

However, the design and optimization of such antennas present significant challenges. The need to balance performance across different frequency bands introduces a complex engineering problem, with each band imposing its own requirements in terms of gain, bandwidth, efficiency, and size [8-11]. These inherently conflicting parameters transform the design of multiband antennas into a sophisticated, multi-objective optimization problem. Traditional modeling approaches often struggle to capture the intricate interactions between these constraints, leading to designs that perform well in some bands but poorly in others.

The integration of artificial intelligence (AI) in antenna design has revolutionized the field, enabling more efficient and accurate design processes. AI techniques, particularly machine learning algorithms, have been increasingly applied to optimize antenna designs by predicting performance metrics based on design parameters[12].

This approach reduces the dependency on time-consuming electromagnetic simulations, allowing for rapid exploration of the design space. Several AI-based methods have been successfully employed in antenna design, including:

1. **Multilayer Perceptron (MLP)**: A type of artificial neural network that consists of multiple layers of neurons. MLPs are particularly effective in modeling complex nonlinear relationships between antenna parameters and performance metrics, making them suitable for optimizing multiband antennas[13].

2. **Support Vector Regression Machine (SVRM)**: SVRM is a powerful machine learning technique that aims to find a regression model that best fits the data while maintaining a balance between model complexity and prediction accuracy. It has been used in antenna design for predicting performance measures such as gain and bandwidth[14].

3. **Gradient Boosted Trees (GBT)**: This ensemble learning method combines the predictions of several decision trees to improve the overall accuracy. GBT has been applied in the optimization of antenna arrays, where it effectively handles the nonlinearities and interactions between design variables[15].

4. **Deep Neural Network Regressor (DNNR)**: DNNRs leverage deep learning architectures to model complex functions. In antenna design, deep neural networks can learn intricate patterns in large datasets, making them well-suited for optimizing antennas across multiple performance criteria[16].

5. **Gaussian Process Regression (GPR)**: GPR is a non-parametric, probabilistic model that is particularly useful for capturing the uncertainty in predictions. It provides a flexible approach for modeling the relationship between design variables and antenna performance, allowing for robust optimization[17].

6. **Modified Multilayer Perceptron**: The M2LP is an enhanced version of the traditional MLP, incorporating modifications that improve its convergence speed and accuracy. This model is particularly effective in complex optimization problems, such as those encountered in the design of multiband antennas[18].

In addition to AI techniques, optimization algorithms play a crucial role in the design process, particularly in navigating the complex, multi-dimensional search spaces associated with antenna design[19]. Optimization algorithms are used to systematically explore these spaces, identify optimal solutions, and balance multiple performance criteria.

One of the optimization algorithms utilized in this work is the **Honey Bee Mating Optimization (HBMO)** algorithm. HBMO [20]is a nature-inspired algorithm that mimics the natural mating process of honey bees. The algorithm is based on the concepts of queen bee mating, where the queen mates with a number of drones to produce a diverse offspring. The best solutions are selected based on their fitness, and these solutions are used to guide the search process in subsequent generations.

The HBMO algorithm operates in several stages:

1. Mating Flight: The queen bee selects drones (potential solutions) to mate with based on their fitness levels. Drones with higher fitness have a greater probability of mating with the queen.

2. Brood Production: The queen produces broods (new solutions) through crossover and mutation of the selected drones' genetic material. This process introduces diversity into the population and helps explore new areas of the design space.

3. Worker Bees: Worker bees (local search algorithms) are employed to refine the solutions within the neighborhood of the brood, improving their quality.

4. Natural Selection: The best broods (solutions) are selected to form the next generation, ensuring that the population evolves towards better solutions over time.

The HBMO algorithm is particularly effective in solving multi-objective optimization problems, as it balances exploration and exploitation of the search space, allowing it to identify high-quality solutions that satisfy multiple performance criteria[21].

Approaching multiband antenna design as a multi-objective optimization problem offers a promising pathway to overcoming these obstacles. Multi-objective optimization involves simultaneously optimizing two or more conflicting objectives, a scenario emblematic of the multiband antenna design process[22]. The objectives in this context may range from maximizing antenna gain and bandwidth in each operational band to minimizing size and cost. The challenge lies in identifying design configurations that offer the best trade-offs among these diverse and often competing objectives.

The emergence of advanced computational techniques and surrogate modeling has opened new horizons in the modeling and optimization of multiband antennas. Surrogate models provide a way to reduce the computational complexity associated with direct simulations, enabling faster and more efficient exploration of the design space[23]. When combined with advanced multi-objective optimization algorithms like HBMO, these models can scan vast design spaces to identify optimal or near-optimal antenna designs that balance different performance metrics.

The aim of this work is to develop and validate a computationally efficient optimization framework for the design of multiband antennas in RF energy harvesting systems, leveraging advanced surrogate modeling techniques and meta-heuristic algorithms to enhance antenna performance across multiple frequency bands. This study encompasses the application of artificial

intelligence-supported surrogate models, particularly the Modified Multilayer Perceptron (M2LP), in combination with the Honey Bee Mating Optimization (HBMO) algorithm, to address the complex, multi-objective challenges of antenna design. The work includes detailed analysis and optimization processes to improve the efficiency and sustainability of RF energy harvesting technologies, with a focus on reducing computational costs while maintaining high accuracy in antenna performance predictions.

The study is structured as follows: In Section 2, we define the antenna and the range of variables considered. In Section 3, we describe the artificial intelligence-based surrogate modeling process used to optimize the antenna design, focusing on methods such as MLP, SVRM, GBT, DNNR, GPR, and M2LP, as well as the HBMO optimization algorithm. The study concludes with a discussion of the results, highlighting the potential of this approach to contribute to the sustainability and advancement of wireless communication technologies through more efficient RF energy harvesting systems.

ANTENNA DESIGN AND DATA PREPARATION

The antenna structure presented in Figure 1 is proposed as a multi-band solution for RF energy harvesting circuits. The design variables are listed in Table 1. Each of these variables significantly impacts the scattering characteristics of the antenna structure, making the optimal selection of these parameters a critical optimization problem. As discussed in the previous section, artificial intelligence-based surrogate modeling techniques are among the most effective methods in the literature for executing this process efficiently and with high performance. Within the range of variables presented in Table 1, a total of 1000 antenna designs (800 for training and 200 for testing) with various geometries were prepared using 3D simulators and the Latin-Hypercube sampling method [24]. In these simulations, the scattering parameter of the antenna was analyzed in the 0.1-10 GHz band, with the geometric variables and frequency information of the antenna serving as inputs to the surrogate models, while the scattering parameter characteristic was the model's output. The subsequent sections of the study present the development and results of data-driven surrogate models based on this dataset.

Table I. Variables And Range Of The Antenna Considered In [Mm].

Değişken	Minimum	maksimum
W1	1	6
W2	0.5	3
W3	0.5	3
L1	5	15
L2	5	20

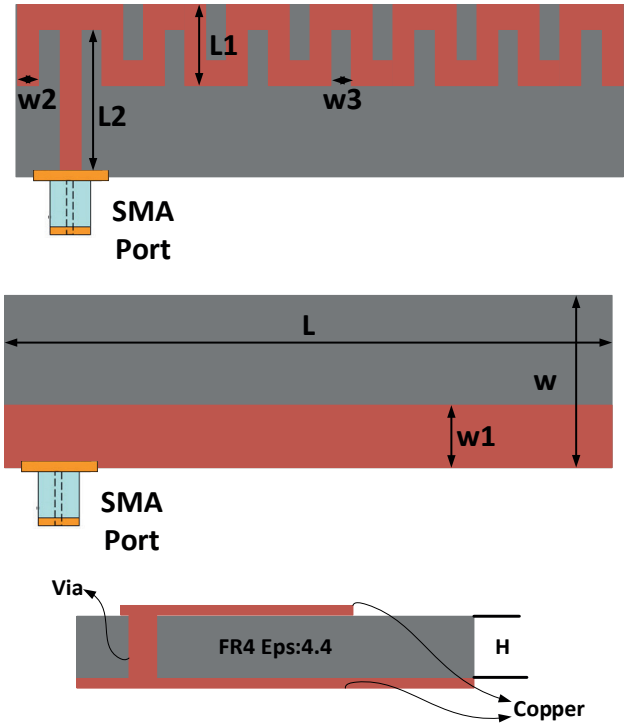

Figure. 1. Schematic images of the examined antenna

MODELING AND SIMULATION RESULTS

The design and optimization of microwave antennas is a critical field, driven by the ever-increasing demand for higher performance in communication systems. This process is characterized by the complexity of microwave antenna design, which involves a large parameter space and nonlinear interactions between design variables. The adoption of advanced computational techniques is essential. Data-driven surrogate modeling has emerged as a powerful tool, offering a practical balance between computational efficiency and modeling accuracy. Traditional full-wave electromagnetic simulations, while accurate, are computationally intensive and time-consuming, making them impractical for extensive parameter scans or optimization studies. This is where surrogate modeling—developing a simplified model that approximates the behavior of a complex system—becomes invaluable. Surrogate models utilizing data-driven approaches can accurately predict antenna performance across a wide range of design parameters with significantly reduced computational overhead. Data-driven surrogate modeling involves using machine learning and statistical techniques to create mathematical models that learn from simulation data. Once trained, these models can act as a surrogate for more complex full-wave simulations, enabling rapid exploration of the design space and optimization

of antenna parameters. Techniques such as polynomial regression, Gaussian processes, and neural networks have been at the forefront of surrogate model development, each offering unique advantages in terms of modeling accuracy, interpretability, and computational requirements.

In this study, various artificial intelligence algorithms were examined, and a surrogate model was developed for the antenna design presented in Section 2. The algorithms listed in Table 2 were employed for this purpose. The cross-validation technique (K=3) was used to select the hyperparameters of the models, utilizing 800 training data points generated in Section 2. The final performance evaluations of the models were conducted using 200 data points generated in the previous section.

Table 2 lists the state-of-the-art regression algorithms widely used in the literature: (i) Multilayer Perceptron (MLP) [25], (ii) Support Vector Regression Machine (SVRM) [26], (iii) Gradient Boosted Tree (GBT) [27], (iv) Deep Neural Network Regressor (DNNR) [28], (v) Gaussian Process Regression (GPR) [29], and (vi) Modified Multilayer Perceptron (M2LP) [30], which have been investigated in this study. The performance of the models was evaluated using relative absolute error. As a result, the M2LP model was found to be the most successful method.

Table II. Design Values In [Mm].

Model	**Model Parametreleri**	**Test Başarımı**
MLP	Two layers, 25 and 45 neurons	%7.4
SVRM	Epsilon = 0.1, Radial basis function	%8.9
GBT	Learning rate 0.001, 5000 estimators, and depth 4	%8.1
DNNR	3 Layers: 256, 512, 1024 neurons	%7.6
GSR	Kernel function: "ard-matern3/2", Prediction method: "Block coordinate descent", Block size: 1000	%6.9
M2LP	Depth 3, Initial number of neurons: 16	%4.7

In this study, the Honey Bee Mating Optimization (HBMO) algorithm [31], a population-based meta-heuristic optimization technique, is employed in conjunction with the M2LP surrogate model to identify the optimal design variables for the proposed multi-band antenna. The search process within the HBMO algorithm is guided by the cost function defined in Equation 1.

$$\text{Cost} = \sum_{f_{\min_1}}^{f_{\max_1}} \frac{C_1}{\left|S_{11_i}(f)\right|} + \sum_{f_{\min_2}}^{f_{\max_2}} \frac{C_2}{\left|S_{11_i}(f)\right|} \tag{1}$$

In this context, the C values represent the weight coefficients of the cost function sub-criteria. In this study, because the importance of each band is considered equal, these coefficients are assigned equal values. The objective

is to maximize the S11 values within the specified frequency ranges. Table III presents the most appropriately selected design variables obtained from the HBMO algorithm.

Table III. Optimum Design Values of the Structure Optimized By Surrogate Modeling In [Mm].

W1	4.5	W3	1.2
W2	1.5	L1	6.2
L2	11.5	FR4	Eps 4.6 h 1.56

To verify the accuracy of the optimized antenna design, the obtained results were input into the 3D simulator tool, and the following performance outputs were obtained.

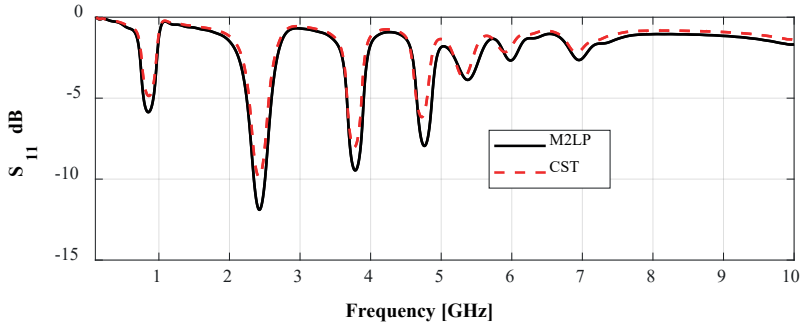

(a)

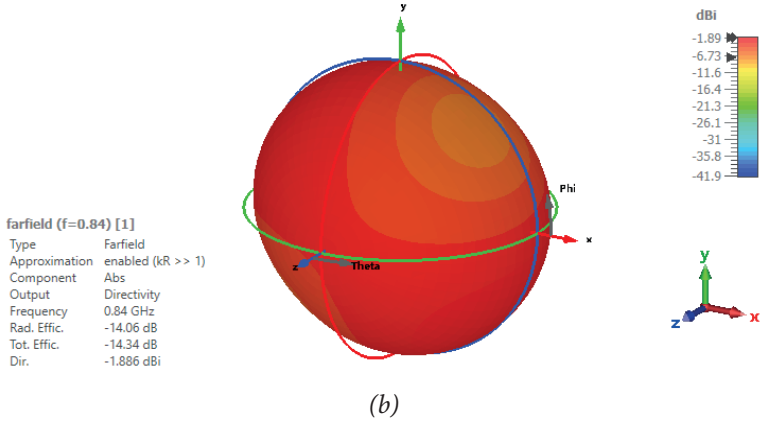

(b)

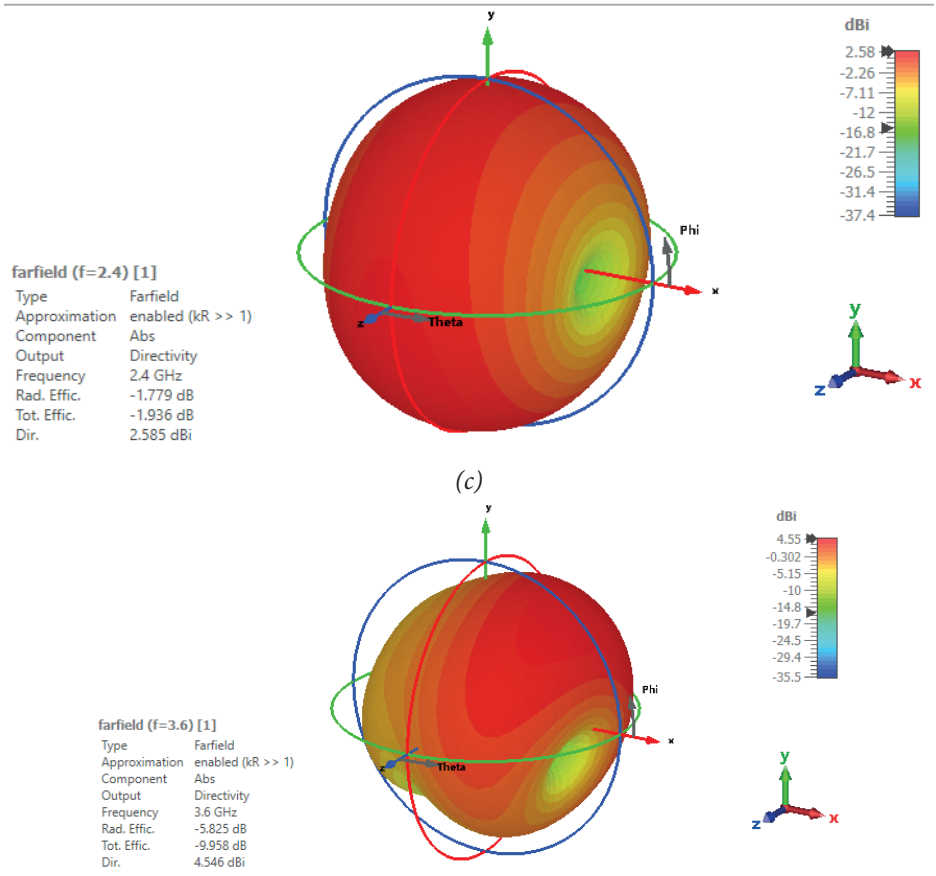

Fig. 2. Simulated 3D radiation pattern of the optimum antenna (a) S_{11}, (b) 868 MHz, (c) 2.4 GHz, (d) 3.6 GHz.

CONCLUSION

In this study, a computationally efficient design optimization process for a multi-band microstrip antenna was successfully demonstrated using a novel approach that integrates the M2LP regression model with the Honey Bee Mating Optimization (HBMO) algorithm. The optimization process aimed to maximize the S11 values across specified frequency ranges, treating each band with equal importance. The accuracy of the optimized design was validated through 3D simulations, which confirmed the effectiveness of the proposed method.

The study compared various state-of-the-art regression models, including Multilayer Perceptron (MLP), Support Vector Regression Machine (SVRM), Gradient Boosted Trees (GBT), Deep Neural Network Regressor (DNNR), Gaussian Process Regression (GPR), and the Modified Multilayer Perceptron

(M2LP). Among these, the M2LP model, characterized by its depth of 3 and an initial neuron count of 16, outperformed the others, achieving the lowest test error rate of 4.7%. This highlights the M2LP model's robustness in handling the complexities associated with multi-band antenna design.

In summary, the combination of the M2LP model and the HBMO algorithm provides a powerful and computationally efficient framework for optimizing complex antenna designs, offering a significant reduction in computational overhead while maintaining high accuracy. This approach holds promise for further applications in advanced antenna design and other related fields.

ACKNOWLEDGMENTS

This study was supported by TÜBİTAK (The Scientific and Technological Research Council of Türkiye) Project 121N412.

REFERENCES

1. L. Ramalingam et al., "The Advancement of Radio Frequency Energy Harvesters (RFEHs) as a Revolutionary Approach for Solving Energy Crisis in Wireless Communication Devices: A Review," IEEE Access, vol. 9, pp. 106107-106139, 2021, doi: 10.1109/ACCESS.2021.3098895.
2. K., Veronique, C. Lahuec, F. Seguin, and C. Person, "A multi-band stacked RF energy harvester with RF-to-DC efficiency up to 84%," IEEE transactions on microwave theory and techniques, vol 63, no. 5, pp. 1768-1778, 2015.
3. S. Keyrouz, H. J. Visser, and A. G. Tijhuis, "Multi-band simultaneous radio frequency energy harvesting," In 2013 7th European Conference on Antennas and Propagation (EuCAP), pp. 3058-3061, 2013.
4. V. Hosseini, F. Yousef, M. Kambiz, and G. Changiz, "Multi-objective hybrid optimization algorithm for design a printed MIMO antenna with n78-5G NR frequency band applications," IEEE Access (2023).
5. K. Suriyan, R. Nagarajan, and G. Ghinea, "Smart Antenna Optimization Techniques for Wireless Applications," Electronics, vol. 12, no. 13, 2023.
6. F. Fouad, K. Fertas, T. A. Denidni, and M. Challal, "Design of miniaturized triband antenna based on differential evolution algorithm," Microwave and Optical Technology Letters, vol. 65, no. 3, pp. 930-935, 2023.
7. S. Kannadhasan, R. Nagarajan, and V. Kanagaraj, "Performance, Metrics, and Challenges of Multiband Antenna for Wireless Communication," In 2022 6th International Conference on Trends in Electronics and Informatics (ICOEI), pp. 478-481, 2022.
8. B. Liu, M. O. Akinsolu, C.haoyun Song, Q. Hua, P. Excell, Q. Xu, Y. Huang, and M. A. Imran, "An efficient method for complex antenna design based on a self adaptive surrogate model-assisted optimization technique," IEEE Transactions on Antennas and Propagation, vol. 69, no. 4 2302-2315,2021.
9. A. Belen, Ö. Tarı, P. Mahouti, M. A. Belen, and A. Caliskan, "Surrogate-based design optimization of multi-band antenna," Applied Computational Electromagnetics Society Journal 2022.
10. O. C. Piltan, A. Kizilay, M. A. Belen, and P. Mahouti, "Data driven surrogate modeling of horn antennas for optimal determination of radiation pattern and size using deep learning," Microwave and Optical Technology Letters, vol. 66, no. 1 2024.
11. B. Yuming, P. Gardner, Y. He, and H. Sun, "A Surrogate Modeling Approach for Frequency Reconfigurable Antennas," IEEE Transactions on Antennas and Propagation 2023.
12. Sarker, N., Podder, P., Mondal, M. R. H., Shafin, S. S., & Kamruzzaman, J. (2023). Applications of Machine Learning and Deep Learning in Antenna Design, Optimization and Selection: A Review. *IEEE Access*. **DOI:** 10.1109/ACCESS.2023.3317371

13. Costa, L., Guerreiro, M., Puchta, E., de Souza Tadano, Y., Alves, T. A., Kaster, M., & Siqueira, H. V. (2023). Multilayer perceptron. *Introduction to Computational Intelligence*, *105*.

14. Velasco, L. C., Estose, A. J., Opon, M., Tabanao, E., & Apdian, F. (2024). Performance Evaluation of Support Vector Regression Machine Models in Water Level Forecasting. *Procedia Computer Science*, *234*, 436-447. https://doi.org/10.1016/j.procs.2024.03.025

15. Zhang, Z. H., Ye, Q., Fu, L., Wang, J. Q., Guo-Xiang, M., & Shen, Z. Q. (2022). Rapid deformation calculation for large reflector antennas: a surrogate model method. *Research in Astronomy and Astrophysics*, *23*(1), 015001.

16. Nguyen, T. V., Huynh-The, T., & Nguyen, T. H. (2023, October). A Deep CNN Design for Secure Short-Packet Communications in WET IoT Networks with Multiple Eavesdroppers. In *2023 International Conference on Advanced Technologies for Communications (ATC)* (pp. 521-526). IEEE. **DOI:** 10.1109/ATC58710.2023.10318924

17. Yurt, R., Torpi, H., Kizilay, A., Koziel, S., Pietrenko-Dabrowska, A., & Mahouti, P. (2023). Buried object characterization by data-driven surrogates and regression-enabled hyperbolic signature extraction. *Scientific Reports*, *13*(1), 5717. https://doi.org/10.1038/s41598-023-32925-6

18. Calik, N., Albayrak, A., Akhan, A., Turkmen, I., Capar, A., Toreyin, B. U., ... & Durak-Ata, L. (2022). Classification of cervical precursor lesions via local histogram and cell morphometric features. *IEEE Journal of Biomedical and Health Informatics*, *27*(4), 1747-1757. **DOI:** 10.1109/JBHI.2022.3218293

19. Devisasi Kala, D. D., & Sundari, D. T. (2023). A review on optimization of antenna array by evolutionary optimization techniques. *International Journal of Intelligent Unmanned Systems*, *11*(1), 151-165. https://doi.org/10.1108/IJIUS-08-2021-0093

20. Piltan, O. C., Kizilay, A., Belen, M. A., & Mahouti, P. (2024). Data driven surrogate modeling of horn antennas for optimal determination of radiation pattern and size using deep learning. *Microwave and Optical Technology Letters*, *66*(1), e33702. **https://doi.org/10.1002/mop.33702**

21. Mahouti, P., Kīzīlay, A., Razevig, V. V., Belen, M. A., & Piltan, O. C. (2023, June). Vivaldi Antenna Design With Frequency Selective Surfaces for GPR Applications. In *2023 10th International Conference on Recent Advances in Air and Space Technologies (RAST)* (pp. 1-4). IEEE. **DOI:** 10.1109/RAST57548.2023.10197899

22. de Curtò, J., de Zarzà, I., & Calafate, C. T. (2023). UWB and MB-OFDM for Lunar Rover Navigation and Communication. *Mathematics*, *11*(18), 3835. **https://doi.org/10.3390/math11183835**

23. Koziel, S., & Pietrenko-Dabrowska, A. (2022). Fundamentals of data-driven surrogate modeling. In *Surrogate Modeling For High-frequency Design: Recent Advances* (pp. 1-37). https://doi.org/10.1142/9781800610750_0001

24. L. Wei-Liem. "On Latin hypercube sampling." The annals of statistics 24, no. 5, pp. 2058-2080, 1996.

25. A. Uluslu, "Application of Artificial Neural Network Base Enhanced MLP Model for Scattering Parameter Prediction of Dual-band Helical Antenna," Applied Computational Electromagnetics Society Journal, vol. 38, no.5, 2021.

26. D. R. Prado, J. A. Lopez-Fernandez, M. Arrebola, and G. Goussetis, "Support vector regression to accelerate design and crosspolar optimization of shaped-beam reflectarray antennas for space applications," IEEE Transactions on Antennas and Propagation, vol. 67, no.3, 1659-1668, 2018.

27. R. Sun, G. Wang, W. Zhang, L.-T. Hsu, and W. Y. Ochieng., "A gradient boosting decision tree based GPS signal reception classification algorithm," Applied Soft Computing vol. 86, 2020.

28. S. G. Cha, K. Donghyun, and Y. J. Yoon, "Compact Amplitude-Only Direction Finding Based on a Deep Neural Network with a Single-Patch Multi-Beam Antenna," Applied Sciences, vol.13, no. 12, 2023.

29. Z. Xie, F. Meng, Y. Tian, and X. Zhang, "Design of monopole antennas based on progressive Gaussian process," International Journal of Microwave and Wireless Technologies, vol.15, no. 2, pp. 255-262, 2023.

30. N. Calik, M. A. Belen, and P. Mahouti, "Deep learning base modified MLP model for precise scattering parameter prediction of capacitive feed antenna," International journal of numerical modelling: electronic networks, devices and fields, vol. 33, no. 2, 2020.

31. F. Güneş, İ. Ö. Evranos, M. A. Belen, P. Mahouti, and M. Palandöken, "A compact triband antipodal vivaldi antenna with frequency selective surface inspired director for IoT/WLAN applications," Wireless Networks 27, no. 5, pp 3195-3205, 2021.

Chapter 2

EFFECT OF INJECTION TIMING ON EMISSION FORMATION IN STRATIFIED CHARGE ENGINES

Müjdat FIRAT[1]

Ömer Faruk AKÇİL[2]

Cengiz ÖNER[3]

1 Doç. Dr., Fırat Üniversitesi, Teknoloji Fakültesi, Otomotiv Mühendisliği Bölümü, Elazığ, Türkiye

2 Ömer Faruk AKÇİL, Fırat Üniversitesi, Teknoloji Fakültesi, Otomotiv Mühendisliği Bölümü, Elazığ, Türkiye, omerfarukakcil@gmail.com

3 Prof.Dr. Cengiz ÖNER, Bingöl Universitesi Mühendislik-Mimarlık Fakültesi Makine Mühendisliği, Bingöl,Türkiye (ORCID: 0000-0002-3278-2831), coner@bingol.edu.tr

1 Introduction

Today, due to the development of the automobile industry, limited fuel reserves and high emission values resulting from combustion, studies on the use of alternative fuels in internal combustion engines are increasing. Clean fuels such as natural gas, liquefied petroleum gas and hydrogen can be given as examples of these alternative fuels (Yang et al. 2023 and Lie et al.2023). Some countries stated that due to environmental pollution and fuel shortage, engines that use only gasoline and diesel as fuel may be banned in the following years (Zhang, 2020). In this context, sustainable methods continue to be developed and implemented in internal combustion engines. In this context, sustainable methods continue to be developed and implemented in internal combustion engines (Liu, 2023).

When energy resources are examined in terms of consumption, oil ranks first with 34.2%, coal ranks second with 27.6% and natural gas ranks third (Akbiyik, 2023).

The Environmental Protection Agency stated that natural gas could be a highly usable fuel in the future. Since the hydrogen/carbon value of natural gas is high, the particulate matter and CO2 emission values released as a result of combustion will be lower. Natural gas can also be obtained from renewable sources (Molina, 2023). If natural gas is obtained from a renewable source, the resulting carbon dioxide emission value will be more promising (Yousefi, 2020).

BP stated in its published reports that the demand for fuel consumption has increased significantly [A4] and announced that natural gas will be the fuel with the fastest growth rate among fossil fuels in 2022. It has been observed that natural gas has lower values both in terms of cost and nitrogen oxide emissions when compared to gasoline and diesel (Liu,2023 and Shen, 2023).

Internal combustion engines are manufactured to run on gasoline or diesel. These engines can be modified and run on alternative fuels such as liquefied petroleum gas (LPG) and compressed natural gas (CNG). CNG is superior to liquid fuels such as gasoline and diesel due to its many properties (Ziyaei, 2023).

Some of these properties are the engine performance and exhaust emission values of natural gas (Ramsay, 2022). In addition, since natural gas has high knock resistance, it is widely used in gasoline engines (Chen, 2021).

In short, Natural gas (NG) is a good alternative fuel due to its high octane number and hydrogen/carbon value, as well as low cost and exhaust emissions (Duan 2018).

Recently, a lot of research has been done on fuels and mixture formation, as well as the charge system structure, to increase engine performance. These

systems are structurally divided as; homogeneous charge and stratified charge. In homogeneous charge, the aim is to mix the fuel with air in the intake manifold and spread it evenly into the cylinder. Stratified charge aims to obtain a stoichiometric mixture in the spark plug region of the cylinder as it moves away from the spark plug, and a lean mixture in the other parts. In this way, Stratified charge engines can be operated with lean mixture, just like diesel engines. A decrease in nitrogen oxide, carbon dioxide and unburned hydrocarbon emission values was observed in the gradual filling method applied in gasoline engines (Jubin, 2022).

Duan et al. (2018) experimentally examined the effects of single injection and two injection strategies on the thermodynamic process and engine performance in the case of ethanol-gasoline mixture as fuel in a direct injection gasoline engine. Under single injection conditions, an injection timing starting at 300 CA BTDC and lasting 18.5 CA was selected. Then, in six different injection timings, without changing the location of the first injection, different injection timings closer to top dead center were selected as the second injection. In the experimental system, an electric dynamometer was used to control fuel consumption and fuel temperature, and all obtained data were transferred to the combustion analysis system and converted into engine data. As a result of the study, it was seen that cylinder pressure and heat release were affected by single and dual injection strategies. It was also emphasized that HC and CO emissions decreased in the case of double injection, but this decrease depended on the time of the second injection.

Oh and Bae (2013) examined the effects of injection time on injection and combustion characteristics in a direct injection spark ignition engine under gradual charging conditions. In the study, two different ambient pressures and three different injection pressures were tested under stratified charge conditions. While Non-luminous flame structure and low combustion efficiency were observed in the early injection timing, luminous flame structures were observed in the late injection timing. In addition, an increase in soot emissions and incomplete combustion products was observed due to locally increasing rich mixture regions at late injection timings It has also been shown that NOx emissions are directly dependent on injection timing.

Aljamali et al. (2016) examined the effect of injection timing on engine performance and emissions in a stratified charged engine. In the experimental study, they used CNG as fuel. Four different injection timings (120 CA, 180 CA, 300 CA, 360 CA BTDC) were used in the study, where the end of the injection was taken as reference. Experimental results are presented in graphs, including torque, specific fuel consumption, average effective pressure, CO, CO_2, NO and HC. In the study, the highest power, torque, average effective pressure and lowest specific fuel consumption were obtained at 120 CA injection timing. In addition, the lowest NO and HC emissions were obtained

at 120 CA injection timing, while CO_2 emissions increased depending on the number of cycles.

The way fuel is sent to the cylinder is important in studies aimed at increasing engine efficiency. One of these is the stratified injection of fuel into the cylinder. In this study, the effects of second-stage injection timing on engine performance and emissions in a stratified charge engine with direct injection fueled natural gas were investigated.

2. Material and methods

The three-dimensional simulation program ANSYS-Forte 19.0 (ANSYS Forte User's Guide. And ANSYS Forte Theory Manuel). was used to investigate combustion and emission characteristics. A port model was designed to give the closest results to reality, and CH_4, which constitutes the majority of natural gas, was chosen as the fuel to be injected from the injector. All tests were performed at wide open throttle position, with different second stage injection timing (220CA, 170CA, 120CA and 70CA BTDC). As a result of the examination, it was seen that the fuel injection timing in the second stage had a positive effect on engine performance, combustion efficiency and emissions (Akçil, Ö.F. 2018).

In order to better understand the stratified charge (SC) conditions and optimize the injection timing, the second injection timing was changed while keeping the first injection time constant. The injection timing and operating conditions determined for homogeneous charge (HC) and stratified charge (SC) conditions are shown in Fig. 2.1 and Table 2.1.

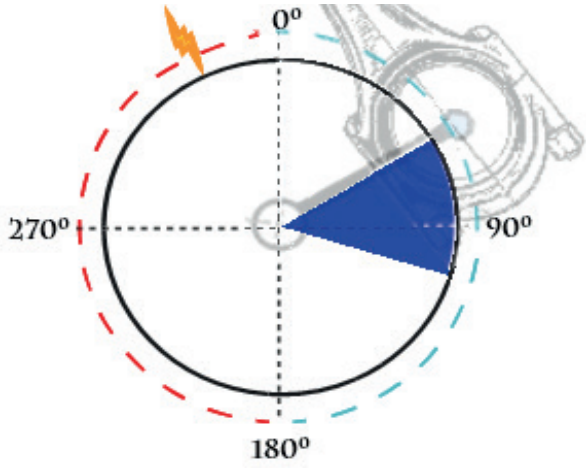

HC

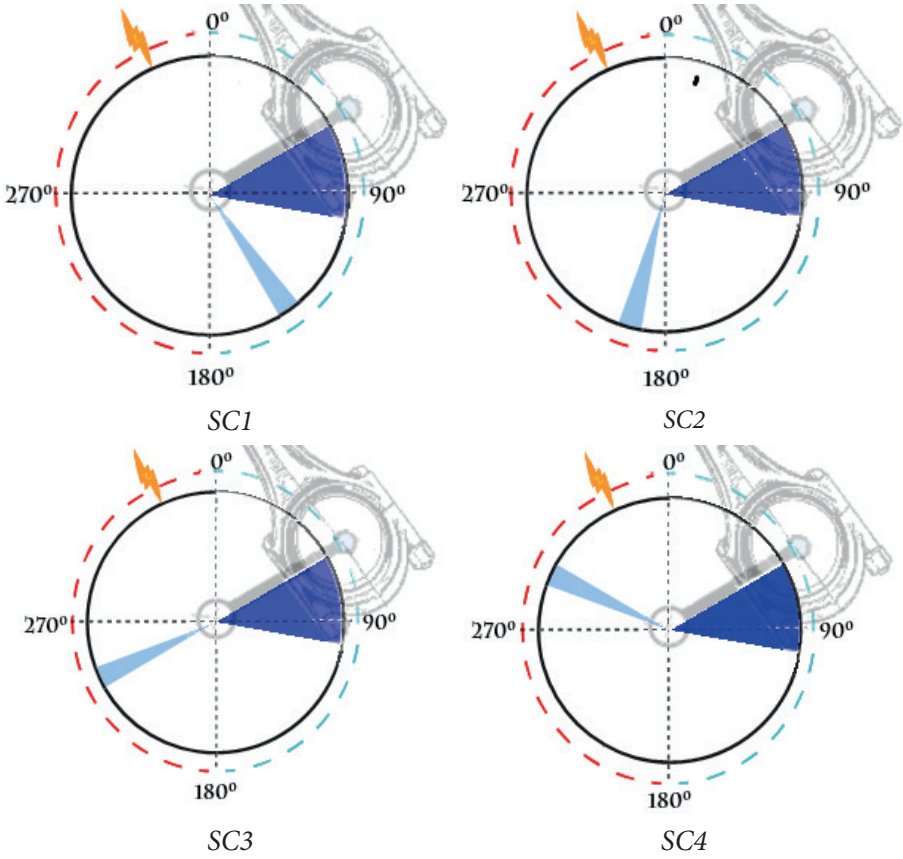

Fig.2.1. *Injection timing determined for homogeneous and stratified charge conditions.*

Table 2.1. Different injection timings and operating conditions.

Injection Type	First injection			Second injection			spark plug time	Lambda (λ)
HC	300CA BTDC	40CA	%100	---	---	---	35CA BTDC	1.4151
SC1	300CA BTDC	40CA	%85	220CA BTDC	10CA	%15	35CA BTDC	1.4211
SC2	300CA BTDC	40CA	%85	170CA BTDC	10CA	%15	35CA BTDC	1.4184
SC3	300CA BTDC	40CA	%85	120CA BTDC	10CA	%15	35CA BTDC	1.4310
SC4	300CA BTDC	40CA	%85	70CA BTDC	10CA	%15	35CA BTDC	1.4423

3. Research Findings and Discussion

The following findings were obtained in this study (Akçil, 2018). In a stratified charge engine, the ideal amount of fuel injected in each stage has been determined to create a generally lean mixture in the cylinder and a stoichiometric or rich mixture in the spark plug region. The crank angle at which the second injection will be made was investigated according to the ideal fuel ratio. Under these conditions, an analysis of a stratified charge direct injection gasoline engine using natural gas as fuel was performed. Although a lean mixture is generally preferred in stratified charge engines, a stoichiometric or rich mixture is intended in the spark plug area.

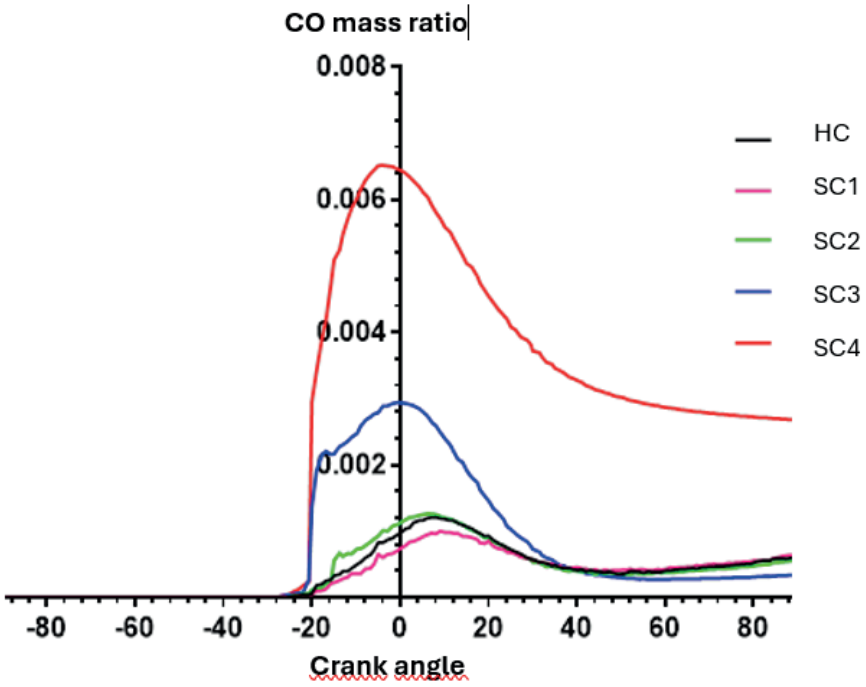

Fig. 3.1. *Changes in CO depending on different injection timings.*

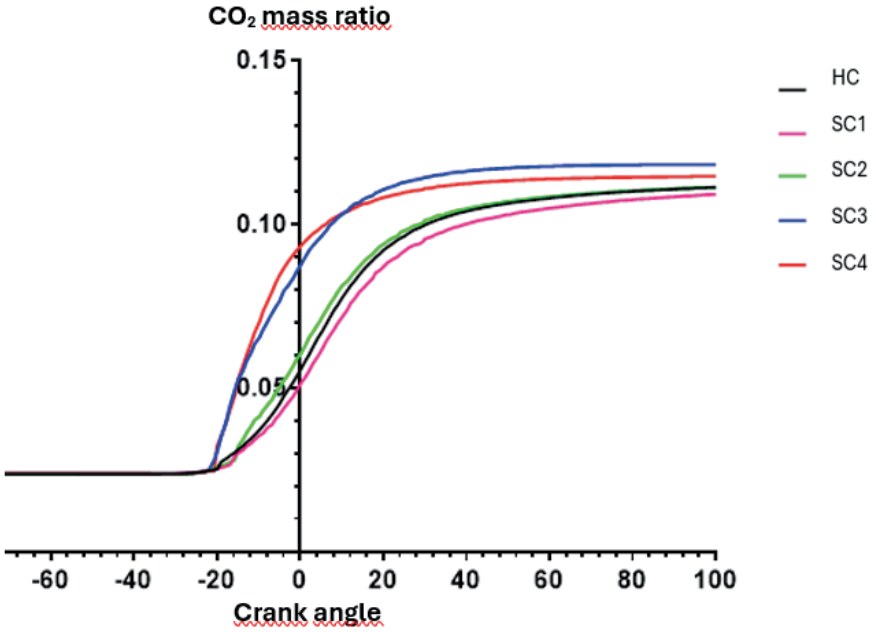

Fig. 3.2. *Changes in CO_2 depending on different injection timings.*

Fig. 3.1 and fig. 3.2 shows the changes in CO and CO2 emissions at each stage according to different injection times. CO emissions seen in Figure 3.1 increased with the start of combustion at all injection times and decreased with advancing crank angles. It is seen that the CO values are negligibly low. As can be seen in the figure, CO emissions are considerably increased near TDC at late injection timings. In late injection (SC3, SC4), CO emissions are expected to be lower due to higher temperatures. This may be a result of the fact that most of the fuel is burned near TDC and the heat release rate is very high. However, with the continuation of combustion, especially SC3 conditions reached the lowest CO emissions. It is understood that very late injection and high engine speed have an effect on CO values under SC4 conditions. CO2 emissions were slightly higher at late injection timings (Fig. 3.3). The higher CO2 emissions at late injection timings can be seen as a natural result of higher heat release rates and temperatures.

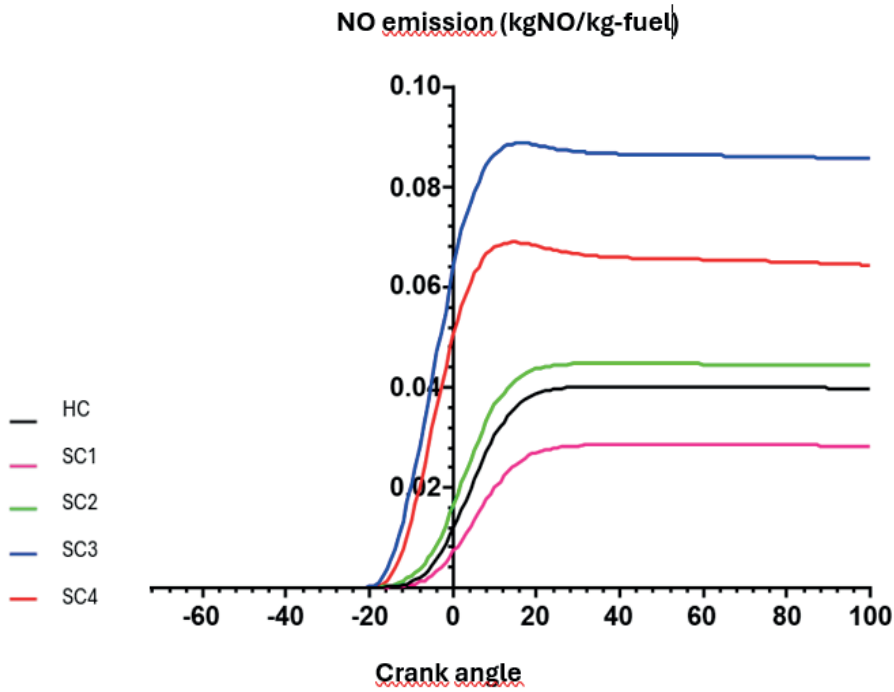

Fig. 3.3. *Change in NO emission depending on different injection timings.*

Fig. 3.3 shows in-cylinder NO emissions depending on different injection timings. It is known that NO formation is a function of in-cylinder temperature. In late injection cases, it is observed that the in-cylinder temperature is high. As a result, it is understood that NO emissions are also high. Since lower temperatures were observed during combustion at early injection timings, NO emission formation remained quite low due to the inability to provide the necessary reaction heat for NO formation.

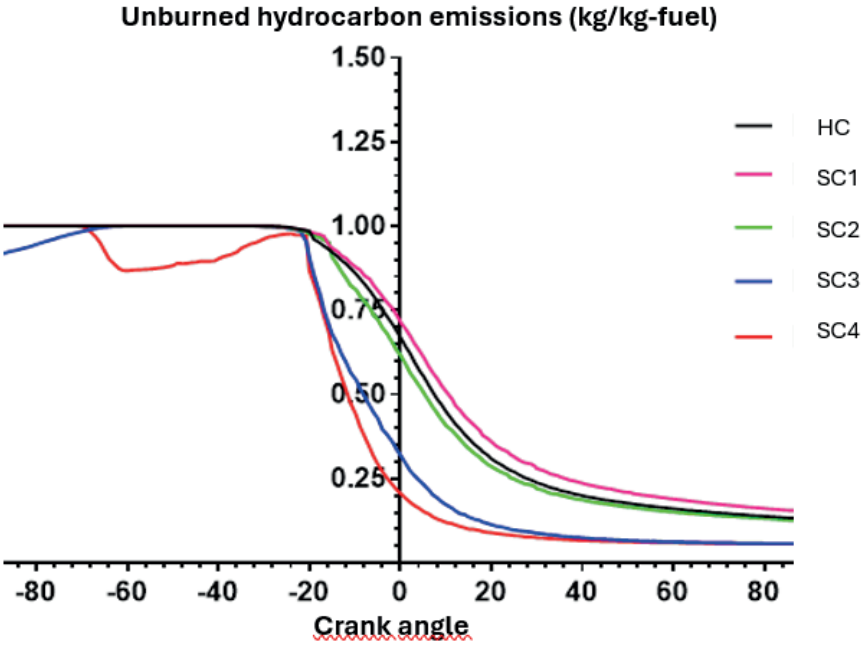

Figure 3.4. *Changes in unburned hydrocarbon emissions depending on different injection timings.*

In-cylinder unburned hydrocarbon emissions according to different injection timings are shown in Figure 3.4. The formation of unburned hydrocarbons is an undesirable emission component for internal combustion engines. It can be considered a criterion of good and complete combustion. In complete combustion, there is no HC in the emissions. HC, which can be burned with low hydrocarbon emissions, directly affects engine power. As can be seen in the figure, unburned hydrocarbon emissions decrease very rapidly in late injection cases, while they decrease more slowly in early injection timings and homogeneous cases. It can be put forward as an indication that in case of late injection, the combustion rate increases and the combustion efficiency increases. In general, similar and very low levels of unburned hydrocarbon emissions were obtained in all spraying cases.

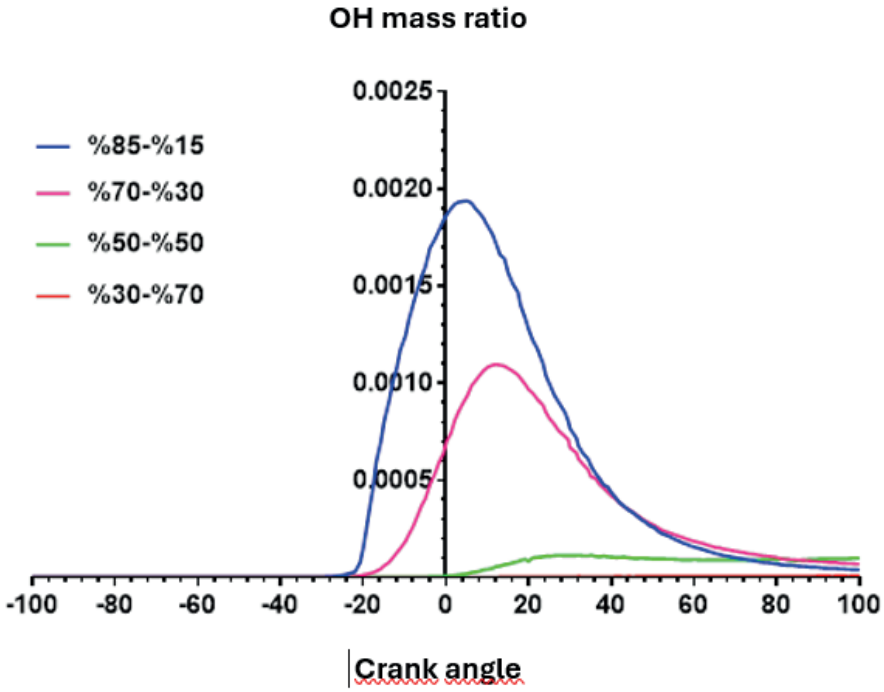

Fig. 3.5. *Variation of OH mass ratio with the amount of fuel injected at different stages.*

In order to follow the start and process of combustion in internal combustion engines, in-cylinder OH formation can be monitored. For this purpose, the formation of OH in the cylinder depending on the fuel rate injected in each stage is seen in Fig. 3.5. As seen in Fig. 3.5, in cases where less fuel was injected in the second stage, OH formation, i.e. combustion, started just before TDC and reached its maximum value just after TDC. However, in cases where less fuel was sent in the second injection, OH formation started much later than TDC. This situation shows that the crank angle and combustion efficiency at which combustion occurs are not appropriate when more fuel is sent in the second injection.

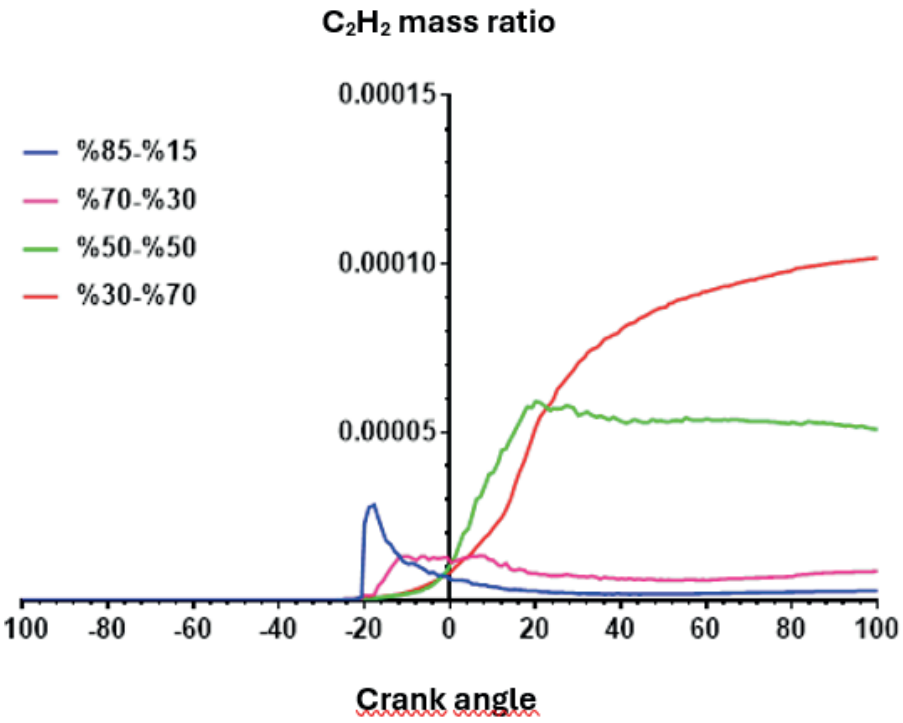

Fig. 3.6. *Variation of C_2H_2 mass ratio with the amount of fuel injected at different stages.*

For some chemical kinetic mechanisms used in internal combustion engines, soot emissions cannot be calculated directly. In this case, Ansys FORTE recommends monitoring C_2H_2, a leading product for monitoring soot emissions. Figure 3.6 shows the change in C_2H_2 depending on the fuel ratio injected in each injection. It is observed that C_2H_2 formation is quite low in cases where combustion occurs better and less fuel is sent in the second injection. However, in cases where more fuel was sent in the second injection, fuel particles that could not meet with oxygen molecules caused C_2H_2 to increase.

4. Conclusion

In this study, an analysis of a stratified charge direct injection gasoline engine using natural gas as fuel was carried out. In the study, firstly the best fuel ratio to be injected in each stage was determined for the staged filling conditions. The timing of the second injection was determined for optimum fuel injection ratios. Studies were carried out using ANSYS Forte software. As a result of the studies conducted, the following conclusions were reached.

For this study, better emission values were obtained under 85%-15% spray conditions. At late injection timings, CO emissions increased significantly

near TDC. However, as combustion continued, especially SC3 conditions reached the lowest CO emissions. Under SC4 conditions, CO emissions remained relatively high due to late injection and high engine speed. CO2 emissions were slightly higher at later injection times. Higher NO emissions were obtained at late injection timings depending on in-cylinder temperatures. From the OH curves, it is understood that combustion starts more quickly at late injection timings.

References

Zhang S., Li Y., Wang S., Zeng H., Liu J., Duan X., Dong H., 2020. Experimental and numerical study the effect of EGR strategies on in-cylinder flow, combustion and emissions characteristics in a heavy-duty higher CR lean-burn NGSI engine coupled with detail combustion mechanism, Fuel, Volume 276,118082

Liu J., Zhang X., Liu Y., Sun P., Ji Q., Wang X., Li Z., Ma H., 2023. Experimental study on in-cylinder combustion and exhaust emissions characteristics of natural gas/diesel dual-fuel engine with single injection and split injection strategies, Process Safety and Environmental Protection, Volume 172, Pages 225-240.

Akbiyik T., Kahraman N., Taner T., 2023. Energy and exergy analysis with emissions evaluation of a gasoline engine using different fuels, Fuel, Volume 345, 128189.

Molina S., Novella R., Gomez-Soriano J., Olcina-Girona M., 2023. Study on hydrogen substitution in a compressed natural gas spark-ignition passenger car engine, Energy Conversion and Management, Volume 291, 117259.

Yousefi A., Guo H., Birouk M., 2020. Split diesel injection effect on knocking of natural gas/diesel dual-fuel engine at high load conditions, Applied Energy 279 115828.

Liu J., Liu Y., Ji Q., Sun P., Zhang X., Wang X., Ma H. 2023**.** Effects of split injection strategy on combustion stability and GHG emissions characteristics of natural gas/diesel RCCI engine under high load, Energy, Volume 266, 126542.

Shen Z., Wang X., Zhao H., Lin B., Shen Y., Yang J., 2021. Numerical investigation of natural gas-diesel dual-fuel engine with different piston geometries and radial clearances, Energy ,Volume 220, 119706.

Siyamak Ziyaei, Siti Khalijah Mazlan, Petros Lappas, 2023 A Review of Ultra-lean and Stratified Charged Combustion in Natural Gas Spark Ignition Engines, RMIT University, Mechanical, Manufacturing and Mechatronic Engineering, Australia, RMIT University, Australia, 03-16-07-0050

Ramsay C.J., Ranga Dinesh K.K.J., High pressure direct injection of gaseous fuels using a discrete phase methodology for engine simulations, International Journal of Hydrogen Energy, Volume 47, Issue 3, Pages 2017-2039.

Chen Z., Zhang T., Wang X., Chen H., Geng L., Zhang T., 2021**.** comparative study of combustion performance and emissions of dual-fuel engines fueled with natural gas/methanol and natural gas/ gasoline, Energy Volume 237, 121586.

Duan X., Liu J., Tan Y., Luo B., Guo G., Wu Z., Liu W., Li Y., 2018. Influence of single injection and two-stagnation injection strategy on thermodynamic process and performance of a turbocharged direct-injection spark-ignition engine fuelled with ethanol and gasoline blend, *Applied Energy*, **228**, 942–953.

Jubin V. Jose, Mayank Mittal, A. Ramesh, Gutti Gnanakotaiah, Kuduva Shanthu Vishnukumar, Shrinidhi Shridhara, 2022. A Novel Combustion Chamber to Physically Stratify the Charge in a Gasoline Direct Injection Engine 03-16-03-0016.

Oh H., Bae C., 2013. Effects of the injection timing on spray and combustion characteristics in a pray-guided DISI engine under lean-stratified operation*, Fuel*, **107**, 225–235.

Aljamali S., Abdullah S., Wan Mahmood W. M. F., Ali Y., 2016. Effect of fuel injection timings on performance and emissions of stratified combustion CNGDI engine, *Applied Thermal Engineering,* **109**, 619–629.

Loyte A., Suryawanshi J., Bhiogade G., Devarajan Y., Raja T.,and Gavaskar T., 2023 Novel approach for efficient operation and reduced harmful emissions on a dual-fuel research engine propelled with hydrogen-enriched natural gas and diesel, Energy Sources, part a: Recovery, Utılızatıon, and Envıronmental Effects, vol. 45, no. 3, 8218–8238.

Akçil, Ö.F., 2018, Kademeli dolgulu bir benzinli motorda doğalgaz kullanımının motor performansına etkisinin incelenmesi, Fırat Üniversitesi Fen Bilimleri Enstitüsü, Yüksek Lisans Tezi

ANSYS Forte User's Guide.

ANSYS Forte Theory Manuel.

Chapter 3

ASSESSING THE ECONOMIC AND ECOLOGICAL FEASIBILITY OF SMALL RUN-OF-RIVER HYDROPOWER PLANTS

Metin YILMAZ[1]

Gamze YÜCEL IŞILDAR[2]

Saeed MORSALİ[3]

1 Metin YILMAZ, Ph.D., Gazi University, 0009-0008-9142-045
2 Gamze YÜCEL IŞILDAR, Prof. Dr., Gazi University, 0000-0001-8528-1806
3 Saeed MORSALİ, Research Associate, University of Turku, 0000-0002-8187-6084

* Not: Bu çalışma Metin YILMAZ tarafından, Gamze YÜCEL IŞILDAR danışmanlığında, Gazi Üniveristesi, FBE, Çevre Bilimleri ABD da, Temmuz 2024 de tamamlanan "NEHİR TİPİ HİDROELEKTRİK SANTRALLERİN YAPIM AŞAMASINDA FARKLI SENARYOLAR İÇİN ÇEVRESEL FAYDA MALİYET ANALİZLERİNİN KARŞILAŞTIRILMASI" başlıklı doktora tezinden üretilmiştir.

1. Introduction:

The raise of global climate change issues (Calvin et al., 2023), and energy prices has been resulted to exploring new and renewable energy sources. Energy is the basic of human socities and development is dependent to avalibility of energy in resaonable prices. Increasing in humankind population and industrialization has been lead to increase in energy demand. The world's demand for electricity is rising at its fastest rate in years, driven by robust economic growth, intense heatwaves and increasing uptake of technologies that run on electricity such as Electrical Vehicles (Evs) and heat pumps. At the same time, renewables continue their rapid ascent, with solar panels on course to set new records

Acording to the International Energy Agency (IEA) global electricity demand is forecast to grow by around 4% in 2024, up from 2.5% in 2023. This would represent the highest annual growth rate since 2007, excluding the exceptional rebounds seen in the wake of the global financial crisis and the COVID-19 pandemic. The strong increase in global electricity consumption is set to continue into 2025, with growth around 4% again, according to the report (International Energy Agency, 2024).

Renewable sources of electricity are also set to expand rapidly this year and next, with their share of global electricity supply forecast to rise from 30% in 2023 to 35% in 2025 (International Energy Agency, 2024). The amount of electricity generated by renewables worldwide in 2025 is forecast to eclipse the amount generated by coal for the first time. Solar PV alone is expected to meet roughly half of the growth in global electricity demand over 2024 and 2025 – with solar and wind combined meeting as much as three-quarters of the growth (International Energy Agency, 2024).

Amongst renewable electricity production systems, river-type small hydropower plants (SHPs) are run-of-river systems that generate electricity by diverting a portion of a river's flow through a turbine without the need for large reservoirs or dams. The economic and ecological feasibility of these projects has been evaluated in various reports, documents, and articles, comparing their advantages and limitations.

2. Methodology

This section provides and overview of some important aspects of HESs throughout the literature.

2.1. Economic Feasibility

Low Operational Costs: SHPs often have lower operational and maintenance costs compared to other renewable energy sources. The technology is mature, and once installed, these systems can operate for long

periods with minimal intervention (Kumar & Saini, 2022), (V. K. Singh & Singal, 2017).

Capital Costs: Initial investment costs for SHPs can be relatively high due to civil works, grid connection, and equipment. However, these costs are significantly lower compared to large hydropower or other forms of infrastructure-based energy sources. Projects are scalable depending on site-specific conditions (Forouzbakhsh et al., 2007), (Seme et al., 2018).

Energy Payback and Efficiency: SHPs have a high energy payback ratio, meaning that the energy produced over their lifetime far exceeds the energy used to construct them. The efficiency of energy conversion can vary depending on the river's flow and seasonal variations, but SHPs generally provide reliable power with efficiency ranging from 70% to 90% (Weißbach et al., 2013), (Dagdelen & Apaydin, 2024).

Economic Benefits to Local Communities: SHPs are often praised for their potential to stimulate local economies, especially in rural areas. They can provide jobs during construction and operation, increase energy access, and support local industry by reducing energy costs (Mišić & Obydenkova, 2024), (Smith, 2024).

Government Incentives and Support: In many regions, SHPs benefit from government incentives like feed-in tariffs, tax credits, and subsidies aimed at promoting renewable energy. These incentives can make SHPs more economically viable, particularly in remote areas (M. Singh & Kumar, 2024), (Darmian et al., 2024).

2.2. Ecological Feasibility

Minimal Environmental Impact: SHPs are generally regarded as having a low environmental footprint compared to large-scale hydropower projects, as they do not require large dams or extensive land flooding. However, they are not completely impact-free (Česonienė et al., 2021).

Aquatic Ecosystem Disruption: The main ecological concern with SHPs is their potential to disrupt aquatic ecosystems, particularly fish migration and river biodiversity. Poorly designed SHP systems can alter river habitats, cause sediment buildup, and affect water quality. However, modern designs often include fish ladders and other mitigation measures to minimize such impacts (Maiolini et al., 2007).

Flow Regime Alteration: SHPs can impact the natural flow of rivers, especially during low-flow periods. This can affect downstream ecosystems, especially if environmental flow requirements are not strictly enforced (Kuriqi et al., 2019).

Water Quality and Temperature Changes: While not as significant as with larger dams, SHPs can still affect water quality by altering sediment flow and water temperature, potentially impacting aquatic life. Mitigation measures include fish-friendly turbines and advanced water management practices (Pimenta et al., 2012).

Positive Environmental Aspects: SHPs are a clean source of energy with no direct greenhouse gas emissions during operation. They contribute to reducing dependence on fossil fuels and are considered a low-carbon technology (Von Sperling, 2012).

2.3. Comparative Studies

Ecological vs. Economic Trade-offs: Many studies highlight the trade-offs between the economic benefits and the potential ecological impacts of SHPs. Proper site selection, design, and regulatory oversight are key to balancing these factors. Remote or low-impact sites are often deemed the most favorable for SHP deployment (W. Wang et al., 2022), (L. Wang et al., 2023).

Comparison with Other Renewables: SHPs are compared to other renewable sources like solar, wind, and biomass. In terms of ecological footprint, they have fewer land-use impacts than solar or wind farms. Economically, they can be more reliable due to the continuous nature of river flow, though seasonal variability can affect output (Paraschiv & Paraschiv, 2023).

Long-term Viability: In the long run, SHPs are often seen as more sustainable than fossil fuel-based energy, given their low operating costs and minimal resource depletion. However, the sustainability of SHPs depends on how well they are integrated into local ecosystems without causing long-term environmental degradation (López-González et al., 2019).

2.4. Economic and Environmental Feasibility of Small Hydro Power Projects

Monteiro et al. (2021) analyze the economic viability of small hydroelectric power (SHP) projects, emphasizing the role of the Clean Development Mechanism (CDM) in Brazil. The study highlights that while CDM projects initially provided a financial incentive through carbon credits, their economic benefit has significantly diminished due to declining Certified Emissions Reduction (CER) prices. Through a case study of Brazilian SHPs, Monteiro et al. find that the financial impact of CERs on SHP projects is negligible, with less than a 0.2% increase in internal rate of return (IRR). Instead, optimizing investment costs and increasing energy production are identified as more effective strategies for improving economic returns (Monteiro et al., 2021).

From an environmental perspective, the study points to the advantages of SHP systems in remote areas where long-distance power transmission is economically unfeasible. Additionally, SHPs contribute less to environmental pollution compared to fossil fuel-based energy sources, aligning with global climate goals to reduce greenhouse gas emissions. However, the authors also critique the inefficacy of CDM projects in fostering local community involvement and delivering broader sustainable development benefits.

2.5. Water-Energy-Ecosystem Nexus in Small Run-of-River Hydropower

Basso et al. (2020) explore the intersection of hydropower production, environmental conservation, and ecosystem services in their study on small RoR hydropower systems. The authors emphasize the trade-offs between energy production and ecological impacts, particularly the strain placed on aquatic ecosystems due to flow reductions. Through a multi-objective design framework applied to a hypothetical case study in Scotland, the study demonstrates how optimizing plant configurations can balance these competing demands.

One of the critical insights from Basso et al. is the importance of integrating environmental flow requirements into the design of RoR systems. By treating environmental flow as a decision variable, they identify economically viable configurations that also preserve key ecological functions, such as hydrological connectivity for migratory species like salmon. The study calls for hydropower policies that avoid penalizing larger installations, as these may sometimes offer better ecological and economic outcomes (Basso et al., 2020).

This work highlights the need for a nuanced approach to RoR system design, where both energy production and ecosystem services are considered simultaneously. This aligns with global sustainability goals, particularly in regions where water resources are critical for both energy and biodiversity.

2.6. LCOE-Based Optimization for Small Run-of-River Hydropower Plants

Amougou et al. (2022) focus on optimizing the design of small RoR hydropower plants through a levelized cost of energy (LCOE) framework. The study provides a comprehensive methodology for designing cost-efficient and energy-efficient hydropower systems by integrating hydraulic, mechanical, and economic factors. The optimization model proposed in the study calculates key design parameters such as penstock dimensions, turbine selection, and flow rates to minimize the LCOE.

In a case study of the Nyong River in Cameroon, the model demonstrates that small RoR plants can achieve competitive LCOEs, with an estimated 0.05 USD/kWh. This is at the lower end of the typical LCOE range for SHPs,

confirming the financial viability of such projects in rural electrification contexts. Moreover, the study emphasizes the role of locally manufactured turbines in promoting job creation and economic development, making RoR systems particularly attractive in developing regions (Amougou et al., 2022).

Amougou et al.'s work underscores the importance of optimizing multiple aspects of RoR systems to enhance both economic and operational efficiency. The study also highlights the potential for small RoR systems to contribute to energy security and sustainable development, particularly in off-grid areas.

2.7.Design Models for Run-of-River Hydropower Plants

The review by Tsuanyo et al. (2023) examines various models used in the design of run-of-river (RoR) hydropower plants, which are favored for their minimal environmental footprint. RoR plants typically do not require large reservoirs, which reduces construction costs, shortens project timelines, and mitigates ecological disruption. Tsuanyo et al. identify key parameters such as penstock diameter, turbine suction head, and cost estimation for both grid-connected and off-grid systems. They argue that effective design requires careful consideration of these parameters, as incorrect calculations can lead to operational inefficiencies and higher costs. Their study offers a detailed guide for optimizing RoR designs based on site-specific conditions (Tsuanyo et al., 2023).

2.8. Optimization in Hydropower Resource Planning

In a complementary study, Coban and Sauhats (2022) discuss the role of mathematical models and optimization techniques in planning SHP systems. Their research emphasizes the uncertainty involved in predicting river flow rates, electricity market prices, and other external factors that influence hydropower production. They employ both deterministic and stochastic programming methods to optimize long-term planning decisions. The Monte Carlo method, used to model uncertainties, provides insights into potential outcomes of SHP projects, helping stakeholders make informed investment decisions. This study underscores the complexity of planning SHPs in dynamic environments and highlights the importance of robust optimization tools (Coban and Sauhats 2022).

2.9. Multi-Criteria Decision Analysis (MCDA) and Ecosystem Trade-offs

Barton et al. (2020) extend the discussion by introducing multi-criteria decision analysis (MCDA) within Bayesian networks to balance hydropower production with ecosystem service preservation. Their research focuses on the Mandalselva River in Norway, where hydropower plants impact Atlantic salmon habitats and local biodiversity. By integrating ecological models with economic data, Barton et al. evaluate trade-offs between hydropower revenues and environmental objectives, such as fish population sustainability and river

aesthetics. The use of Bayesian networks allows for the modeling of uncertainties and stakeholder preferences, facilitating more transparent decision-making processes. This study highlights the increasing need for integrated approaches to SHP management that consider not only technical and economic factors but also environmental and social impacts (Barton et al., 2020).

Evaluating the trade-offs between economic and ecological feasibility in river-type small hydropower plants requires a multifaceted approach that incorporates various methodologies and design considerations. The following key aspects highlight effective methods for this evaluation.

2.10. Methodologies for Trade-off Analysis

Multi-objective Optimization: Utilizing a multi-objective optimization framework allows for the identification of Pareto-optimal alternatives, balancing economic value against environmental impacts such as sediment transport and fish growth (Ploussard et al., 2024).

Monte Carlo Simulations: This method helps in exploring a wide solution space, identifying "win-win" scenarios that optimize both economic and ecological outcomes (Ploussard et al., 2024).

Design Considerations

Run-of-River Models: Specific design models for run-of-river hydropower plants can enhance economic feasibility while minimizing ecological disruption. These models assess variables like penstock diameter and turbine selection to optimize energy production and cost (Tsuanyo et al., 2023).

Capacity Optimization: Studies indicate that optimizing installed capacity based on hydraulic parameters can significantly improve energy output while ensuring ecological flow requirements are met (Yusuf et al., 2022).

Innovative Technologies

Conveyor-type Systems: New designs, such as conveyor-type hydropower plants, offer efficient energy generation in shallow waters without dam construction, thus reducing ecological impacts (Beresnevich et al. 2023).

While these methods provide a robust framework for evaluating trade-offs, it is essential to recognize that the negative ecological consequences of hydropower projects can sometimes outweigh their economic benefits, necessitating careful consideration of all factors involved.

3. Comparative Analysis

3.1.Economic Viability and Policy Incentives

Monteiro et al. (2021) highlight the diminishing role of the Clean Development Mechanism (CDM) in enhancing the economic feasibility of

SHP projects in Brazil. While CDM projects initially boosted returns through carbon credits, the falling price of Certified Emissions Reductions (CER) has made their financial impact negligible. The study concludes that optimizing investment costs and enhancing energy output are more effective strategies for improving economic returns, with a less than 0.2% increase in internal rate of return (IRR) attributed to CERs. This indicates that policy-driven incentives, such as CDM, may no longer be sufficient to ensure economic viability in certain contexts.

In contrast, Amougou et al. (2022) focus on optimizing SHP designs to reduce the levelized cost of energy (LCOE). Their study, conducted on the Nyong River in Cameroon, demonstrates that small RoR plants can achieve highly competitive LCOEs of around 0.05 USD/kWh. This is particularly important in off-grid regions, where low-cost energy is essential for rural electrification. Unlike Monteiro et al., who emphasize policy limitations, Amougou et al. show that design and operational optimization—such as using locally produced turbines—can directly improve economic feasibility.

3.2. Environmental Sustainability and Ecosystem Services

While Monteiro et al. (2021) acknowledge the environmental benefits of SHPs, particularly in remote areas where long-distance power transmission is economically infeasible, they also critique the lack of local community involvement in CDM projects. This contrasts with Basso et al. (2020), who take a more nuanced approach to environmental sustainability by examining the ecological trade-offs inherent in small RoR systems. Basso et al. argue that reducing river flows for hydropower production can strain aquatic ecosystems, particularly affecting species like migratory salmon. By integrating environmental flow requirements into the design process, their study proposes a balanced solution that maintains both energy production and ecosystem services.

Barton et al. (2020) extend this discussion by using multi-criteria decision analysis (MCDA) to balance hydropower revenues with ecosystem service preservation. Their study of the Mandalselva River in Norway shows how integrating ecological models with economic data helps decision-makers weigh trade-offs between fish population sustainability and hydropower output. This framework enables more transparent and informed decisions, particularly in regions where biodiversity and environmental aesthetics are significant concerns.

3.3. Technical Optimization and Resource Planning

Technical optimization is central to both Amougou et al. (2022) and Tsuanyo et al. (2023). While Amougou et al. focus on LCOE optimization, Tsuanyo et al. delve into the detailed design parameters of RoR systems, such

as penstock dimensions and turbine selection. Both studies emphasize the importance of site-specific conditions in achieving optimal design outcomes. Tsuanyo et al. provide a detailed guide for RoR systems, highlighting how incorrect calculations can lead to inefficiencies and increased costs. This aligns with Amougou's focus on cost-efficiency through robust design methodologies.

Coban and Sauhats (2022) approach optimization from a planning perspective, using both deterministic and stochastic programming methods to account for the unpredictability of river flow rates and market prices. By employing the Monte Carlo method, they model uncertainties that can significantly impact the financial viability of SHP projects. This study complements the technical optimization discussed by Tsuanyo et al. by highlighting the importance of long-term planning in ensuring that SHP systems remain both financially and operationally sustainable.

4. Discussion

This literature review has consolidated knowledge from various studies on the feasibility of small hydropower plants (SHPs), specifically focusing on economic and ecological considerations. By synthesizing the existing body of research, several key themes have emerged that inform the potential of SHPs in contributing to Turkey's renewable energy landscape while highlighting both opportunities and challenges.

Economic Viability of Small Hydropower Plants: The reviewed literature consistently highlights that SHPs, particularly run-of-river (RoR) systems, present a cost-effective renewable energy option due to their relatively low operational and maintenance costs. Studies such as those by Kumar and Saini (2022) and Singh and Singal (2017) emphasize that while the initial capital investment for SHPs can be substantial, their long-term economic benefits often outweigh these upfront costs. However, the review also identifies a significant gap in the literature regarding strategies to mitigate these high initial costs, especially in regions with limited financial incentives. This gap indicates a need for more research into innovative financing mechanisms or public-private partnerships to make SHP projects more accessible and economically feasible.

Ecological Impact and Sustainability Concerns: One of the most critical themes identified in this literature review is the ecological trade-offs associated with SHP installations. While SHPs are generally recognized for their low environmental footprint compared to large-scale hydropower systems, the review highlights the nuanced ecological impacts that can arise, particularly concerning aquatic ecosystems. Studies like those by Česonienė et al. (2021) and Maiolini et al. (2007) discuss the disruptions to fish migration, sediment flow, and water quality caused by poorly designed SHPs. Despite the

incorporation of mitigation measures such as fish ladders and eco-friendly turbines, the review indicates a lack of consistent ecological assessments across different regions and types of SHP projects. This gap suggests an urgent need for standardized methodologies in evaluating and minimizing the environmental impacts of SHPs, tailored to local ecological conditions.

Comparative Analysis with Other Renewable Energy Sources: The review also places SHPs in the broader context of renewable energy technologies. Compared to solar and wind power, SHPs are noted for their ability to provide more consistent energy output due to the continuous nature of river flow. However, the literature highlights seasonal variability as a significant limitation, which can affect energy reliability. Paraschiv et al. (2023) argue that while SHPs have a smaller land-use impact than solar farms or wind installations, their performance is highly site-dependent. The review suggests that future research should focus on developing hybrid renewable energy systems that integrate SHPs with other energy sources to enhance reliability and optimize land use.

Technological Advances and Optimization Techniques: The literature review identifies significant advancements in the optimization of SHP design and operation. The use of methodologies such as Levelized Cost of Energy (LCOE) frameworks and Monte Carlo simulations has been instrumental in enhancing the economic efficiency of these systems, as evidenced by the studies of Amougou et al. (2022) and Tsuanyo et al. (2023). These approaches enable a more precise understanding of the trade-offs between cost, efficiency, and ecological impact. However, despite these technological improvements, the review points out that there remains a gap in adaptive management techniques that can dynamically respond to changes in river flow rates and environmental conditions. Addressing this gap could lead to more resilient SHP designs that are better suited to fluctuating climatic conditions.

Policy Implications and the Role of Government Incentives: The role of policy and governmental incentives emerged as a critical factor in the economic feasibility of SHPs. The review found that while incentives like feed-in tariffs and tax credits significantly improve the attractiveness of SHP investments, their effectiveness varies widely across different regions. Studies by Monteiro et al. (2021) indicate that international mechanisms like the Clean Development Mechanism (CDM) have become less impactful due to falling carbon credit prices. This finding underscores the need for localized policy frameworks that support the financial sustainability of SHPs, especially in emerging markets like Turkey. Future research should explore the effectiveness of different incentive structures in promoting SHP development and identify best practices from countries with successful SHP policies.

Identified Gaps and Directions for Future Research: One of the most significant contributions of this literature review is its identification of gaps in both economic and ecological aspects of SHP research. While there is ample data on the technical and financial aspects of SHPs, there is a notable lack of comprehensive studies that integrate economic analysis with ecological impact assessments. Additionally, the review reveals limited research on the social dimensions of SHPs, such as community involvement and the social acceptability of these projects. Addressing these gaps will be crucial in developing a holistic understanding of SHP feasibility that encompasses economic, ecological, and social factors.

Conclusion

The synthesis of existing studies in this review indicates that while small hydropower plants hold significant potential as a renewable energy source, their successful implementation requires a balanced approach that considers both economic viability and ecological sustainability. The gaps identified in the literature suggest that future research should focus on integrated methodologies that combine financial analysis, ecological impact studies, and community engagement strategies. Advancements in technology, coupled with supportive policy frameworks, will be essential to unlocking the full potential of SHPs as a key contributor to sustainable energy transitions in Turkey and beyond.

References

Amougou, C. B., Tsuanyo, D., Fioriti, D., Kenfack, J., Aziz, A., & Elé Abiama, P. (2022). LCOE-Based Optimization for the Design of Small Run-of-River Hydropower Plants. *Energies*, *15*(20). https://doi.org/10.3390/en15207507

Barton, D. N., Sundt, H., Bustos, A. A., Fjeldstad, H. P., Hedger, R., Forseth, T., Berit Köhler, Aas, Ø., Alfredsen, K., & Madsen, A. L. (2020). Multi-criteria decision analysis in Bayesian networks - Diagnosing ecosystem service trade-offs in a hydropower regulated river. *Environmental Modelling and Software*, *124*(December 2019). https://doi.org/10.1016/j.envsoft.2019.104604

Basso, S., Lazzaro, G., Bovo, M., Soulsby, C., & Botter, G. (2020). Water-energy-ecosystem nexus in small run-of-river hydropower: Optimal design and policy. *Applied Energy*, *280*(January), 115936. https://doi.org/10.1016/j.apenergy.2020.115936

Calvin, K., Dasgupta, D., Krinner, G., Mukherji, A., Thorne, P. W., Trisos, C., Romero, J., Aldunce, P., Barrett, K., Blanco, G., Cheung, W. W. L., Connors, S., Denton, F., Diongue-Niang, A., Dodman, D., Garschagen, M., Geden, O., Hayward, B., Jones, C., … Ha, M. (2023). IPCC, 2023: Climate Change 2023: Synthesis Report. Contribution of Working Groups I, II and III to the Sixth Assessment Report of the Intergovernmental Panel on Climate Change [Core Writing Team, H. Lee and J. Romero (eds.)]. IPCC, Geneva, Switzerland. *Ipcc*, *13*(3), 35–115. https://doi.org/10.59327/IPCC/AR6-9789291691647

Česonienė, L., Dapkienė, M., & Punys, P. (2021). Assessment of the Impact of Small Hydropower Plants on the Ecological Status Indicators of Water Bodies: A Case Study in Lithuania. In *Water* (Vol. 13, Issue 4). https://doi.org/10.3390/w13040433

COBAN, H. H., & SAUHATS, A. (2022). Optimization tool for small hydropower plant resource planning and development: A case study. *Journal of Advanced Research in Natural and Applied Sciences*, *8*(3), 391–428. https://doi.org/10.28979/jarnas.1083208

Dagdelen, E., & Apaydin, H. (2024). Cost-effectiveness of Hydroelectric Turbines and Pumps as an Alternative to Pressure-Reducing Valves for Electricity Production in Irrigation Lines in Turkey. *Water Conservation Science and Engineering*, *9*(2), 1–14.

Darmian, S. M., Tavana, M., & Ribeiro-Navarrete, S. (2024). An Investment Evaluation and Incentive Allocation Model for Public-Private Partnerships in Renewable Energy Development Projects. *Socio-Economic Planning Sciences*, 101953.

Forouzbakhsh, F., Hosseini, S. M. H., & Vakilian, M. (2007). An approach to the investment analysis of small and medium hydro-power plants. *Energy Policy*, *35*(2), 1013–1024. https://doi.org/https://doi.org/10.1016/j.enpol.2006.02.004

International Energy Agency. (2024). *Electricity Mid-Year Update*. *July*.

Kumar, K., & Saini, R. P. (2022). Economic analysis of operation and maintenance costs of hydropower plants. *Sustainable Energy Technologies and Assessments*, *53*, 102704. https://doi.org/https://doi.org/10.1016/j.seta.2022.102704

Kuriqi, A., Pinheiro, A. N., Sordo-Ward, A., & Garrote, L. (2019). Flow regime aspects in determining environmental flows and maximising energy production at run-of-river hydropower plants. *Applied Energy*, *256*, 113980.

López-González, A., Ferrer-Martí, L., & Domenech, B. (2019). Long-term sustainability assessment of micro-hydro projects: Case studies from Venezuela. *Energy Policy*, *131*, 120–130.

Maiolini, B., Silveri, L., & Lencioni, V. (2007). Hydroelectric power generation and disruption of the natural stream flow: effects on the zoobenthic community. *Studi Trentini Di Scienze Naturali Acta Biologica*, *83*, 21–26.

Mišić, M., & Obydenkova, A. (2024). Environmental conflict, renewable energy, or both? Public opinion on small hydropower plants in Serbia. In *Global Environmental Politics and International Organizations* (pp. 120–149). Routledge.

Monteiro, L. S., Costa, K. A., Christo, E. da S., & Freitas, W. K. (2021). Economic feasibility analysis of small hydro power projects. *International Journal of Environmental Science and Technology*, *18*(6), 1653–1664. https://doi.org/10.1007/s13762-020-02931-6

Paraschiv, L. S., & Paraschiv, S. (2023). Contribution of renewable energy (hydro, wind, solar and biomass) to decarbonization and transformation of the electricity generation sector for sustainable development. *Energy Reports*, *9*, 535–544. https://doi.org/https://doi.org/10.1016/j.egyr.2023.07.024

Pimenta, A. M., Albertoni, E. F., & Palma-Silva, C. (2012). Characterization of water quality in a small hydropower plant reservoir in southern Brazil. *Lakes & Reservoirs: Research & Management*, *17*(4), 243–251.

Ploussard, Q., Veselka, T., & De Silva, T. (2024). Methodology for Exploring Water and Hydropower Operating Criteria That Simultaneously Improve Economic and Environmental Considerations. In *Water* (Vol. 16, Issue 3). https://doi.org/10.3390/w16030371

Seme, S., Sredenšek, K., Praunseis, Z., Štumberger, B., & Hadžiselimović, M. (2018). Optimal price of electricity of solar power plants and small hydro power plants–Technical and economical part of investments. *Energy*, *157*, 87–95.

Singh, M., & Kumar, S. (2024). Policy level changes initiated by Government of India for development of hydro power sector in India ensuring dam safety and safety of other structures. *Water and Energy International*, *66*(11), 28–35.

Singh, V. K., & Singal, S. K. (2017). Operation of hydro power plants-a review. *Renewable and Sustainable Energy Reviews*, *69*, 610–619.

Smith, D. (2024). The social impacts of dams and hydropower. In *Handbook of Social Impact Assessment and Management* (pp. 51–66). Edward Elgar Publishing.

Tsuanyo, D., Amougou, B., Aziz, A., Nka Nnomo, B., Fioriti, D., & Kenfack, J. (2023). Design models for small run-of-river hydropower plants: a review. *Sustainable Energy Research*, *10*(1), 1–23. https://doi.org/10.1186/s40807-023-00072-1

View of CONVEYOR-TYPE SMALL HYDROPOWER PLANT FOR SHALLOW RIVER WATERS.pdf. (n.d.).

Von Sperling, E. (2012). Hydropower in Brazil: overview of positive and negative environmental aspects. *Energy Procedia*, *18*, 110–118.

Wang, L., Xu, B., Zhang, C., Chen, X., Zheng, Y., Zhang, J., & Fu, G. (2023). Exploring the trade-offs among hydropower benefits, environmental flow, and surface water temperature in a large reservoir under deep uncertainty. *Journal of Hydrology*, *624*, 129913. https://doi.org/https://doi.org/10.1016/j.jhydrol.2023.129913

Wang, W., Wang, H., Liu, G., & Gao, L. (2022). Analysis of the trade-off between hydroelectricity generation and ecological protection from the perspective of eco-efficiency in Southwest China. *Journal of Environmental Management*, *315*, 115063. https://doi.org/https://doi.org/10.1016/j.jenvman.2022.115063

Weißbach, D., Ruprecht, G., Huke, A., Czerski, K., Gottlieb, S., & Hussein, A. (2013). Energy intensities, EROIs (energy returned on invested), and energy payback times of electricity generating power plants. *Energy*, *52*, 210–221.

Yusuf, K., Alkhaly, Y. R., & Amalia, A. (2022). Optimization of Small Run-of-River Hydropower Plant Capacity. *International Journal of Engineering, Science and Information Technology*, *2*(3), 58–63. https://doi.org/10.52088/ijesty.v2i3.290

Chapter 4

RESEARCH OF PUBLIC PERCEPTION AND AWARENESS ABOUT ENVIRONMENTAL POLLUTION OF OPEN WASTE DUMPING IN A SELECTED SITE

Faisal A. Osra[1*], Hasan Abdullah Mosaıbah[1], Mirac Nur Ciner[2], H. Kurtulus Ozcan[2], Emine Elmaslar Özbaş[2]

1 Civil Engineering Department, College of Engineering and Islamic Architecture, Umm Al-Qura University, Makkah 21955, Saudi Arabia; faosra@uqu.edu.sa, s44182120@st.uqu.edu.sa
2 Engineering Faculty, Department of Environmental Engineering, Istanbul University-Cerrahpasa, Avcılar, Istanbul 34320, Turkey; mirac.ciner@iuc.edu.tr, hkozcan@iuc.edu.tr, elmaslar@iuc.edu.tr

1. Introduction

Today, exponential population growth and the intensification of industrial activities globally have led to a rapid increase in municipal and industrial waste production (Adamović et al. 2018; Chen, 2018-a; Osra et al. 2024). The increase in urban solid waste represents a significant environmental challenge in the current urbanization process. Population growth, urbanization, economic expansion, and improvements in living standards have accelerated the generation of solid waste in cities (Song & Zeng, 2015). The composition of urban solid waste is influenced by various factors such as urbanization and is highly diverse, containing many components that can contribute to environmental pollution and ecosystem degradation (Chen, 2018-b). Additionally, the sustainable management of materials such as plastics, metals, paper, cardboard, and organic matter within the waste is crucial for recycling and recovery efforts (Kassim, 2012; Troschinetz & Mihelcic, 2009). The improper management of solid waste hinders the recycling of valuable materials. At the same time, it contributes to increased greenhouse gas emissions and climate change, negatively affecting both human health and environmental sustainability (Hussain et al. 2015). These issues force local governments to bear substantial costs and develop sustainable solutions (Abarca-Guerrero et al. 2015).

The management of urban solid waste is a critical issue for both environmental and public health. Sustainable waste management primarily focuses on preventing waste generation, reducing waste volume, reusing materials, recycling, and recovery processes. The main objective of this hierarchical approach is to minimize the environmental impact of waste. However, once these processes are completed, the remaining urban solid waste must be safely disposed of in sanitary landfills (Williams, 2013; Chang & Pires, 2015). In some developing and underdeveloped countries, uncontrolled open dumping methods are still used in waste management, leading to serious environmental issues. Such dumping sites are associated with a range of negative environmental impacts (Hoornweg & Bhada-Tata, 2012).

Open dumping is a method where waste is deposited in sites lacking ground sealing and gas control, posing a threat to public health. This practice leads to groundwater contamination, soil degradation, and air pollution, damaging ecosystems. Additionally, the decomposition of organic waste in open dumping sites generates methane gas (CH_4), and its uncontrolled accumulation increases the risk of explosions (Scharff & Jacobs, 2006). In sites where adequate ventilation is not provided, the ignition of this gas can result in sudden and dangerous explosions. These explosions pose serious risks to both environmental destruction and human health. In Saudi Arabia, open dumping practices still partially continue. A significant portion of the waste is disposed of in sites without proper engineering controls, presenting

environmental risks. Sustainable management of urban solid waste is essential for resource conservation and the reduction of greenhouse gas emissions (Zaman, 2015).

Sustainable urbanization not only aims to minimize the environmental impact of urban growth and development but also requires enhancing resource efficiency through the effective management of solid waste. In this context, reducing, recycling, and properly disposing of waste contribute to lowering the ecological footprint of cities, thereby supporting the preservation of social and environmental well-being (Song et al. 2015). The sustainability of cities is directly linked to the implementation of integrated waste management strategies and the principles of a circular economy.

There are numerous studies in the literature evaluating the environmental impacts of open dumping sites. A study conducted in 2024 highlights that the Kakia Open Dumping Site in Makkah has caused significant environmental pollution by negatively affecting groundwater, soil, and air quality. The research found that leachate from these sites contains essential elements such as calcium, magnesium, and sodium, as well as heavy metals like lead, cadmium, and chromium, which have seeped into the soil and groundwater, causing severe ecological damage. These findings emphasize the urgent need for the closure of open dumping sites and the implementation of appropriate rehabilitation processes to minimize the negative impacts on the environment and public health (Osra et al. 2024).

In their 2021 study, Talang and Sirivithayapakorn examine the environmental and financial impacts of traditional municipal solid waste (MSW) disposal methods, such as open burning and open dumping, across different income groups. The study concludes that integrated waste disposal scenarios (a combination of recycling, incineration, composting, and landfill processes) are recommended as the most optimal solutions from both environmental and financial perspectives (Talang & Sirivithayapakorn, 2021).

Another study conducted in 2022 examines the negative environmental and health impacts of open dumping sites. Open dumping sites contribute to environmental issues such as the leaching of harmful substances into groundwater, air pollution, and the spread of unpleasant odors, while also causing serious health problems, including cancer and respiratory diseases, among nearby residents. The study emphasizes the need for the closure of these sites and the implementation of appropriate waste management practices (Siddiqua et al. 2022).

In their 2022 study, Vaigunthan and Sewwandi mapped the environmental pollution risks caused by open dumping practices at the Karadiyana MSW site in Sri Lanka using Geographic Information Systems (GIS). The study found that the leachate from the open dumping site contained pollutants such as

phosphates and heavy metals, which spread into the soil and water sources. The results indicated that pollution from such dumpsites spreads both seasonally and geographically, highlighting the need for effective measures to ensure sustainable waste management (Vaigunthan & Sewwandi, 2022).

The aim of this study is to assess the perceptions of individuals living around the Kakia Open Dumping Site, their awareness of environmental pollution, and their concerns about its impacts. The research employs a survey method to collect and analyze the views of the local population regarding waste management processes and their effects on their quality of life. In doing so, the study aims to raise awareness of the negative impacts of open dumping practices on human health and the environment, while promoting the development of more sustainable approaches to waste management.

2. Materials and Methods

2.1. Site Description

Makkah is one of the cities that still practices open dumping for the disposal of MSW. The exponential growth in the population of this metropolis has resulted in the production of substantial amounts of MSW. An analysis of the rate at which MSW is produced in Makkah shows that during the Hajj season from 1994 to 2006, the rate of MSW creation per pilgrim was 2.05 kg per day, whereas for local residents it was 1.60 kg per person per day (Abdul Aziz et al. 2007). According to a previous research investigation, the rate of MSW generation was found to be 1.4 kg per person per day for the local community and 1.9 kg per pilgrim per day for pilgrims (Nizami et al. 2015). In addition, the amount of MSW produced in 2004 was documented to be 1.2 kg per day. This figure escalated to 1.5 kg per day in Riyadh city and 2 kg per day during the Hajj and Ramadan periods in Makkah City (MEP, 2005).

The rate of MSW generation varied across different cities in Saudi Arabia. Major cities such as Riyadh, Makkah, Medina, Jeddah, Dammam, and Al-Ahsa had a generation rate of 1.5 kg/day. Medium-sized population cities had a rate of 1.2 kg/day, while low-population cities and villages had a rate of 1.0 kg/day (GCC, 2013). Furthermore, it is important to highlight that a substantial amount of 4500 tons of MSW is generated on a daily basis during the Hajj season (Osra et al. 2021). This MSW is mostly composed of organic materials and plastics (Mashat, 2014; Osra, 2017). After examining MSWM in Makkah, it was found that the historical method of disposing waste (dumping) was used at two primary locations. These locations are the Muasiam Site, which stopped operating in 2003, and the Kakia Site, which has been in operation since 2003 till now.

The Kakia Dumpsite is situated in the southwestern region of Makkah city, along the expansion of Aranah wadi. It is situated between longitudes

39°47′60″ and 39°48′39″ E, and latitudes 21°15′53″ and 21°15′29″ N. The Kakia Dumpsite is located in a valley encompassed by a cluster of mountains (Osra, 2020). The subsurface sand deposits have a depth of roughly 12 meters. The estimated area of the Kakia Dumpsite is approximately 452,489 square meters, and the increased area now covers 1,077,188 square meters. The expected duration of its functioning is seven years. The site has a maximum elevation of 10 meters above the ground surface and does not have a liner or a gas and leachate collection system. Every day, it receives an average of around 3100 tons of solid garbage, which tends to increase during Hajj and the month of Ramadan.

Furthermore, the Kakia Dumpsite is encompassed by highways and different facilities, including residential, health, sports, industrial, and educational institutions. These activities are primarily focused in the eastern vicinity and in close proximity to the dumping site. These facilities consist of residential areas, ready-mix concrete plants, hospitals, educational facilities, scrap collection sites, sports centers, vehicle maintenance shops, showroom centers, and a stadium (Figure 1). Due to these factors, it is crucially important to manage MSW in a manner that does not cause harm to the environment and public health.

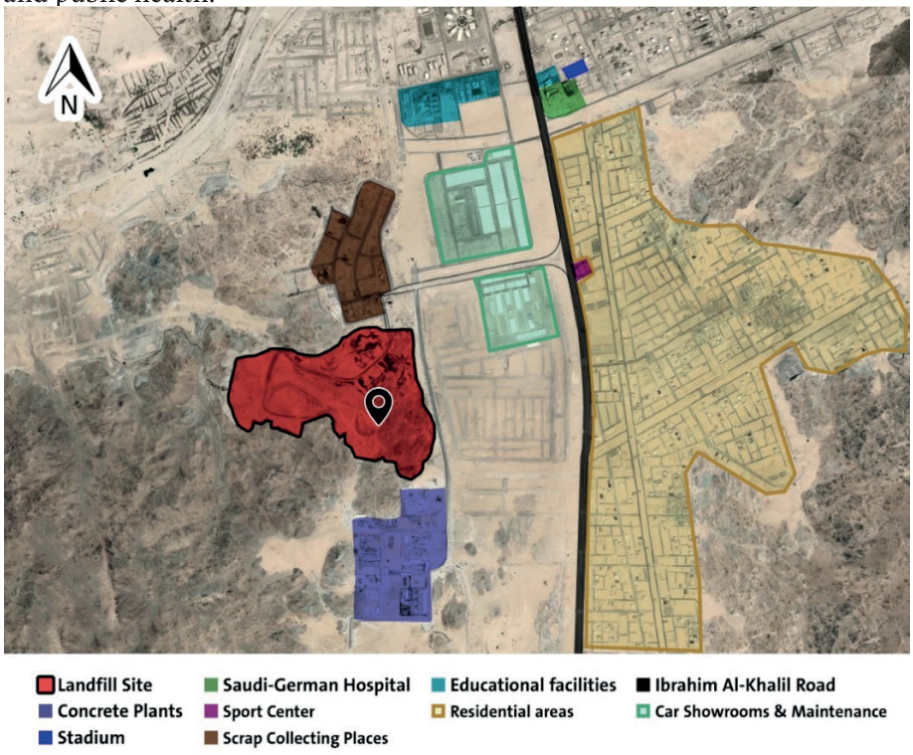

Figure 1. Kakia Open Dumping Site and land-use map showing the major activities that take place around the dump

2.2. Questionnaire Study

A total of 100 questionnaires were interviewed with the residents around Kakia Dumping Site, to determine the major trends and opinions about the adverse environmental impacts of the concerned site. In general, the questionnaire survey was conducted during October 2022, the questionnaires were composed of 15 points (Table 1). The answers were directly given by the respondents, according to their living conditions around Kakia Dumping Site.

Table 1. Environmental questionnaire about the potential threats around Kakia Open Dumping Site.

Question-1 Duration of living in the residential community near Kakia Dumping Site ? a) Less than 1 year b) 2-3 years c)More than 3 years	**Question-2** Approximate distance between residential community and Kakia Dumping Site? a) Less than 1 km b) 2-3 km c) More than 3 km	**Question-3** Are you affected by Kakia Dumping Site? a) Yes b) No
Question-4 What are the harmful effects? a) Air pollution b) Noise c) Soil Pollution d) Others	**Question-5** Are there sensitive facilities in the vicinity of Kakia Dumping Site? a) Yes b) No	**Question-6** Are there industries adjacent to the Kakia Dumping Site? a) Yes b) No
Question-7 Are the odors emanating from Kakia Dumping Site noticeable? a) Yes b) No	**Question-8** Are the odors emanating from Kakia Dumping Site regular? a) Yes b) No	**Question-9** Are the odors emanating from Kakia Dumping Site continuous? a) Yes b) No
Question-10 Is there dust in the residential community? a) Yes b) No	**Question-11** Do you believe that odors are associated with the seasons of the year? a) Yes b) No	**Question-12** What is the season associated with odors? a) Summer b) Winter c) Others
Question-13 What are the peak times of dust? a) Early morning b) Morning c) Afternoon d) Evening	**Question-14** Have you thought about migrating the residential community as a result of odors? a) Yes b) No	**Question-15** Did you introduce a complaint dues to odors? a) Yes b) No

The survey was composed of 15 multiple-choice items, with each item having only one correct choice. The items mainly concerned the respondent's

understanding of environmental issues and environmental knowledge. The interviews were conducted through face-to-face consultations. After collection of the questionnaire data, the statistical analysis was executed.

3. Results and Discussion

Duration of living in the residential community near Kakia Dumping Site: It is estimated that a major component of 44% of residents living around the Kakia Dumping Site have been there for less than 1 year, while 35% have lived there for about 2-3 years, and 21% have lived there for more than 3 years (Figure 2).

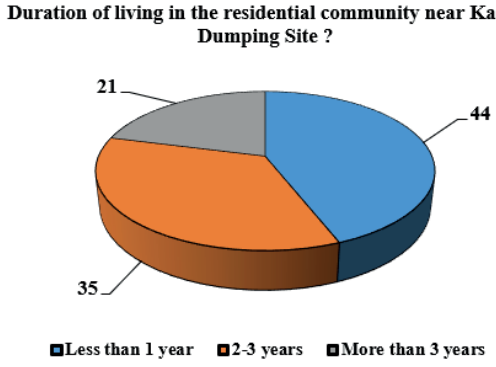

Figure 2. Environmental questionnaire about the potential threats around Kakia Open Dumping Site.

Approximate distance between the residential community and Kakia Dumping Site: It has been found that a major fraction of residents (63%) in residential communities live at a distance less than 1 km from the Kakia Dumping Site, while 32% live at a distance ranging from 2-3 km, and 5% live at a distance greater than 3 km (Figure 3).

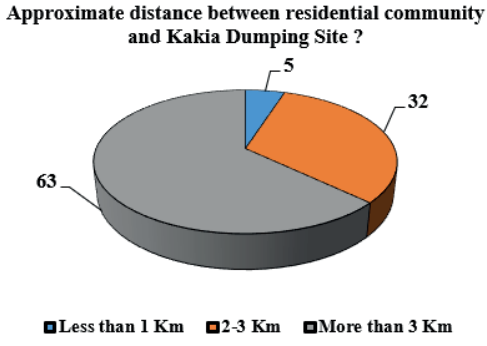

Figure 3. Approximate distance between residential community and Kakia Open Dumping Site.

Adverse impacts of Kakia Dumping Site on surrounding residential communities: It has been found that a major fraction of residents (95%) living in residential communities were affected by the Kakia Dumping Site, while 5% were not affected by the Kakia Dumping Site (Figure 4).

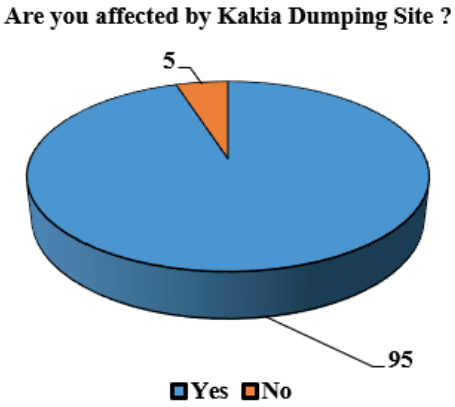

Figure 4. Rate of impact of Kakia Open Dumping Site on the surrounding residential communities.

Type of environmental impact of Kakia Dumping Site on surrounding residential communities: It has been found that a major fraction of residents (92%) living in residential communities were affected by the Kakia Dumping Site through air pollution, while 3% were impacted by noise levels, and 2% were affected by soil pollution (Figure 5).

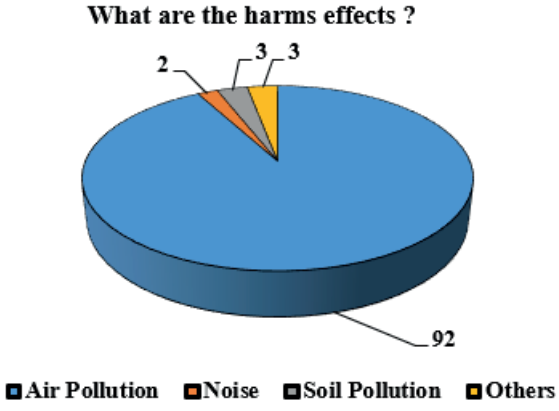

Figure 5. Type of environmental impact of Kakia Open Dumping Site on surrounding residential communities.

Regarding the presence of sensitive facilities near the Kakia Dumping Site, a significant majority (94%) confirm their existence, while 6% do not. (Figure 6).

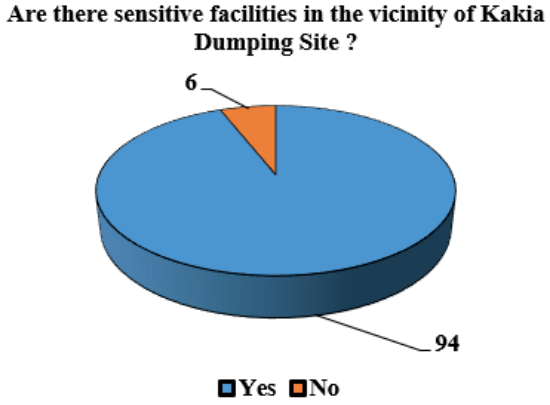

Figure 6. Presence of sensitive facilities near Kakia Open Dumping Site.

Regarding the presence of industries near the Kakia Dumping Site, a significant majority (69%) confirm the presence of industries, while 31% do not (Figure 7).

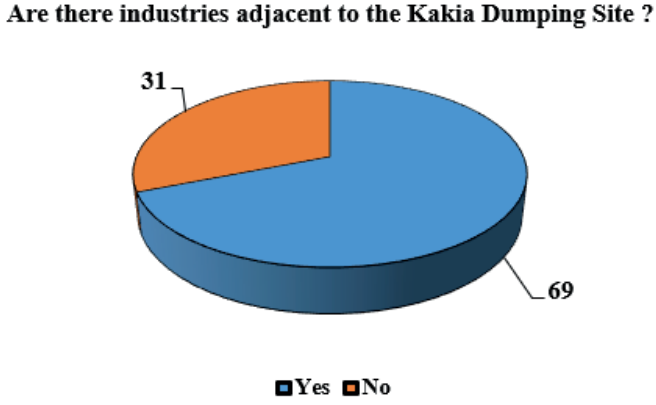

Figure 7. Presence of industries near Kakia Open Dumping Site.

Noticeable odors emanating from Kakia Dumping Site: It is found to be a major fraction (95%) states the presence of odors, and a rate of 5% does not state that (Figure 8).

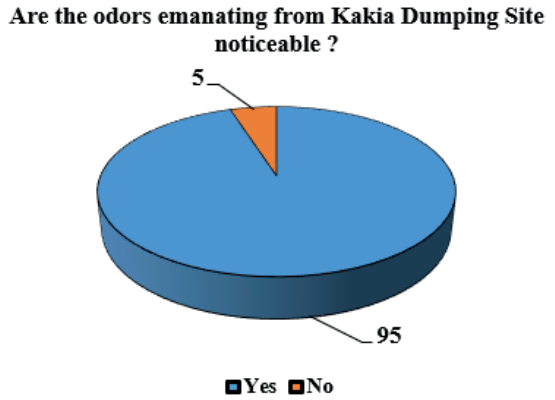

Figure 8. Presence of noticeable odors emanating from Kakia Open Dumping Site.

The regularity of noticeable odors emanating from the residents of Al-Kakia Dumping Site: It was found that a significant percentage of the population (78%) indicated that the odors occur regularly, while a percentage (22%) of the population perceived the odors as irregular in occurrence (Figure 9).

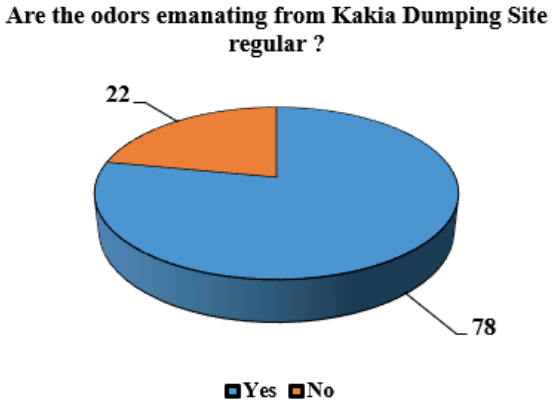

Figure 9. Regularity of noticeable odors emanating from Kakia Open Dumping Site.

Continuity The continuity of noticeable odors emanating from the Kakia Dumping Site: It was found that a significant percentage of the population (63%) perceives the odors as continuous in occurrence, while a percentage (37%) of the population sees the odors as non-continuous in occurrence (Figure 10).

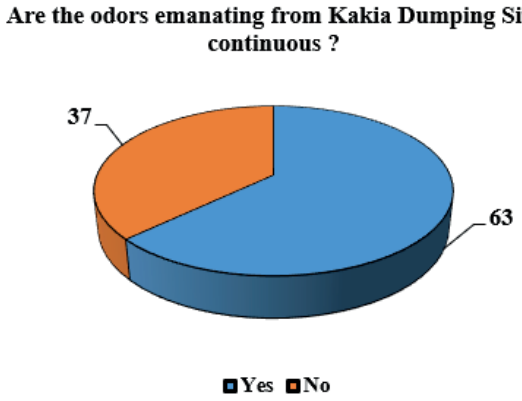

Figure 10. Continuity of noticeable odors emanating from Kakia Open Dumping Site.

Presence of dust in the residential plan: It was found that a significant percentage of the residents (99%) confirm the presence of dust in the residential plan, while 1% of the residents deny it. (Figure 11).

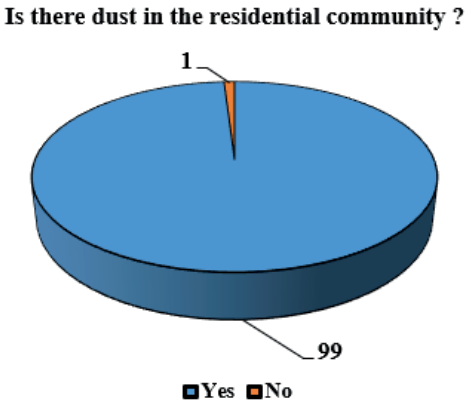

Figure 11. Presence of dust in the residential community.

Relation The relationship between the odors emanating from Kakia Dumping Site and the seasons: It was found that 68% of the population believes that there is a connection between the presence of odors and the seasons, while 32% do not see a connection between the odors and the seasons. (Figure 12).

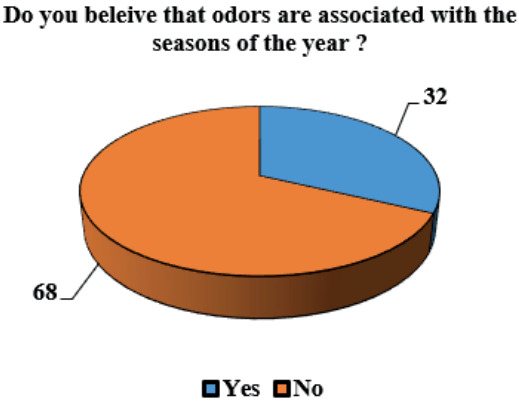

Figure 12. Relation between generated odors from Kakia Open Dumping Site and seasons.

Season and the generated odors from Kakia Dumping Site: It is found that a major fraction (68%) were not unified about the concerned season of odors, 26% agreed with the summer season which represents the maximum generated odors, and a rate of 6% was stated winter season equivalent to the maximum generated odors (Figure 13).

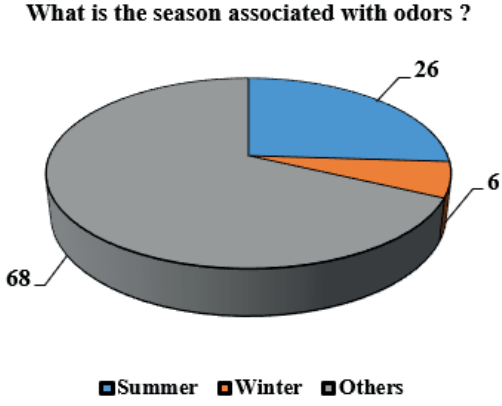

Figure 13. Season and the generated odors from Kakia Open Dumping Site.

Peak times of dust around the Kakia Dumping Site: A significant majority (73%) reported that dust is concentrated in the afternoon around the Kakia Dumping Site, with 20% mentioning evening times, 4% in the morning, and 3% in the early morning. (Figure 14).

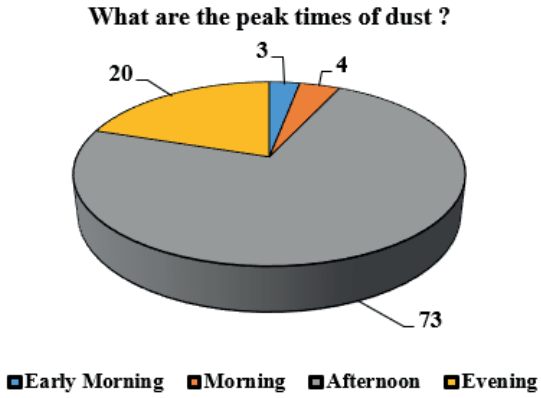

Figure 14. Peak times of dust around Kakia Open Dumping Site.

Probable migration of residents due to the odors emanating from the Kakia Dumping Site: a significant portion (57%) expressed the possibility of migration due to the odors generated from the Kakia Dumping Site, while 43% indicated their intention to stay in residential communities despite the odors. (Figure 15).

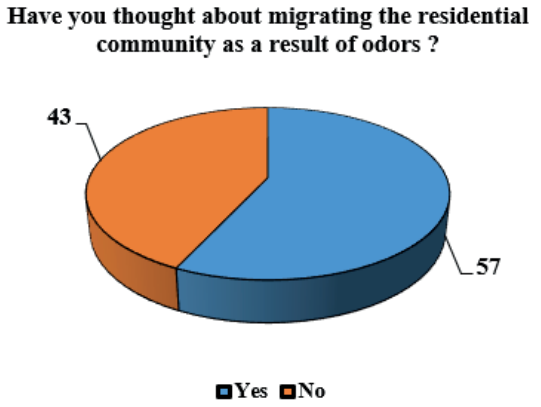

Figure 15. Probable migration of residents due to generated odors from Kakia Open Dumping Site.

Introducing a complaint to governmental authorities about the Kakia Dumping Site: It was found that a significant majority (64%) had not submitted a complaint to governmental authorities regarding the Kakia Dumping Site, while 36% had already submitted a complaint. (Figure 16).

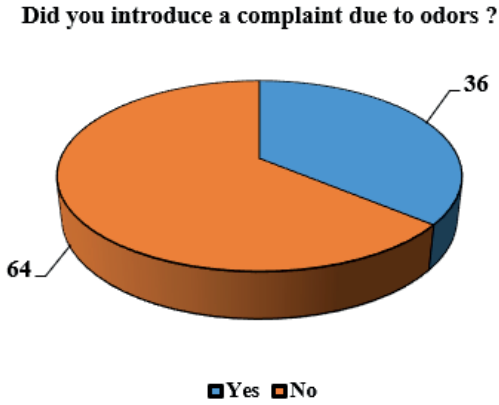

Figure 16. Introducing a complaint to the governmental bodies about Kakia Open Dumping Site.

4. Conclusions

A total of 100 questionnaires were interviewed with the residents around Kakia Dumping Site, to determine the major trend and opinion about the adverse environmental impacts of the concerned site. In general, the questionnaire survey was conducted during October 2022, the questionnaires were composed of 15 points. The answers were directly given by the respondents, according to their living conditions around Kakia Dumping Site.

The items mainly concerned the respondent's understanding of environmental surrounding issues and knowledge. The interviews were conducted through face-to-face consultations. After collection of the questionnaire data, the statistical analysis was executed, to display the data in an understandable form.

The findings of this study underscore the significant environmental and health challenges posed by the Kakia Open Dumping Site, particularly as experienced by the local residents. Residents (37%) live within farthest 3 km of the dumping site, with 92% reporting negative impacts from the site, predominantly due to air pollution. The majority of respondents (95%) also reported unpleasant odors originating from the site, with 78% stating that these odors occur regularly. Additionally, 99% of respondents reported dust emissions from the site's activities, with peak dust times occurring mostly in the afternoon (73%).

The proximity of sensitive facilities and industries near the Kakia Dumping Site was noted by 94% of respondents. A considerable portion of the community (57%) expressed a desire to migrate due to these environmental issues, while others (43%) preferred rehabilitation measures to improve

living conditions. Notably, 36% of respondents have submitted complaints to government bodies regarding the dumping site, highlighting the growing concern among residents.

These results emphasize the urgent need for sustainable waste management solutions and rehabilitation efforts at the Kakia Open Dumping Site to mitigate its environmental and public health impacts. It is essential to implement effective measures for controlling leachate, air pollution, odor, and dust emissions to safeguard the quality of life of the local population.

Acknowledgements

This study, a part of M.Sc. thesis entitled "ENVIRONMENTAL IMPACT ASSESSMENT OF CURRENT LANDFILL IN MAKKAH CITY, SAUDI ARABIA" which was conducted at Umm Al-Qura University.

REFERENCES

Abarca-Guerrero, L., Maas, G., & Hogland, W. (2015). Solid waste management challenges for cities in developing countries. *Revista Tecnología en Marcha*, *28*(2), 141-168.

Abdul Aziz, H.; Isa, M.; Kadir, O.; Nordin, N.; Daud, W.; Alsebaei, A.; Abu-Rizaiza, A. Study of baseline data regarding solid waste management in the holy city of Makkah during Hajj. *In The Custodian of the Two Holy Mosques Institute of the Hajj Research*; Universiti Sains Malaysia: Penang, Malaysia, 2007; (Unpunished Report).

Adamović, V. M., Antanasijević, D. Z., Ćosović, A. R., Ristić, M. Đ., & Pocajt, V. V. (2018). An artificial neural network approach for the estimation of the primary production of energy from municipal solid waste and its application to the Balkan countries. *Waste management*, *78*, 955-968.

Chang, N. B., & Pires, A. (2015). *Sustainable solid waste management: A systems engineering approach*. John Wiley & Sons.

Chen, Y. C. (2018-a). Evaluating greenhouse gas emissions and energy recovery from municipal and industrial solid waste using waste-to-energy technology. *Journal of Cleaner Production*, *192*, 262-269.

Chen, Y. C. (2018-b). Effects of urbanization on municipal solid waste composition. *Waste management*, *79*, 828-836.

GCC. Municipal Solid Waste Management Guidelines in the Cooperation Council for the Arab States of the Gulf; Department of Human Affairs and Environment—The Cooperation Council for the Arab States of the Gulf, (GCC): Riyadh, Saudi Arabia, 2013.

Hoornweg, D., & Bhada-Tata, P. (2012). What a waste: a global review of solid waste management.

Hussain, M. T. D. T., Behaylu, A., & Tilahun, A. (2015). Scenario of present and future of solid waste generation in metro cities of India. *Journal of Environment and Earth science*, *5*(9), 164-9.

Kassim, S. M. (2012, October). The importance of recycling in solid waste management. In *Macromolecular Symposia* (Vol. 320, No. 1, pp. 43-50). Weinheim: WILEY-VCH Verlag.

Mashat, B. Effective Microorganisms (EM) Technology as a Pathway to Improve Municipal Solid Waste of Makkah City (Saudi Arabia) and as Foul Odor Eliminator. In Proceedings of the Clute Institute International Academic Conference, Munich, Germany, 8–12 June 2014; pp. 8–12.

MEP. *The Eighth Development Plan for 2005–2009*; Ministry of Economy and Planning: Riyadh, Saudi Arabia, 2005.

Nizami, A.S.; Rehan, M.; Ismail, I.M.I.; Almeelbi, T.; Ouda, O.K.M. Waste biorefinery in Makkah: A solution to convert waste produced during Hajj and Umrah Sea-

sons into wealth. In Proceedings of the Conference: 15th Scientific Symposium for Hajj, Umrah and Madinah Visit, Medina, Saudi Arabia, 27–28 May 2015.

Osra, F. A., & Kajjumba, G. W. (2020). Landfill site selection in Makkah using geographic information system and analytical hierarchy process. *Waste Management & Research*, *38*(3), 245-253.

Osra, F. A., Elbisy, M. S., Mosaıbah, H. A., Osra, K., Ciner, M. N., & Ozcan, H. K. (2024). Environmental Impact Assessment of a Dumping Site: A Case Study of Kakia Dumping Site. *Sustainability*, *16*(10), 3882.

Osra, F. A., Ozcan, H. K., Alzahrani, J. S., & Alsoufi, M. S. (2021). Municipal solid waste characterization and landfill gas generation in kakia landfill, makkah. *Sustainability*, *13*(3), 1462.

Osra, F. Optimizing the Suitable Site (S) for Landfill by Multi-Criteria Decision and Investigating Biogasification Potential of the Waste in Makkah, Saudi Arabia. Doctoral Dissertation, Institute of Graduate Studies in Science and Engineering, Istanbul University, Istanbul, Türkiye, 2017.

Scharff, H., & Jacobs, J. (2006). Applying guidance for methane emission estimation for landfills. *Waste management*, *26*(4), 417-429.

Siddiqua, A., Hahladakis, J. N., & Al-Attiya, W. A. K. (2022). An overview of the environmental pollution and health effects associated with waste landfilling and open dumping. *Environmental Science and Pollution Research*, *29*(39), 58514-58536.

Song, Q., Li, J., & Zeng, X. (2015). Minimizing the increasing solid waste through zero waste strategy. *Journal of Cleaner Production*, *104*, 199-210.

Talang, R. P. N., & Sirivithayapakorn, S. (2021). Environmental and financial assessments of open burning, open dumping and integrated municipal solid waste disposal schemes among different income groups. *Journal of Cleaner Production*, *312*, 127761.

Troschinetz, A. M., & Mihelcic, J. R. (2009). Sustainable recycling of municipal solid waste in developing countries. *Waste management*, *29*(2), 915-923.

Vaigunthan, T., & Sewwandi, B. G. N. (2022). Mapping of Environmental Pollution Risk Induced by Open Dumping Practice of Municipal Solid Waste in Karadiyana of Sri Lanka Using Geographic Information System. *International Journal for Research in Applied Sciences and Biotechnology*, *9*(1), 127-139.

Williams, P. T. (2013). *Waste treatment and disposal*. John Wiley & Sons.

Zaman, A. U. (2015). A comprehensive review of the development of zero waste management: lessons learned and guidelines. *Journal of Cleaner Production*, *91*, 12-25.

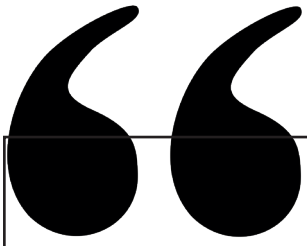

Chapter 5

USE OF VARIOUS ADDITIVES AND FIBERS IN REINFORCED CONCRETE BEAMS

Salih CENGİZ[1]*, Alptuğ ÜNAL[2]

1 Department of Construction, Vocational School of Technical Sciences, Konya Technical University, 42000, Konya, Turkey, ORCID ID: 0000-0003-1571-7488
2 Department of Civil Engineering, Faculty of Engineering and Natural Sciences, Konya Technical University, 42000, Konya, Turkey, ORCID ID: 0000-0003-2945-8325
* Corresponding author, e-mail: scengiz@ktun.edu.tr

1. INTRODUCTION

Concrete is a building material formed by mixing sand, gravel (or crushed stone, lightweight aggregate, etc.), cement, minerals, chemical admixtures and water. When these materials are combined in certain calculated ratios, a plastic material that can take the desired shape in moulds is obtained. One of the most important features of concrete that makes it different from and superior to other materials used in the construction industry is its plastic consistency that enables it to be given the desired shape. Concrete sets shortly after mixing and pouring into the mould and gains strength over time (Ersoy and Özcebe,2001).

Studies were carried out to determine the calculation criteria for reinforced concrete structures and the first regulations were published in Germany in 1904 and in France in 1906. In our country, the implementation of the regulation begins with the use of the German Reinforced Concrete Regulation. The regulation prepared by the Turkish Bridge and Construction Society in 1953 was published again in 1953 and 1962 with some changes. TS 500: Regulation on Calculation and Construction Rules of Reinforced Concrete Structures, prepared by the Turkish Standards Institute, has been valid since 1975. The current regulation is the TS 500–2000 regulation, the last edition of which was published in 2000 (Celeb and Kumbasar, 2001). In addition to TS 500, the Turkish Earthquake Regulation is also implemented in our country.

The main criterion for the quality of concrete is the compressive strength of the concrete. In the studies conducted on concrete, the relationships between the compressive strength of concrete and various properties of the material were investigated and it was observed that other mechanical properties of concrete had the same tendency as the compressive strength (Erdal, 2002). However, when various environmental conditions come into play, in addition to compressive strength, the energy absorption capacity of concrete also comes to the fore. Especially in our country, which is an earthquake country, due to the adverse environmental conditions to which the structures will be exposed, the production of additives such as fibre as well as reinforcement in concrete gains great importance. Among these fibres, the fibres that give the most effective results consist of steel and polypropylene.

In this study, a general evaluation was made regarding the various fibers used in concrete.

1.1. Literature Research

Sümer (2012) investigated the effects of the use of silica fume, an industrial waste material, in on-site concrete on concrete properties and investigated the effects on concrete properties by adding polypropylene fibre to improve

the negative effects of silica fume on concrete. Changes in compressive strength were observed when polypropylene fiber was added to concrete. Determination of compressive strength of concretes containing 10% silica fume reinforced with 0.1%, 0.5% and 1% polypropylene fiber was made on 28-day cube samples. As the amount of polypropylene fiber and silica fume increased, their compressive strength increased. The compressive strengths of 5% and 10% silica fume admixed concretes increased by approximately 23% and 35%, respectively, compared to traditional concrete.

In the study conducted by Aryan (2014) 216 g polypropylene fiber was used for the beam of 600 g/m^3 and 303 g polypropylene fiber was used for the beam of 840 g/m^3. The material weight of fine aggregate with a grain diameter of 4-12 mm is 293 kg, the mixing ratio is 15, the apparent specific gravity is 2.71 t/m^3 and the water absorption rate is 0.29%. C20 class concrete was used in the study and 12 mm long polypropylene fibers were used. S420 class ribbed reinforcement was used, and 3f12 flexural reinforcement and 2f12 compression reinforcement were used in the beams. The test specimens are 2 m long and have a cross-section of 0.20 x 0.30 m. The results obtained in this experiment are given in Table 1.

Table 1. *Experimental results (Aryan, 2014)*

Sample name	Yield load (kN)	Yield load difference (%)	Maximum displacement (mm)	Maximum displacement difference (%)	Energy absorption capacity (kN.mm)	Energy absorption capacity difference (kN.mm)	Ductility coefficient	Ductility coefficient difference (%)
Reinforced Concrete-RF	168.0	1	66.00	1	9912	1	4.71	1
Reinforced Concrete-P1	154.0	-9.09	70.00	+6.06	10076	+1.65	5.83	+23.77
Reinforced Concrete-P2	152.0	-10.52	65.00	-1.52	10329	+4.20	5.91	+25.48

In this comparison, the energy absorption capacity and ductility coefficient of reinforced concrete reference beams (P1, P2) were lower than the reinforced concrete beams with polypropylene fiber reinforcement. While the energy absorption capacity and ductility coefficient of reinforced concrete reference beams are 9912 kN/mm and 4.71, respectively, the energy absorption capacity and ductility coefficient of reinforced concrete beams with polypropylene fiber additive (P1, P2) are 10076 kN/mm and 5.83, 10329 kN/mm and 5.90, respectively. It was observed that the energy absorption capacity and ductility coefficient of the reinforced concrete reference beams were 2% lower and 23% lower, respectively, than the P1 polypropylene fiber reinforced reinforced concrete beams, while the energy absorption capacity and ductility coefficient were 4% and 25% lower, respectively, than the P2 polypropylene fiber reinforced reinforced concrete beams. According to these results (P1, P2), it was concluded that polypropylene fiber reinforced reinforced concrete beams are more ductile and their earthquake performance is better.

In the study conducted by Erdem (2019) 6 beams with the same properties were produced. Two different reinforcement ratios and three different concrete types were used in these beams. The reference beams of the study were produced with conventional C30/37 concrete, while the other beams in the study were produced using ultra-high strength concrete (average compressive strength 155 MPa) from the same matrix but containing different steel fibers. The test specimens were tested in a four-point bending setup, the strength and behavior of the test specimens under bending loads, their stiffness and ductility were examined, and the differences between the fracture mechanisms of the beams were observed. The findings obtained were analysed and presented comparatively. The results obtained are shown in Table 2.

Table 2. *Initial and yield stiffnesses of beams (Erdem, 2019)*

Specimen name	Initial crack load (kN)	Initial crack displacement (mm)	Yield load (kN)	Yield displacement (mm)	Initial Stiffness (kN/mm)	Yield Stiffness (kN/mm)
K-01	16.30	3.24	66.45	19.53	5.03	3.40
K-02	17.00	1.91	124.01	24.58	8.90	5.05
K-03	42.05	4.41	92.53	16.13	9.54	5.74
K-04	40.90	5.48	151.20	26.87	7.46	5.63
K-05	38.01	5.33	93.53	19.87	7.13	4.71
K-06	47.12	6.56	148.06	27.83	7.18	5.32

Otuzbir (2020) investigated the behavior of beams produced with steel and glass fiber polymer reinforced ultra-high performance concrete under bending effect. Compressive strength, flexural strength, elasticity modulus and energy absorption capacity of beams of ultra-high performance concretes were determined. Two different types of reinforcement placement modeled real-size beam specimens were produced. Steel fiber was used in the production of ultra-high performance concretes. It has been observed that the strength and fracture energy of glass fiber polymer reinforced beams produced with Ultra High Performance Concrete decrease under the bending effect compared to beams produced with steel reinforcement.

2. MOST USED FIBERS IN CONCRETE

Steel fiber and polypropylene fibers are most commonly used in reinforced concrete beams. Steel fibers significantly increase load carrying capacity. Polypropylene fibers significantly increase strength, ductility and energy absorption capacity. While glass fiber reduces fracture energy, it also reduces strength. Fibre materials increase the strength but negatively affect the fracture threshold (Kakooei, Akil, Jamshidi, & Rouhi, 2012; Kizilkanat, Kabay, Akyüncü, Chowdhury, & Akça, 2015; Song & Hwang, 2004; Ünal, Cengiz, & Kamanlı, 2021; Van Chanh, 2004).

These additives added to reinforced concrete elements are widely used today. Every additive has its positive aspects as well as its negative aspects. Our country, the majority of which is located in an earthquake zone, is turning to reinforced concrete structures that are advanced in terms of energy absorption and ductility. Research and experiments show that polypropylene fiber and steel fiber give positive effects. The significant increase in strength, energy absorption and ductility of polypropylene fibers has accelerated the preference for these fibers.

The method and time of use of additives are very important. For this reason, additives are added to the concrete together with the aggregate. A homogeneous distribution is aimed in fiber-reinforced concrete.

2.1. Steel fiber

Steel fibers of different types and properties are used in the reinforcement of concrete and mortar. Steel fibers, which gained importance after 1970, exhibit different properties in terms of mechanical properties, tensile strength, adherence, tension and absorption abilities because they are produced differently in terms of shape, size and surface structure (Thomas & Ramaswamy, 2007).

Steel fiber reinforced concrete is a mixed reinforced concrete in which steel fibers are regularly distributed in three dimensions into the concrete paste. It has been observed that steel fibers increase the characteristic properties of concrete such as crack resistance, ductility and permeability. The quality of fiber-reinforced concrete varies depending on the slenderness ratio and dosage of steel fibers used as additives. Depending on the selected design method, steel fiber reinforced concrete should also be selected. The most important parameters to be selected in this design method are structural safety and ductility behavior. Steel fibers act as a connection between micro cracks that begin to form as a result of shrinkage in fresh concrete paste, spreading the internal forces throughout the structure and preventing the cracks from spreading and growing under the applied loads. It prevents the concrete from losing its strength and deteriorating its structure due to its energy absorption abilities against dynamic loads such as sudden earthquakes, in addition to external loads (Song & Hwang, 2004; Van Chanh, 2004).

2.1.1. Properties of steel fiber

• Flexural strength and energy absorption capacity (toughness): The most important purpose of steel fibers is to increase the energy absorption capacity of the concrete after the crack that will occur and to reduce the bending strength to a certain limit value.

• Crack control: Steel fibers prevent crack propagation by transferring cracks with their interconnected mixture structure.

• Shock resistance: Steel fibers increase impact resistance thanks to their homogeneous distribution within the concrete paste.

• Elimination of surface swelling: In reinforced concrete structures designed with small diameter fibers compared to the concrete dimensions, discontinuous reinforcement system and high surface/volume ratio and classical iron reinforcement, swelling due to corrosion does not occur.

2.1.2. Important factors in steel fiber usage

• Concrete quality and structure for the designs of steel fiber reinforced concrete are included in TS 10514. Accordingly, the minimum cement dosage should be 320 kg/m^3 and the maximum water/cement ratio should be 0.55.

• The amount of sand should be between 40-45% of the total aggregate weight (750 kg/m^3 –850 kg/m^3).

• The maximum grain size should not exceed the limit values of 28 mm for natural aggregates and 32 mm for crushed stones. The proportion of aggregate with a grain size larger than 14 mm should be between the limit values of 15-20%.

• The compressive strength of the concrete should not be lower than 20 N/mm^2.

• To increase the workability of concrete, fluidity enhancing additives are used.

2.2. Polypropylene fiber

Polypropylene fibers are a derivative of petroleum and are an organic material widely used in the construction industry due to their physical and chemical properties. It is widely used all over the world to micro-reinforce inorganic binders such as cement and gypsum and organic binders such as bitumen and to improve their durability properties. The most important feature of polypropylene fibers in concrete is to control cracking due to plastic shrinkage that occurs within the first few hours of pouring the concrete. Polypropylene fibers are a micro reinforcement system used for concrete, plaster, screed, gypsum, bitumen and precast applications. Polypropylene fibers are produced in a wide variety of sizes (Sun & Xu, 2009).

2.2.1. Properties of polypropylene fiber

Polypropylene fibers;

- Reduces shrinkage cracks in concrete,
- It reinforces the concrete in three dimensions,
- It reduces segregation,
- It makes the concrete ductile and reduces its permeability,

- Increases the impact resistance of concrete,
- Increases the compressive and flexural strength of concrete,
- It is not affected by acids and bases and delays the corrosion and rust of the reinforcement,
- It prevents concrete from breaking up and disintegrating,
- Structures are less damaged in earthquakes and the risk of collapse is reduced,
- Increases the durability of concrete and prevents swelling of concrete in molds,
- It increases fatigue strength and increases the service life of concrete,
- Increases resistance to corrosive chemicals,
- Prevents surface wear, chipping and flaking.

2.2.2. Application areas of polypropylene fibers

- Field Concretes and Screed Applications: This is the application area where polypropylene fibers are most widely preferred. It is the most economical and practical method to prevent plastic shrinkage, plastic collapse and shrinkage cracking. In addition, it provides surface abrasion resistance. Flaking and crumbling are eliminated. Allows for minimum thinness screed pouring. In addition, it is used as a secondary reinforcement system instead of mesh reinforcement which is not used as a carrier.

- Structural Load-Bearing Reinforced Concrete Systems: In systems such as columns and beams of prefabricated and traditional structures, polypropylene fibers work parallel to the stirrups, slightly increasing the energy absorption capacity of the structure against sudden and severe impact loads such as earthquakes.

- Repair and Adhesive Mortars: When Polypropylene fiber is used in repair mortars and fillers, which are widely used to eliminate construction defects, the durability of the composite material obtained will increase and shrinkage problems will be eliminated. Polypropylene fibers can be used instead of flax, straw, goat hair, etc. in special mixture mortars prepared for the renovation of historical buildings. Polypropylene fibers also increase adherence in bonding polystyrene sheet systems for sheathing purposes.

- Structural Prefabricated Elements: It is possible to prevent breakages, deterioration in surface quality, collapse problems and thermal cracks caused by curing that occur during demoulding of reinforced concrete pipes, precast facade cladding elements, copings, sills and jambs and prefabricated building elements by using polypropylene fibers.

• Bituminous Mixtures: Polypropylene fibers are used for modification purposes in bituminous mixtures and asphalt applications to eliminate the brittleness of the mixtures at low temperatures.

• Sprayed Concrete: Fall-back, which is the biggest cost factor in shotcrete applications, can be reduced to 5% with the use of polypropylene fibers.

• Polypropylene fibers increase the ability of concrete to adhere to the surface, while providing rebound and splash control from the surface. It provides ease of application to the operator by providing homogeneous and continuous material flow. Reduces sagging and scattering in slope, vertical and overhead applications (Ahmed, Ali, & Zidan, 2020; Bei-Xing, Ming-xiang, Fang, & Lu-ping, 2004).

Aryan (2014) strengthened a reinforced concrete beam with polypropylene fiber and subjected it to load. The yield strength of the reinforced concrete RF beam is higher than the reinforced concrete P1 beam, and the P1 beam is higher than the P2 beam. The energy absorption capacity and ductility coefficient of the reinforced concrete reference beams are 2% lower and 23% lower, respectively, than the P1 polypropylene fiber reinforced reinforced concrete beams. It was also observed that the energy absorption capacity and ductility coefficient of the reference beams are 4% lower and 25% lower, respectively, than the P2 polypropylene fiber reinforced reinforced concrete beams.

In this comparison, the energy absorption capacity and ductility coefficient of reinforced concrete reference beams (P1, P2) were lower than the energy absorption capacity and ductility coefficient of reinforced concrete beams with polypropylene fiber reinforcement. While the energy absorption capacity and ductility coefficient of reinforced concrete reference beams are 9912 kN.mm and 4.71, respectively, the energy absorption capacity and ductility coefficient of reinforced concrete beams with polypropylene fiber additive (P1, P2) are 10076 kN.mm and 5.83, 10329 kN.mm and 5.90, respectively. The energy absorption capacity and ductility coefficient of the reinforced concrete reference beams were 2% and 23% lower than the P1 polypropylene fiber reinforced concrete beams, while the energy absorption capacity and ductility coefficient were 4% and 25% lower than the P2 polypropylene fiber reinforced concrete beams. According to these results (P1, P2), it was concluded that polypropylene fiber reinforced reinforced concrete beams are more ductile and their earthquake performance is better.

2.3. Glass fiber

The production of thread and various products made from glass dates back to ancient times. Glass fiber was produced by R. F. de Reaumur in 1734, but its production in a factory was realized in the late 18th century. In 1935,

Owens-Illinois Glass Co. of Newark produced glass fibres fine enough to be spun into yarn and woven. It was first used in the aerospace industry in 1942 as a reinforced composite material. High strength glass fiber (S-type) was first used in the early 1960s as a result of the joint work of O. Corning Textile Products and the US Air Force. By 1968, S-2 type glass fiber began to find use in a wide variety of commercial applications. Later, with the development of many fiber spinning methods, the production of glass fibers increased rapidly. This rate reached 2.9 million tons/year in the 2000s (Morampudi, Namala, Gajjela, Barath, & Prudhvi, 2021; Özdemir, Mecit, Seventekin, & Öktem, 2006).

2.3.1. Properties of glass fiber

Glass fibers are transparent and have smooth surfaces. They are also circular in cross-section. Their fineness varies between 2 and 13 μ. The surface of 1 kg of glass fiber with a thickness of 6μ is 280 m^2. Glass fibers are known for their high strength and their tenacity generally varies between 6-7.3 gr/denier. However, the strength of thin fibers is better than that of thick fibers. Their elongation percentage at break is around 2%, which is quite low compared to other fibers. However, for type C fibers this rate can be as high as 3-4%. Their density is 2.5-2.7 g/cm^3. 1 denier is the weight in grams of 9000 meters of yarn. The specific gravity of wool glass made from glass fibers is around 0.025 g/cm^3, which is considered low compared to normal glass fibers. Because these fibers contain large volumes of air. The amount of moisture contained in glass fibers is between 0.13-0.8%. Humidity affects the strength of glass fiber. The strength of glass fibers decreases with the increase in temperature of the environment in which they are located. The elastic modulus of uncured silicate glass fibers ranges from about 52 GPa to 87 GPa. When the fiber is heated, the modulus of elasticity gradually increases. Glass fibers do not burn, but they melt at around 1150 °C. They are resistant to acids but are affected by hot hydrofluoric acid and phosphoric acid. They are also adversely affected by concentrated bases and hot base solutions. They are not affected by many organic solvents, bacteria, moths and microorganisms. They do not conduct electricity and heat. The load-deflection relationship of a glass fiber is shown as an example in Figure 2 (Özdemir et al., 2006).

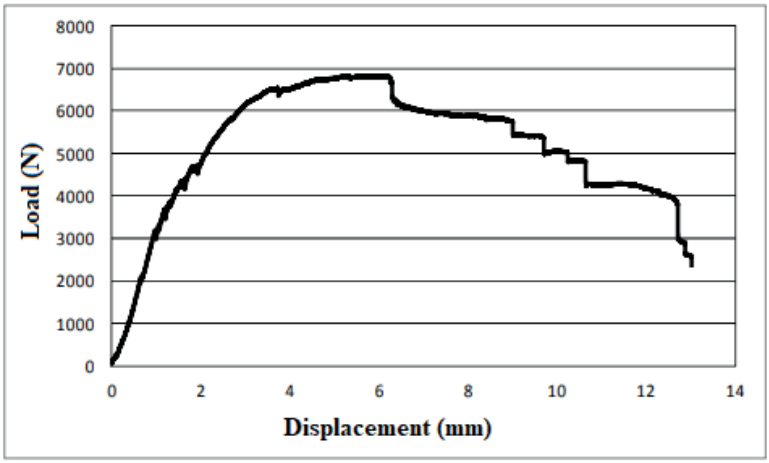

Figure 2. *Example of load-deflection relationship of a glass fiber (Mecid ve ark., 2006).*

2.3.2. Usage areas of glass fibers

• A type fiberglass – It is a type of glass fiber obtained from the recycling of scrap glass and does not have much alkali resistance.

• E type fiberglass – It is an alkali-free aluminum boron silicate glass. It is the first discovered and most produced type of glass fiber in the world. Chloride ions can melt its surface. They do not melt at high temperatures but soften.

• S type fiberglass – It is a solid glass fiber with high breaking strength.

• C type fiberglass – It is a type of glass fiber that is resistant to chemicals.

• T type fiberglass – It is the North American counterpart to C fiberglass.

• AR type fiberglass – While other types of glass fiber are water soluble and affected by pH changes, AR Glass Fiber has high alkali resistance and is therefore the most preferred in concrete production. (Ahmad et al., 2022).

The type of glass fiber used as reinforcement in the construction industry is AR type glass fiber. AR stands for "Alkali Resistant". It is undesirable to use other types of glass fiber in concrete production (Özdemir et al., 2006).

3. CONCLUSIONS AND RECOMMENDATIONS

3.1. Conclusions

Concrete is a material with a very wide range of construction applications. However, as concrete is a brittle material, in some applications it may be necessary to support it with other materials. Fibers are added to concrete to create a more ductile structures. The use of fibers in concrete is extremely important in terms of reducing shrinkage cracks in concrete, reducing

segregation, protecting the concrete against impacts, and increasing the energy absorption capacity of the structure against sudden and severe impact loads such as earthquakes. The results of the research are given below.

Since Türkiye is located on one of the world's major earthquake zones, it is frequently exposed to devastating earthquakes. Investigations after earthquakes in recent years have shown that most of the buildings were destroyed or damaged due to reasons such as not being built in accordance with the current regulations of the period in which they were built, lack of materials, and non-compliance with the project. It is seen that the majority of the buildings that are not damaged and are still in use do not meet today's regulations and are at risk of collapse in severe earthquakes. For this reason, many additives are used in reinforced concrete structural elements. These additives have positive as well as negative properties.

While steel fiber was observed to increase the load bearing capacity the most, it was also observed to reduce the initial crack load in some cases. It was found that polypropylene fiber significantly increased strength and ductility, but its load carrying capacity remained lower than that of steel and glass fibers. Silica fume also reduces the porous structure in reinforced concrete and increases strength and ductility, and it has been observed that if added in excess, it reduces strength.

- As a result of the examination carried out on reinforced concrete structures, it was observed that polypropylene fibers increased the energy absorption capacity by 4% and the ductility coefficient by 25%. The addition of polypropylene fibres has been shown to prevent concrete from dispersing and crumbling. It has been determined that buildings are less damaged in earthquakes and the risk of collapse is reduced.

- Although glass fiber has a tensile strength approximately 3 times higher than steel reinforcement due to its polymer material structure, its unit deformation is approximately 5-6 times lower than steel reinforcement. Glass fiber reinforced reinforced concrete beams had a negative effect on yield stiffness. It was observed that it positively affected the "first crack load" and "displacement" and also contributed significantly to the strength, but it was also understood that it decreased the strength with the increase in temperature.

3.2. Recommendations

As a result of this examination, it is seen that the use of fibers in concrete would be beneficial. It is expected that the use of steel fibre and glass fibre together will give good results in terms of energy absorption capacity and ductility. It is anticipated that the use of polypropylene fiber and silica fume in the same mixture will positively affect strength, ductility and load carrying capacity.

REFERENCES

Ahmad, J., González-Lezcano, R. A., Majdi, A., Ben Kahla, N., Deifalla, A. F., & El-Shorbagy, M. A. J. M. (2022). Glass fibers reinforced concrete: Overview on mechanical, durability and microstructure analysis. *15*(15), 5111.

Ahmed, T. W., Ali, A. A. M., & Zidan, R. S. (2020). Properties of high strength polypropylene fiber concrete containing recycled aggregate. *Construction Building Materials, 241*, 118010.

Aryan, A. (2014). *Polipropilen lif takviyeli betonarme kirişlerin deneysel ve analitik olarak araştırılması.* (Yüksek Lisans Tezi), Selçuk Üniversitesi Konya.

Bei-Xing, L., Ming-xiang, C., Fang, C., & Lu-ping, L. (2004). The mechanical properties of polypropylene fiber reinforced concrete. *Journal of Wuhan University of Technology-Mater. Sci. Ed., 19*, 68-71.

Erdem, Ç. (2019). *Lif katkılı yüksek mukavemetli beton ile üretilmiş elemanların eğilme davranışları.* (Yüksek Lisans Tezi), Ege Üniversitesi İzmir.

Kakooei, S., Akil, H. M., Jamshidi, M., & Rouhi, J. (2012). The effects of polypropylene fibers on the properties of reinforced concrete structures. *Construction Building Materials, 27*(1), 73-77.

Kizilkanat, A. B., Kabay, N., Akyüncü, V., Chowdhury, S., & Akça, A. H. (2015). Mechanical properties and fracture behavior of basalt and glass fiber reinforced concrete: An experimental study. *Construction Building Materials, 100*, 218-224.

Morampudi, P., Namala, K. K., Gajjela, Y. K., Barath, M., & Prudhvi, G. (2021). Review on glass fiber reinforced polymer composites. *Materials Today: Proceedings, 43*, 314-319.

Otuzbir, C. (2020). *Çelik ve cam lifi polimer donatılı ultra yüksek performanslı betonların eğilme davranışlarının incelenmesi* (Yüksek Lisans Tezi), Dokuz Eylül Üniversitesi, İzmir.

Özdemir, D., Mecit, H. D., Seventekin, N., & Öktem, T. (2006). Cam Lifleri. *Tekstil ve Konfeksiyon, 16*(1), 281-287.

Song, P., & Hwang, S. (2004). Mechanical properties of high-strength steel fiber-reinforced concrete. *Construction Building Materials, 18*(9), 669-673.

Sun, Z., & Xu, Q. (2009). Microscopic, physical and mechanical analysis of polypropylene fiber reinforced concrete. *Materials Science Engineering, 527*(1-2), 198-204.

Sümer, B. (2012). *Silis dumanı katkılı betonlarda polipropilen lif kullanımının beton özelliklerine etkilerinin araştırılması.* (Yüksek Lisans Tezi), Sakarya Üniversitesi,

Thomas, J., & Ramaswamy, A. (2007). Mechanical properties of steel fiber-reinforced concrete. *Journal of materials in civil engineering, 19*(5), 385-392.

Ünal, A., Cengiz, S., & Kamanlı, M. (2021). Effect of stirrup spacing and polypropylene fiber ratio on behavior of reinforced concrete beams. *Periodica Polytechnica Civil Engineering, 65*(2), 522-536.

Van Chanh, N. (2004). *Steel fiber reinforced concrete.* Paper presented at the Faculty of Civil Engineering Ho chi minh City university of Technology. Seminar Material.

Chapter 6

USE OF GRADIENT BOOSTING CLASSIFIER AND PERFORMANCE EVALUATION FOR DIABETES PREDICTION

Kinyas POLAT[1]

Selahattin BARDAK[2]

1 Associate Professor Kinyas POLAT, Sinop University, Faculty of Engineering and Architecture, Department of Metallurgical and Materials , Sinop, Turkey, ORCID ID:0000-0003-4574-1286

2 Professor Selahattin BARDAK, Sinop University, Faculty of Engineering and Architecture, Department of Computer Engineering, Sinop, Turkey, ORCID ID: 0000-0001-9724-4762, E-mail: sbardak@sinop.edu.tr

INTRODUCTION

High blood sugar levels are a hallmark of diabetes, a chronic illness brought on by the body's incapacity to make or utilize insulin efficiently. Diabetes is classified into two primary types: type 1, where the body fails to produce insulin, and type 2, where the body cannot effectively use the insulin it produces (World Health Organization, 2021). Millions of individuals worldwide are impacted by this critical public health issue, with an estimated 463 million adults living with diabetes in 2019, a number that is projected to rise to 700 million by 2045 (International Diabetes Federation, 2020). Diabetes may result in substantial complications such as heart disease, stroke, renal failure, and nerve damage, significantly increasing mortality and morbidity rates (World Health Organization, 2021; International Diabetes Federation, 2020).

The global prevalence of diabetes has been steadily rising over the past few decades, with the highest increase observed in low- and middle-income countries. In these regions, the rapid pace of urbanization and changes in dietary habits, combined with limited access to healthcare resources, have contributed to a surge in diabetes cases (NCD Risk Factor Collaboration, 2016). According to the Centers for Disease Control and Prevention (CDC), in 2019 alone, approximately 34.2 million people in the United States had diabetes, accounting for over 10% of the population (CDC, 2020). Furthermore, diabetes has become a leading cause of disability and reduced quality of life globally, often resulting in complications such as amputations, vision loss, and cardiovascular diseases (Einarson et al., 2018). Einarson and colleagues (2018) conducted a systematic literature review and found that the prevalence of cardiovascular disease in individuals with type 2 diabetes is significantly higher, which underlines the importance of effective management and early diagnosis.

The economic burden of diabetes is also substantial. In 2017, the global cost of diabetes was estimated at USD 727 billion, primarily due to the expenses associated with managing complications and lost productivity (International Diabetes Federation, 2020). With the increasing prevalence and the associated healthcare costs, diabetes poses a significant challenge to public health systems worldwide (NCD Risk Factor Collaboration, 2016). To avoid these complications and enhance patient outcomes, early diagnosis and implementation of optimal diabetes treatment are critical (American Diabetes Association, 2020). Effective management includes lifestyle modifications, medication adherence, and regular monitoring of blood glucose levels to prevent complications (Hahr & Molitch, 2015). The American Diabetes Association (2020) recommends a multifaceted approach to diabetes care, including dietary changes, increased physical activity, and medication management. Hahr and Molitch (2015) further highlight that

patients with comorbid conditions, such as chronic kidney disease, require tailored treatment strategies to minimize risks and improve outcomes.

Early detection is crucial, as many patients remain asymptomatic until the disease has progressed to an advanced stage (Einarson et al., 2018). Regular screening, particularly for high-risk populations, can significantly reduce the likelihood of complications and improve prognosis (Smith et al., 2019). Smith and colleagues (2019) emphasize the importance of utilizing implementation science to improve diabetes management in primary care settings, suggesting that structured protocols and health technology can play a pivotal role in enhancing care quality.

Through the analysis of enormous datasets of characteristics linked to health, machine learning approaches have shown considerable potential in the prediction and management of diabetes. To create prediction models for diabetes, prior research has used a variety of machine learning methods, such as decision trees, support vector machines, and neural networks (Choi et al., 2017; Kavakiotis et al., 2017; Abhari et al., 2019; Cho et al., 2016). These models can analyze complex and multidimensional health data, which often include demographic factors, lifestyle habits, genetic information, and laboratory test results, to identify patterns that may not be apparent through traditional statistical methods (Chen et al., 2018).

For instance, Choi et al. (2017) demonstrated that recurrent neural network models are highly effective in predicting the onset of heart failure in patients with type 2 diabetes, using longitudinal electronic health records. Similarly, Kavakiotis et al. (2017) conducted a comprehensive review of machine learning techniques used in diabetes research and identified support vector machines and decision trees as two of the most commonly used models, owing to their ability to handle both linear and non-linear relationships in data.

By combining the capabilities of multiple weak learners, ensemble learning methods such as the Gradient Boosting Classifier have proven very successful in increasing the accuracy and durability of predictive models (Friedman, 2001). Gradient boosting involves the iterative training of decision trees, where each tree corrects the errors of the previous one, resulting in a robust model that is less prone to overfitting (Friedman, 2001; Chen & Guestrin, 2016). Chen and Guestrin (2016) introduced the XGBoost framework, a scalable and efficient implementation of gradient boosting, which has been widely adopted in predictive modeling for diabetes due to its ability to handle missing data and produce high accuracy results.

In recent years, hybrid models that integrate traditional machine learning with deep learning techniques have further improved the sensitivity and specificity of diabetes prediction models (Miotto et al., 2016; Razavian et al.,

2015). Miotto et al. (2016) proposed the Deep Patient model, which leverages unsupervised deep learning to extract complex features from electronic health records, enhancing the prediction of future disease risks. This model has shown promise in identifying high-risk patients who may benefit from more intensive monitoring and intervention.

The integration of machine learning into diabetes care has significant implications for personalized medicine. Predictive models can assist clinicians in developing individualized treatment plans based on a patient's unique risk profile, optimizing the allocation of healthcare resources (Smith et al., 2019). For instance, Razavian et al. (2015) demonstrated that machine learning models could accurately predict severe diabetes complications, such as diabetic nephropathy and neuropathy, enabling early intervention.

Despite the promise of machine learning in diabetes care, challenges remain. Data privacy, model interpretability, and the need for high-quality data are critical factors that must be addressed to ensure these models are effectively integrated into clinical practice (Chen et al., 2018). As the field continues to evolve, future research should focus on developing transparent and generalizable models that can be seamlessly incorporated into existing healthcare workflows (Miotto et al., 2016).

Diabetes is a rapidly growing public health concern with significant implications for both individual health and healthcare systems globally. Early diagnosis, effective management, and the integration of advanced machine learning techniques hold promise in mitigating the disease's impact. By leveraging the predictive power of machine learning, healthcare providers can develop more targeted and personalized treatment strategies, ultimately improving patient outcomes and quality of life.

In this work, we use the Gradient Boosting Classifier to create a diabetes prediction model. We will use a dataset including different health metrics from 768 people to assess the model's performance. To improve the predicted accuracy of the model, GridSearchCV will be used to adjust its hyperparameters. Performance measures including recall, accuracy, precision, and F1 score will be used to evaluate how well the model predicts diabetes.

MODEL CHOICE

The Gradient Boosting Classifier model was selected because to its exceptional performance and capacity to identify non-linear correlations within the dataset. GridSearchCV was used for the hyperparameter tuning process.

The Gradient Boosting Classifier model was chosen for its ability to capture non-linear relationships in the dataset and its high performance. Gradient Boosting works by building an ensemble of weak learners, typically

decision trees, in a sequential manner. Each tree is trained to correct the errors of its predecessor, thereby improving the model's overall performance.

Mathematically, the Gradient Boosting algorithm minimizes a differentiable loss function $L(y, F(x))$ by iteratively adding a new tree $h_m(x)$ that points in the negative gradient direction of the loss function. The model after mmm iterations is given by:

$$F_m(x) = F_{m-1}(x) + \gamma h_m(x)$$

where γ\gamma is the learning rate that controls the contribution of each tree. The negative gradient at each iteration is computed as:

$$-[\frac{\partial L(y, F(x))}{\partial F(x)}] = F_{m-1}(x)$$

This approach allows the model to correct its errors iteratively, leading to a highly accurate predictive model capable of capturing complex patterns in the data.

PYTHON IMPLEMENTATION

The Python programming language and a number of libraries were used in this work to develop the model and carry out data analysis. Among the important libraries used are:

pandas: This package is necessary for analyzing and manipulating data. It offers data structures that are perfect for managing and examining structured data, such as DataFrame. Pandas was utilized in this research to import the dataset, preprocess the data, and carry out other data manipulation operations.

Two libraries used for data visualization are seaborn and matplotlib. Seaborn offers a high-level interface for creating visually appealing statistical visuals and is developed on top of matplotlib. A complete Python visualization toolkit for static, animated, and interactive graphics is called Matplotlib. In order to better understand the correlations between the variables in this research, visualizations like the correlation matrix were created using seaborn and matplotlib.

One of the most widely used Python libraries for machine learning is scikit-learn. It offers straightforward and effective data mining and analysis tools. The Gradient Boosting Classifier was implemented in this work using scikit-learn. GridSearchCV was used to do hyperparameter tuning, and measures including accuracy, precision, recall, and F1 score were employed to assess the model's performance.

OPTIMIZATION OF HYPERPARAMETERS

Learning rate, the number of trees (n_estimators), and the maximum depth (max_depth) were among the parameters that were improved throughout the hyperparameter optimization process. The hyperparameter grid that follows was employed:

```
param_grid = {
  'learning_rate': [0.01, 0.1, 0.05],
  'n_estimators': [100, 200, 300],
  'max_depth': [3, 4, 5]}
```

CORRELATION MATRIX

To investigate the connections between the variables in the dataset, a correlation matrix was constructed and represented as it is displayed below. Strong correlations between several variables were shown by the correlation matrix.

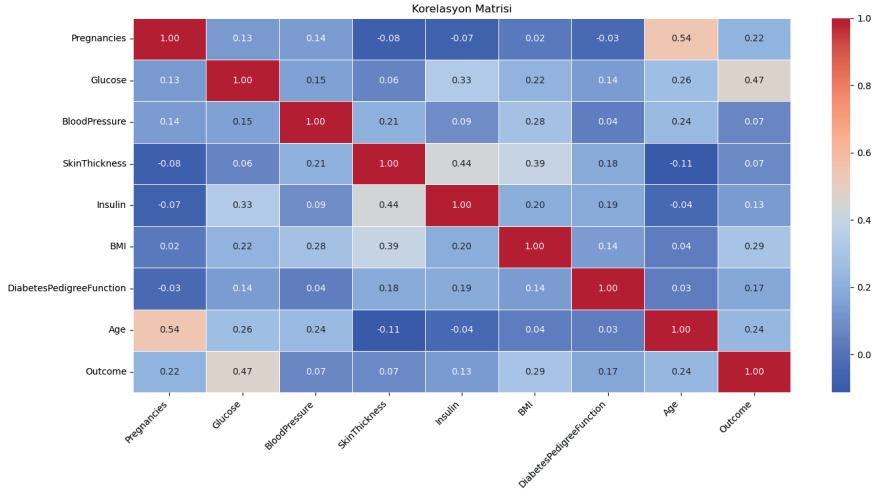

Glucose and outcome: The result of diabetes and glucose levels have a significant positive connection (0.47). This suggests that there is a substantial correlation between having higher blood sugar and a greater chance of developing diabetes, which is consistent with medical understanding that elevated blood sugar is a major marker of diabetes.

Age and outcome: The association between age and the result of diabetes is somewhat favorable (0.24). The idea that the risk of diabetes rises with age is consistent with the fact that older people often have a greater risk of the disease.

BMI and outcome: Patients with higher BMIs are more likely to develop diabetes, according to the 0.31 connection found between BMI and diabetes result. This bolsters the established link between diabetes risk and fat.

Insulin and Glucose: The relationship between insulin and glucose is somewhat favorable (0.34). Especially in those who are insulin resistant, higher insulin doses are often needed to control elevated glucose levels.

The correlation matrix aids in determining which factors are highly correlated and may have a greater bearing on diabetes prediction. We may choose features and train models in an educated manner by being aware of these linkages.

RESULTS

MODEL PERFORMANCE

The performance of the model was evaluated using four main metrics: accuracy, precision, recall, and F1 score. Each of these metrics provides unique insights into how well the model performs in distinguishing between diabetic and non-diabetic individuals. The achieved accuracy of the model is 74.0%, which indicates that 74% of the predictions made by the model are correct. While this is a satisfactory baseline, it leaves room for improvement, as ideally, a higher accuracy rate would be preferred, especially in critical applications such as healthcare, where misdiagnosis can have serious consequences.

The precision of the model is 62.7%, suggesting that out of all the individuals predicted to have diabetes, only 62.7% are actually diabetic. A lower precision indicates the presence of false positives cases where the model incorrectly flags healthy individuals as diabetic. This may lead to unnecessary anxiety and additional medical tests for these individuals, highlighting a potential issue with the model's robustness.

The recall is calculated as 67.3%, which indicates that 67.3% of the actual diabetic patients were correctly identified by the model. A low recall score points to the existence of false negatives, where individuals who genuinely have diabetes are not flagged by the model. In healthcare, false negatives are particularly dangerous, as they can delay necessary treatment for at-risk patients.

The F1 score, which is the harmonic mean of precision and recall, is 64.9%. This metric balances the trade-off between precision and recall, making it a good indicator of the model's overall performance, especially in cases of imbalanced datasets. A F1 score close to 65% suggests that while the model is relatively effective, it still has room for refinement to handle the complexity of predicting diabetes more accurately.

The hyperparameter tuning was conducted using GridSearchCV, which identified the optimal combination of parameters for improving the model's performance. The best parameters included a learning rate of 0.05, 200 trees (estimators), and a maximum depth of 4 for each decision tree. A learning rate of 0.05 suggests that the model updates its predictions slowly during training, which helps prevent overfitting. The choice of 200 trees implies that the model benefits from a relatively larger number of iterations, ensuring that the final decision boundaries are more refined. A maximum depth of 4 indicates that the trees are not too deep, thereby avoiding unnecessary complexity and reducing the risk of overfitting.

DISCUSSION

The model's performance, as demonstrated by the metrics, is reasonably good but not without limitations. The accuracy of 74% and F1 score of 64.9% suggest that while the model can distinguish between diabetic and non-diabetic individuals to a certain extent, there is a significant proportion of false positives and false negatives. This observation is supported by the low precision (62.7%) and recall (67.3%) values, which indicate that the model misclassifies both healthy and diabetic individuals at a non-negligible rate.

One reason for the lower performance might be the complexity and heterogeneity of diabetes as a disease. Diabetes is influenced by numerous factors, including genetic predisposition, lifestyle, age, and comorbid conditions. As a result, it is challenging for a single model to capture all these nuances accurately. Moreover, the data might be imbalanced, with more non-diabetic samples compared to diabetic ones, which could skew the model's learning process.

To improve the model's performance, additional feature engineering and the inclusion of more relevant health indicators, such as family medical history or genetic factors, could be beneficial. Furthermore, techniques like SMOTE (Synthetic Minority Over-sampling Technique) can be employed to balance the dataset, thereby reducing the impact of imbalanced classes. Another approach could be to experiment with other algorithms, such as random forests or support vector machines, to see if they offer better performance. Ultimately, while the model provides a solid foundation, it requires further refinement to be reliably used for diabetes prediction in clinical settings.

FUTURE WORK

Future studies should focus on collecting more data, experimenting with different models, and performing feature engineering. Additionally, prospective studies are needed to evaluate the model's application in clinical settings.

REFERENCES

Abhari, S., Niakan Kalhori, S. R., Hashemi, S., Fatehi, F., & Ghazisaeedi, M. (2019). Artificial neural network models for prediction of type 2 diabetes: A systematic review of the literature. Journal of Diabetes Research, 2019, 1-10. https://doi.org/10.1155/2019/3158673

American Diabetes Association. (2020). Standards of medical care in diabetes—2020 abridged for primary care providers. Clinical Diabetes, 38(1), 10-38. https://doi.org/10.2337/cd20-as01

Centers for Disease Control and Prevention. (2020). National Diabetes Statistics Report, 2020. U.S. Department of Health and Human Services, Centers for Disease Control and Prevention. Retrieved from https://www.cdc.gov/diabetes/library/features/diabetes-stat-report.html

Chen, T., & Guestrin, C. (2016). XGBoost: A scalable tree boosting system. In Proceedings of the 22nd ACM SIGKDD International Conference on Knowledge Discovery and Data Mining (pp. 785-794). https://doi.org/10.1145/2939672.2939785

Chen, J., Liu, C., & Hsu, H. (2018). Diabetes prediction using deep learning with feature selection and risk factor analysis. BMC Medical Informatics and Decision Making, 18(1), 1-8. https://doi.org/10.1186/s12911-018-0599-8

Cho, K., Van Merriënboer, B., Bahdanau, D., & Bengio, Y. (2016). On the properties of neural machine translation: Encoder-decoder approaches. In Proceedings of SSST-8, Eighth Workshop on Syntax, Semantics and Structure in Statistical Translation (pp. 103-111). https://doi.org/10.3115/v1/W14-4017

Choi, E., Schuetz, A., Stewart, W. F., & Sun, J. (2017). Using recurrent neural network models for early detection of heart failure onset. Journal of the American Medical Informatics Association, 24(2), 361-370. https://doi.org/10.1093/jamia/ocw112

Einarson, T. R., Acs, A., Ludwig, C., & Panton, U. H. (2018). Prevalence of cardiovascular disease in type 2 diabetes: A systematic literature review of scientific evidence from across the world in 2007–2017. Cardiovascular Diabetology, 17(1), 1-19. https://doi.org/10.1186/s12933-018-0728-6

Friedman, J. H. (2001). Greedy function approximation: A gradient boosting machine. Annals of Statistics, 29(5), 1189-1232. https://doi.org/10.1214/aos/1013203451

Hahr, A. J., & Molitch, M. E. (2015). Management of diabetes mellitus in patients with chronic kidney disease. Clinical Diabetes and Endocrinology, 1(1), 1-9. https://doi.org/10.1186/s40842-015-0001-9

International Diabetes Federation. (2020). IDF Diabetes Atlas, 9th edition. International Diabetes Federation. Retrieved from https://diabetesatlas.org

Kavakiotis, I., Tsave, O., Salifoglou, A., Maglaveras, N., Vlahavas, I., & Chouvarda, I. (2017). Machine learning and data mining methods in diabetes research. Computational and Structural Biotechnology Journal, 15, 104-116. https://doi.org/10.1016/j.csbj.2016.12.005

Miotto, R., Li, L., Kidd, B. A., & Dudley, J. T. (2016). Deep patient: An unsupervised representation to predict the future of patients from the electronic health records. Scientific Reports, 6(1), 1-10. https://doi.org/10.1038/srep26094

NCD Risk Factor Collaboration. (2016). Worldwide trends in diabetes since 1980: A pooled analysis of 751 population-based studies with 4.4 million participants. The Lancet, 387(10027), 1513-1530. https://doi.org/10.1016/S0140-6736(16)00618-8

Razavian, N., Marcus, J., Sontag, D., & Seifter, A. (2015). A machine learning approach to predict severe diabetes complications. Journal of Diabetes Research, 2015, 1-10. https://doi.org/10.1155/2015/618968

Smith, J. D., Polaha, J., Muench, J., O'Keefe, M., & Carroll, A. (2019). Using implementation science to improve the management of chronic disease in primary care. The Journal of Primary Prevention, 40(1), 1-11. https://doi.org/10.1007/s10935-018-0537-9

World Health Organization. (2021). Diabetes. World Health Organization. Retrieved from https://www.who.int/news-room/fact-sheets/detail/diabetes

Chapter 7

ARTIFICIAL INTELLIGENCE BASED DEEP LEARNING SURROGATE MODEL FOR DESIGN OPTIMIZATION OF MICROSTRIP FREQUENCY SELECTIVE SURFACE AND GAIN IMPROVEMENT OF PATCH ANTENNA

Burak Dokmetas[1], Shivani S. Shinde[2], Tarlan Mahouti[3], Mehmet Ali Belen[4]

1 Asst. Prof. Dr. Burak Dökmetaş, Kafkas University, https://orcid.org/0000-0001-5900-6691, burakd@kafkas.edu.tr
2 Shivani S. Shinde, G. H. Raisoni College of Engineering, Nagpur, shivanishivajishinde01@gmail.com
3 Tarlan Mahouti, Yıldız Teknik University, https://orcid.org/0000-0001-5178-4878, tarlan.mahouti@gmail.com
4 Assoc. Prof. Dr. Mehmet Ali Belen, İskenderun Teknik University, https://orcid.org/0000-0001-5588-9407, mali.belen@iste.edu.tr

I. Introduction

The rapid advancements in artificial intelligence (AI) and deep learning have brought significant changes to the field of electromagnetic design, particularly in the optimization of microstrip frequency selective surfaces (FSS) and patch antennas [1]. Traditionally, the design of these components has relied on iterative methods and extensive computational simulations to explore the complex design space and achieve desired performance metrics, such as gain improvement and frequency selectivity. These conventional approaches, however, often struggle to efficiently capture the intricate dependencies between various design parameters and the resulting electromagnetic behaviour [2].

Despite the advantage of providing high-precision measurements, EM simulations are disadvantageous in solving computationally large and complex problems such as optimization and tolerance analysis. The duration of the EM simulation can take a very long time depending on the granularity of the optimization targets [3]. One of the recommended approaches to reduce this time and obtain more effective results is the Data-driven surrogate model [4-5]. The effective utilization of contemporary AI methodologies and optimization techniques have proven to be efficient approaches in achieving exceptional levels of EM-performances.

AI-based deep learning techniques have emerged as powerful tools to address these challenges by developing surrogate models that can predict the performance of microstrip FSS and patch antennas with high accuracy and significantly reduced computational effort. These models leverage the capabilities of deep learning to model the nonlinear and complex interactions inherent in electromagnetic designs, enabling rapid optimization and real-time decision-making throughout the design process [6].

This paper introduces, a novel approach to the design of FSS, leveraging artificial intelligence, is explored. The M2LP architecture is highlighted as an advanced AI regression model that enhances traditional artificial neural networks by incorporating sophisticated elements from Deep Neural Networks (DNN). These advanced components include modern activation functions such as ReLU and ELU, which help to mitigate vanishing gradient issues and improve the convergence rate during the training process. Additionally, batch normalization is utilized, a technique designed to

address the internal covariate shift problem. The techniques examined in this study aim to introduce a new perspective to FSS design.

II. FSS AND SURROGATE MODEL

In this section, artificial intelligence algorithms used for regression modeling are introduced. These algorithms used will help in finding the modeling that best optimizes the resonance response of the FSS according to geometric parameters. The best of these algorithms was chosen and modeling was done based on this algorithm.

A. Support Vector Regression Machine

Support Vector Machines (SVM) have proven to be highly effective in classification and regression tasks in recent years. SVM is a fast-learning algorithm grounded in robust mathematical principles that link generalization with optimization theories[7-8]. These algorithms are particularly well-suited for handling regression with complex non-linear functions, as they operate in an appropriate feature space where these non-linear functions can be treated as linear ones. SVM has garnered increasing attention in both theoretical and engineering contexts due to its numerous advantageous features. It is widely applied in areas such as pattern recognition, voice recognition, function estimation, and optimal control. The primary domains where SVM is applied include engineering and economics, where it serves as a solution method for classification, regression, and prediction problems. SVM learning theory is built on the principle of utilizing a small sample size rather than an infinite number of samples, which results in lower computational costs [9].

The use of a convex objective function in the optimization process ensures a universal minimum, and unlike Artificial Neural Networks (ANN), SVM minimizes the coefficients of the approximation function (structural risk) rather than the empirical risk. This approach provides a comprehensive risk minimization strategy for a learning machine. With these core principles, SVM offers distinct advantages over other methodsChoosing the right kernel is the trickiest part of SVM problems [10]. Some of the most used kernel functions are p ranked kernel, p-order polynomial kernel, and Sigmoid kernel. They are given in the Eq. (1), Eq. (2) and Eq. (3) respectively.

$$K(u,v) = (<u,v>)^p \qquad (1)$$

$$K(u,v) = (<u,v> +1)^p \quad (2)$$

$$K(u,v) = tanh\ (a <u,v> -\gamma) \quad (3)$$

B. ***Gaussian Process Regression***

Gaussian Process Regression (GPR) models are typically utilized in scenarios involving non-linear regression and classification due to their powerful capability to model complex relationships between variables. A key advantage of GPR is its ability to provide probabilistic predictions, which means that, in addition to predicting the expected value, GPR also estimates the uncertainty of the predictions. This probabilistic nature allows for the calculation of empirical confidence intervals, offering a quantifiable measure of prediction reliability. These confidence intervals are particularly useful in identifying regions where the model's predictions may be less certain, thus guiding the decision on whether additional data or adjustments are needed in those areas [11].

The Gaussian process f(x) is parameterized with m(x) evaluated at points x and x′. The function can be defined as:

$$m(x) = E\ (f(x)) \quad (4)$$

$$Cov(f(x)),f(x')) = k(x, x';\theta) =$$

$$E((f(x)-m(x))f(x')-m(x'))) \quad (5)$$

Here, "θ" denotes the set of hyperparameters.

The mean function is generally considered zero because it expresses the central tendency of the function [12]. The covariance function contains information about the shape and structure of the function to be created [13]. The connection between input and output parameters is stated as follows:

$$y = f(x) + \varepsilon \quad (6)$$

Here, the value of ε is assumed to be independent and a Gaussian distribution with zero mean and variance of σ_n^2 is distributed over it.

C. ***Ensemble Learning***

Ensemble learning (EN) is a machine learning approach that involves the combination of multiple base models to create a single, highly effective predictive model. This method is particularly advantageous in cases where complex decision boundaries are present, as relying on a single classifier may not provide sufficient accuracy or robustness. By aggregating the predictions from several different models, ensemble learning can enhance

overall performance, reduce the risk of overfitting, and improve generalization to unseen data. This technique is especially beneficial in scenarios where individual models may struggle to capture intricate patterns within the data, making ensemble methods a powerful tool in tackling challenging predictive tasks [14].

D. ***Multi-Layer Perceptron***

Multilayer perceptrons (MLPs) are a type of artificial neural network particularly suited for situations where the relationship between input and output variables is nonlinear. MLPs are highly effective in tasks involving classification and generalization, where capturing complex patterns in the data is crucial. These networks consist of multiple layers, including one or more hidden layers, that process information received from the input layer and pass it on to subsequent layers. The presence of multiple hidden layers allows MLPs to model and solve complex problems by learning intricate features and representations within the data. This layered structure enhances the network's ability to handle challenging tasks that simpler models might not adequately address, making MLPs a powerful tool for a wide range of applications in machine learning [15].

E. ***Modified Multi-Layer Perceptron***

The goal of the Multi-Layer Perceptron (MLP) model is to reduce error, or the discrepancy between the network's output and the actual output. By spreading the error throughout the network, this is accomplished. Because of this, the MLP model is sometimes referred to as the Error Propagation or Backpropagation model. The input layer, hidden layer (intermediate layer), and output layer make up the three layers of the MLP model. There may be more than one concealed layer. The input layer is in charge of making sure that inputs from the outside world are sent to the hidden layer; it is not tasked with processing information. Hidden layers process information from the input layer or the information from the previous intermediate layer. The output layer produces the output of the network by processing the information coming from the intermediate layer [16].

Modified Multi-Layer Perceptron (M2LP) is an equivalent convolutional neural network model of the standard multilayer perceptron (MLP). Instead of the traditional training parameters of MLP, more advanced training parameters such as rectified linear unit (ReLU) and Adam training algorithm have been used [15]. A modified multilayer regression (M2LP) perceptron was used to estimate the scattering parameters of the nonuniform microstrip transmission line [17-18].

F. ***Proposed FSS Design***

The proposed FSS design is represented in Figures 1-2. Design variables and their variation limits of the proposed FSS design are given in Table 1. Parametric analyses have a crucial role in scientific and technical research, particularly in the development and optimization of complex systems and materials. The effect of altering specific design factors, such as the "Gap," on scattering parameters is thoroughly investigated in the study of frequency selective surfaces (FSSs) (Figure 3). This extensive analysis achieves two significant goals: (I) it generates a critical idea about the dataset that will be used in Machine Learning (ML) algorithms later on; and (II) it clarifies the precise influence of individual parameters on the performance characteristics of the FSS. It is not only a matter of academic integrity. Despite the existence of multiple relevant variables, the focus on the parametric analysis of a single parameter is justified by the need to speed the research and enhance the clarity of the findings. Researchers are able to provide a detailed, thorough, and quantitative explanation of how this specific design feature influences the behavior of the FSS by isolating the effect of the "Gap" parameter. It is simpler to communicate the information in a clear and understandable way with this targeted approach, which is particularly beneficial for academic papers where length and reader comprehension are crucial considerations. In this work the model is built using 500 training samples generated via Latin-Hypercube Sampling (LHS), alongside 100 hold-out samples. Each sample represents an evaluation of the scattering parameter vector within the frequency range of 2 to 10 GHz, with a 0.1 GHz increment. The results of the mentioned algorithms and their corresponding parameters are given in Table 2.

A crucial aspect of developing and optimizing Artificial Intelligence (AI) algorithms is hyperparameter optimization, particularly in the context of regression studies, which are essential for modeling and forecasting the behavior of microwave components. The selection of suitable hyperparameters, which, in contrast to model parameters learned during training, must be established prior to the training process, is a major determinant of the performance of these AI models. These hyperparameters might be anything from neural network architectural details to regularization coefficients and learning rates. For predictive models to have high levels of efficiency, generalizability, and accuracy, their ideal design is essential.

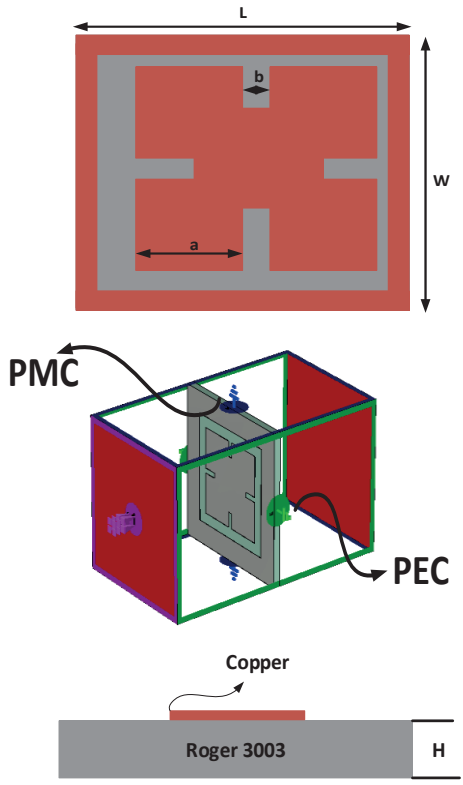

Fig 1. Schematic of the proposed FSS structure

TABLE I. DESIGN VARIABLES AND THEIR VARIATION LIMITS

Parameter	Lower	Upper
L	10	30
W	10	30
a	5	20
b	5	20

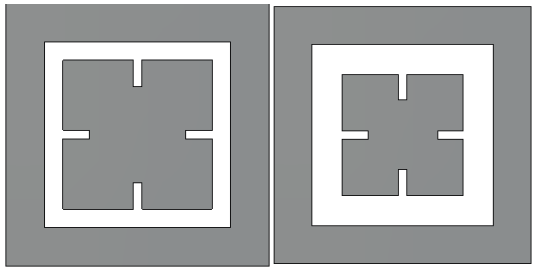

(a) (b)

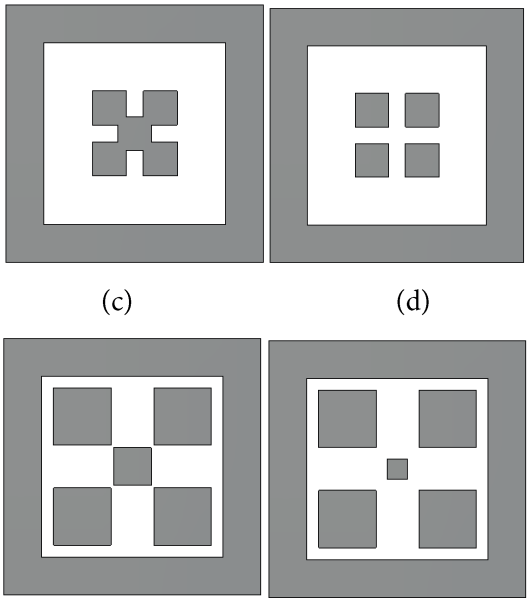

Figure. 2. Geometrical variation of unit cell element for different design parameter combinations.

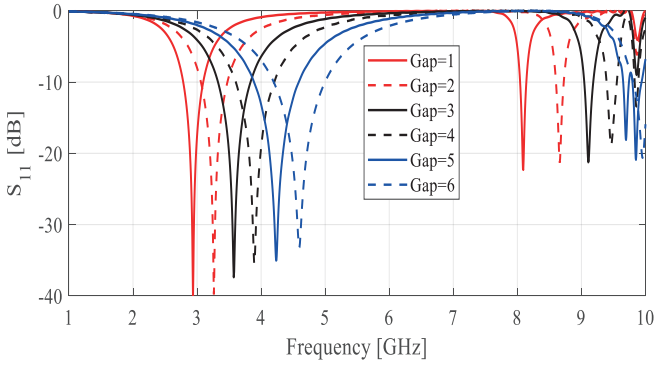

(a)

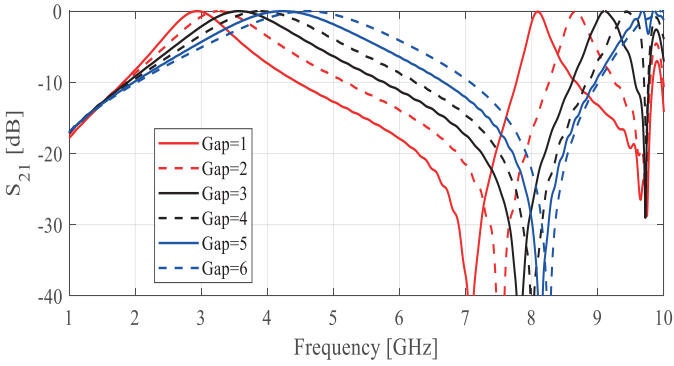

(b)

Figure. 3. Scattering parameter (a) S_{11} (b) S_{21}, responses of the unit cell for variation of parameter "Gap" over the operation band.

TABLE II. RME VALUES OF SURROGATE MODELS

Model	Hyper-Parameters	K-fold/Holdout
SVM	Kernel-function: Gaussian,Epsilon: 0.42	9.2% / 10.4 %
EN	hyperpar.learningrate=0.035 hyperpar.Numestimators=3200	7.9% / 9.1%
GPR	Kernel-function:ardmatern 3/2; Prediction-method: Block-coordinate-descent;block-size:500	5.1% / 6.8%
M2LP	Hyperpar.depth=3 Hyperpar.initial_num_neuron=64	4.1% /4.9 %

III. FSS RESULTS AND DISCUSSION

Based on the findings from Table 2, the M2LP algorithm was selected for the design of Frequency Selective Surfaces (FSS). Among various optimization techniques, the Honey Bee Mating Optimization (HBMO) algorithm was chosen to act as the search engine for the optimization process. The HBMO algorithm, inspired by the complex mating behavior of honey bees, involves a sophisticated process of selection, mating, and mutation to discover optimal solutions. When applied to FSS design, HBMO is effectively utilized to identify the optimal set of design variables that achieve the desired electromagnetic performance [19].

To validate the proposed M2LP model, a comparative study was conducted using an electromagnetic (EM) simulation program. The results for the S11 and S21 parameters are presented in Figures 4 and 5, respectively. The

results indicate that the proposed method is consistent, with the differences in response primarily occurring in regions where the scattering parameters are below -10 dB. This level of discrepancy is within the same magnitude as the model's test error (Table II), demonstrating that the M2LP model provides reliable predictions that closely match the EM simulation results. This consistency underscores the effectiveness of the M2LP algorithm in accurately capturing the essential characteristics of the FSS design.

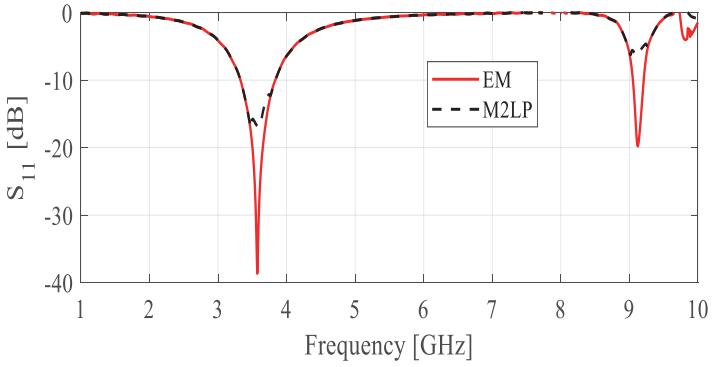

Figure 4. The S_{11} results of the proposed FSS structure

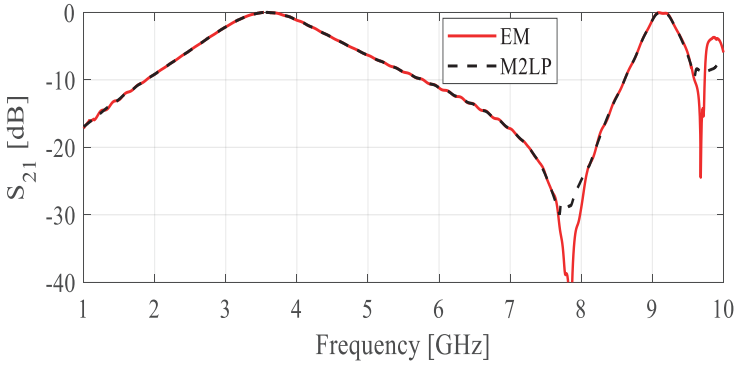

Figure 5. The S_{21} results of the proposed FSS structure

IV. APPLICATION: GAIN IMPROVEMENT OF PATCH ANTENNA

In this section, the application of Frequency Selective Surface (FSS) for enhancing the gain of a patch antenna is explored. The patch antenna (Table III), as shown in the figures (Fig 6), is constructed on an FR4 substrate with a dielectric constant of 4.4, as depicted in the first image. The antenna is designed to operate in the microwave frequency range, and the inclusion of an FSS aims to enhance its performance, particularly by improving its gain and impedance matching.

The FSS unit cell, illustrated in the second image, is a periodic structure that interacts with incoming electromagnetic waves, resulting in a resonant behavior that enhances the antenna's electromagnetic properties. When the FSS is positioned close to the patch antenna, it modifies the surrounding electromagnetic field, directly affecting the antenna's scattering parameters (S11) and gain.

The effectiveness of the FSS in improving the antenna's performance is demonstrated through the S11 and gain plots shown in the third and fourth figures, respectively. The S11 comparison reveals that the integration of the FSS shifts the resonant frequencies and significantly enhances impedance matching, particularly around the 3.6 GHz band (Fig 7). This is evidenced by the considerable dip in S11, where the reflection coefficient reaches -24 dB with the FSS, compared to -18 dB without it, indicating superior impedance matching and reduced return loss.

The gain improvement is especially noticeable in the gain plot, where the patch antenna with FSS (represented by the red dashed line) shows a significant gain increase across the frequency spectrum, with a peak around the resonance frequency. Specifically, at 3.6 GHz, the gain of the antenna with FSS is 7.2 dBi, compared to 4.1 dBi for the antenna without FSS, as detailed in Table IV. This increase of over 3 dB demonstrates the FSS's effectiveness in enhancing the radiation efficiency and overall performance of the patch antenna.

Furthermore, Table V presents a performance comparison of the proposed antenna with other works in the literature. The comparison highlights that the proposed antenna, operating at 3.6 GHz with a compact size of 60x60x12 mm, achieves a significant S11 of -24 dB and a gain of 7.2 dBi using an FR4 substrate. When compared to similar designs in the literature, the proposed antenna demonstrates a competitive performance, especially considering its compact size and the utilization of a single-layer FSS. For instance, the work in [24] achieved a higher gain of 13.9 dBi but required a much larger structure (120x120x30 mm) and a more expensive substrate (Taconic TLC Roger5880). The proposed design strikes a balance between size, cost, and performance, making it a practical and efficient solution for applications requiring high gain and compact antenna structures.

Overall, the results confirm that the integration of FSS with patch antennas is an effective strategy for enhancing gain, optimizing impedance matching, and improving overall antenna performance. This approach offers significant advantages in high-frequency applications where compact, high-performance antennas are required. The proposed FSS-loaded patch antenna demonstrates clear benefits over traditional designs, making it a promising candidate for a wide range of microwave applications.

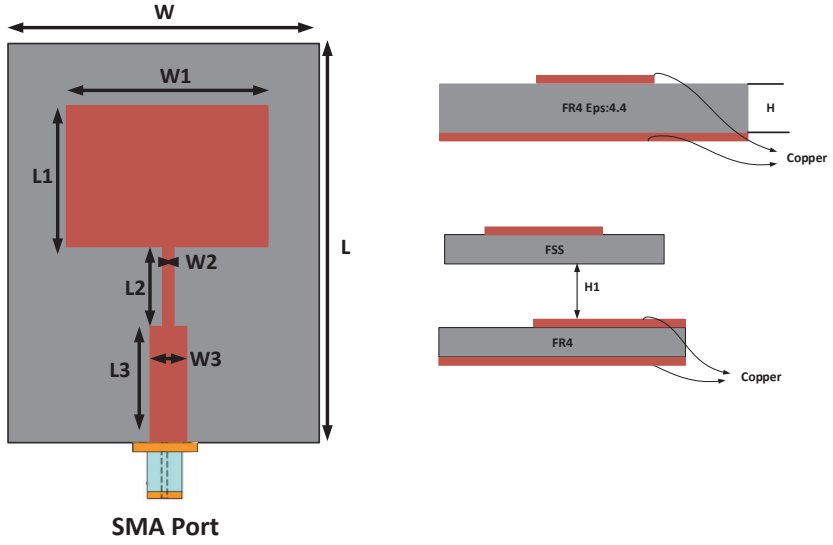

(a)

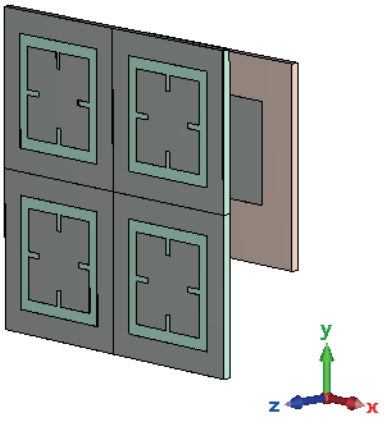

(b)

Fig 6. (a) Schematic, (b) 3D, view of the proposed patch antenna

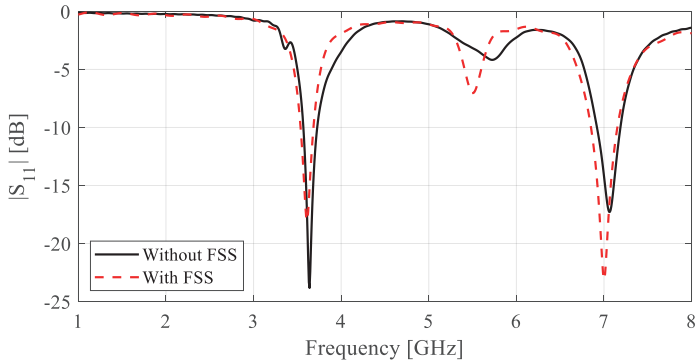

(a)

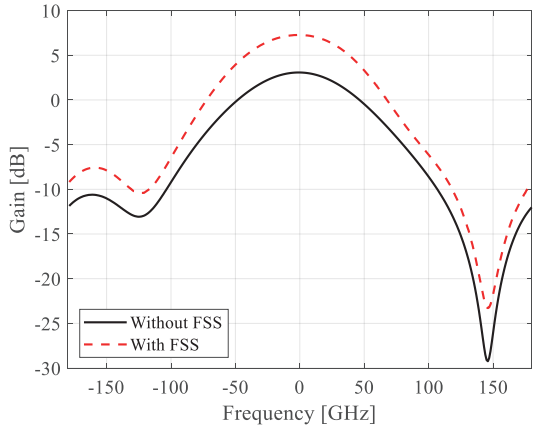

(b)

Fig 7. Measured (a) S11, (b) radiation pattern @ 2.4 GHz, results of the proposed antenna

TABLE III. ANTENNA PARAMETER (MM)

W	40.88	L	38.2
W1	24.8	L1	19.2
W2	1.2	L2	5
W3	3	L3	6
H1	10	FR4	H:1.56mm eps:4.6

TABLE IV. SIMULATED PERFORMANCE RESULTS OF THE PROPOSED FSS LOADED PATCH ANTENNA @ 3.6GHZ

Model	S_{11}(dB)	Gain (dBi)
Patch Antenna With FSS	-24	7.2
Patch Antenna without FSS	-18	4.1

TABLE V. PERFORMANCE COMPARISON OF PROPOSED ANTENNA WITH COUNTERPART WORKS IN LITERATURE

Model	*f (GHz)*	Size (mm)	Layer	S11 dB	Gain dBi	Substrate
[20]	2.4	63.65x54.16x10	Dual layer FSS	-14	6.5	FR4
[21]	2.55	315x315x30		---	7.6	
[22]	3.53	105x175x50	Single Layer FSS	-20	13	
[23]	2.4	63.65x54.16x12	SIW FSS	-16	4.7	
[24]	2.6	120x120x30	Single Layer FSS	-25	13.9	Taconic TLC Roger5880
In this paper	3.6	60x60x12	Patch-FSS	-24	7.2	FR4

V. CONCLUSION

This study successfully demonstrated the efficacy of combining Artificial Intelligence (AI)-based surrogate modeling with meta-heuristic optimization techniques for the design and performance enhancement of Frequency Selective Surfaces (FSS) and patch antennas. Specifically, the Modified Multi-Layer Perceptron (M2LP) model was integrated with the Honey Bee Mating Optimization (HBMO) algorithm to optimize the design parameters of FSS-loaded patch antennas. The proposed method proved to be highly effective, achieving a significant improvement in antenna performance. The optimized patch antenna with FSS showed a marked increase in gain from 4.1 dBi to 7.2 dBi at 3.6 GHz, alongside an enhancement in the S11 parameter from -18 dB to -24 dB. These improvements validate the capability of the M2LP-HBMO model to accurately capture the complex relationships between design variables and performance metrics, thereby enabling the design of highly efficient microwave components. Furthermore, a comparison with existing designs in the literature highlighted that the proposed antenna design, with its compact size of 60x60x12 mm and use of a cost-effective FR4 substrate,

provides a competitive balance between size, performance, and cost. This makes the approach particularly suitable for high-frequency applications where space constraints and material costs are critical considerations.

Overall, the study establishes that advanced AI techniques, when combined with sophisticated optimization algorithms, can serve as powerful tools for optimizing complex electromagnetic structures. This approach offers a promising alternative to traditional electromagnetic simulation software, providing a more efficient pathway to achieving superior performance in FSS and patch antenna designs. The results of this research pave the way for further exploration and application of AI-driven optimization in the broader field of microwave engineering.

REFERENCES

[1] Wei, Z. (2023). Machine Learning-Assisted Automated Modeling, Optimization and Design of Electromagnetic Devices.

[2] Lalbakhsh, A., Simorangkir, R. B., Bayat-Makou, N., Kishk, A. A., & Esselle, K. P. (2022). Advancements and artificial intelligence approaches in antennas for environmental sensing. *Artificial Intelligence and Data Science in Environmental Sensing*, 19-38.

[3] P. Mahouti,"Design optimization of a pattern reconfigurable microstrip antenna using differential evolution and 3D EM simulation-based neural network model," Int. J. RF Microw. Comput.-Aided Eng., vol. 29, no. 8, April 2019.

[4] M. J. Asher, B. F. W. Croke, A. J. Jakeman, and L. J. M. Peeters, "A review of surrogate models and their application to groundwater modeling," Water Resources Research, no. 8, pp.5957-5973,2015.

[5] S. Koziel, "Low-cost data-driven surrogate modeling of antenna structures by constrained sampling," IEEE Antennas and Wireless Propagation Letters, pp. 461-464, 2016.

[6] Mishra, B., Singh, A. K., Satheesha, T. Y., Verma, R. K., & Singh, V. (2024). From Past to Present: A Comprehensive Review of Antenna Technology in Modern Wireless Communication. Journal of Engineering Science & Technology Review, 17(3).

[7] Vapnik V., "The Nature of statistical learning theory," Springer-Verlag, New York, 1995.

[8] Arthur, C. K., Temeng, V. A., Ziggah, Y. Y.,"Novel approach to predicting blast-induced ground vibration using Gaussian process regression," Engineering with Computers, 36(1),pp.29-42,2020.

[9] Maulik, U., & Chakraborty, D. (2017). Remote Sensing Image Classification: A survey of support-vector-machine-based advanced techniques. *IEEE Geoscience and Remote Sensing Magazine*, *5*(1), 33-52.

[10] Nalepa, J., & Kawulok, M. (2019). Selecting training sets for support vector machines: a review. *Artificial Intelligence Review*, *52*(2), 857-900.

[11] Mahmoodzadeh, A., Mohammadi, M., Ibrahim, H. H., Rashid, T. A., Aldalwie, A. H. M., Ali, H. F. H., & Daraei, A. (2021). Tunnel geomechanical parameters prediction using Gaussian process regression. *Machine Learning with Applications*, *3*, 100020.

[12] Zhang, C., Wei, H., Zhao, X., Liu, T., Zhang, K.." A Gaussian process regression based hybrid approach for short-term wind speed prediction," Energy conversion and management, 126, pp. 1084-1092, 2016.

[13] Gao, W., Karbasi, M., Hasanipanah, M., Zhang, X.,Guo, J. "Developing GPR model for forecasting the rock fragmentation in surface mines," Engineering with Computers, 34(2),pp. 339-345, 2018.

[14] Mienye, I. D., & Sun, Y. (2022). A survey of ensemble learning: Concepts, algorithms, applications, and prospects. *IEEE Access*, *10*, 99129-99149.

[15] Khalil Alsmadi, M., Omar, K. B., Noah, S. A., & Almarashdah, I. (2009, March). Performance comparison of multi-layer perceptron (Back Propagation, Delta Rule and Perceptron) algorithms in neural networks. In *2009 IEEE International Advance Computing Conference* (pp. 296-299). IEEE.

[16] N. Calik, M. A. Belen, P. Mahouti, "Deep learning base modified mlp model for precise scattering parameter prediction of capacitive feed antenna," International Journal of Numerical Modelling: Electronic Networks, Devices and Fields, vol. 33, no. 2, 2020.

[17] Belen, A., Günes, F., Palandoken, M., Tari, O., Belen, M. A., & Mahouti, P, "3D EM data driven surrogate based design optimization of traveling wave antennas for beam scanning in X-band: an application example", Wireless Networks, 28(4), 1827-1834, 2022.

[18] Belen, A., Tarı, Ö., Mahouti, P., Belen, M. A., & Caliskan, A.," Surrogate-based design optimization of multi-band antenna", Applied Computational Electromagnetics Society Journal, 2022.

[19] Mahouti, P., Belen, A., Tari, O., Belen, M. A., Karahan, S., & Koziel, S.,"Data-driven surrogate-assisted optimization of metamaterial-based filtenna using deep learning", Electronics, 12(7), 1584, 2023.

[20] M.A. Belen, "Performance enhancement of a microstrip patch antenna using dual-layer frequency-selective surface for ISM band applications", Microw Opt Technol Lett.

[21] Z. B. Weng, N. B. Wang, Y. C. Jiao, FS Zhang, "A directive patch antenna with metamaterial structure", Microw Opt Technol Lett.2007;49(2):456–459.

[22] S. Shalini, M. Ashok, R. T. Malay, "High gain dual band slot antenna loaded with frequency selective surface for WLAN/fixed wireless communication", Microw Opt Technol Lett., Volume 61, Issue2 February 2019 Pages 519-525, DOI:10.1002/mop.31559

[23] F. Güneş Mehmet A. Belen P. Mahouti, Performance enhancement of a microstrip patch antenna using substrate integrated waveguide frequency selective surface for ISM band applications Microw Opt Technol Lett., 60(5), pp. 1160-1164, 2018

[24] N. Muhammad, H. Umair, Z. U. Islam, Z. Khitab, I. Rashid, and F. A. Bhatti, "High Gain FSS Aperture Coupled Microstrip Patch Antenna," Progress In Electromagnetics Research C, Vol. 64, 21-31, 2016. DOI:10.2528/PIERC16022102

Chapter 8

POWER FLOW, LOSSES AND EFFICIENCY IN INDUCTION MOTORS

Mehmet Cihat ÖZGENEL[1]

1 Electric and Electronics Engineering Department, Engineering Faculty, Erzincan Binali Yıldırım University, mcozgenel@erzincan.edu.tr, ORCID: 0000-0001-5304-1488

1.1 EQUIVALENT CIRCUIT IN INDUCTION MOTORS

Induction motors are very similar to transformers, especially the wound rotor asynchronous motor. The induction motor stator corresponds to the primary winding in the step-down transformer, and the rotor is similar to the secondary winding in the transformer as it seen illustrated in Fig. 1. The basis of transferring electrical power to the secondary winding in a transformer and to the rotor in an asynchronous motor are the same. The transfer of power in both machines is done according to Faraday's electromagnetic induction principle. Since electrical power is occurred on the rotor by induction principle in asynchronous motors, these motors are also called induction motors.

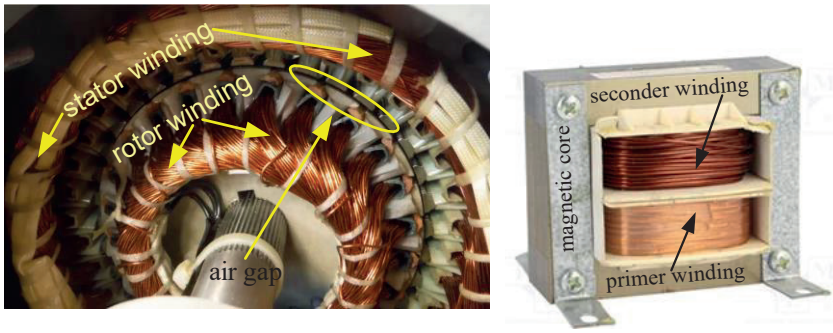

Fig. 1. Similarity of induction motor and transformer.

Although transformer and induction motor are similar in terms of operation, there are the following differences between the two in a transformer does not move. In an asynchronous motor, there is a very thin air gap between the stator and the rotor so that the rotor can rotate within the stator. Therefore, more magneto motor force is needed for the magnetic flux in order to cross through the air gap compared to the same power transformer. Because the air gap reluctance is much higher (low permeability) than the ferromagnetic core. Therefore, while the current that creates the magnetic field in induction motors is between 25 and 40 percent of the rated current, in transformers this current is between 2 and 5 percent of the primary rated current. The primary voltage frequency is equal voltage frequency developed in the secondary winding in the transformers. But in the induction motor, only when the slip is 1, the rotor voltage frequency is equal the stator voltage frequency. When the rotor starts to rotate, the rotor voltage inducted in the rotor winding and

frequency of rotor voltage decrease. As the rotor revelation up, the rotor windings voltage and its frequency decrease.

While secondary winding voltage depends on the secondary winding number of turns in the transformer, the induced voltage in the induction motor's rotor depends on the rotor winding turns and the rotor rotation speed (Eqbal, 2012).

As with all electrical machines, using the equivalent circuit in the examination of the induction motor analyzes simpler and more understandable. For the analysis of multi-phase alternating current electrical machines, one phase electrical equivalent circuit of the motor is used. To draw the induction motor electrical equivalent circuit, it need to be written the motor parameters on the equivalent circuit, starting from the energy input to the motor.

To draw asynchronous motor equivalent circuit, let's start by assuming that the motor is unloaded. When the induction motor is energized, current flows through the stator windings. This current encounters the resistance (R_1) and inductance (JX_1) of the stator winding. Since the induction motor is unloaded, the stator winding current is called the no-load (I_0) current. A part of this no-load current creates a rotating field in the stator magnetic circuit, which is called the magnetizing current (I_m). The other component of the no-load current is used for the heat generated by the change of magnetic domains direction in the stator magnetic core (I_c). The magnetizing current lags the voltage applied to the stator by 90 degrees. An electrical element that draws this current must put into the equivalent circuit. Reactance (X_m) is suitable for this because the reactance current is lateness the voltage by 90 degrees. Similarly, an element representing the current that creates heat in the core must be added to the equivalent circuit. Resistance (R_c) is suitable for this because the current and voltage in the resistor are in the same phase and the resistor converts the current into heat. The vectorial sum of the currents drawn by these two passive elements (R_c and X_m) is the no-load current and this current does not change according to the load condition of the motor. Therefore, these passive elements must be added in parallel in the equivalent circuit (Mashar and Mudawari, 2020).

When electric power is inputted to asynchronous motor three-phase winding of the stator creates a rotating magnetic field. The stator

rotating magnetic field cuts the rotor conductors and rotor bars and voltage is induced in the rotor windings. This voltage is the highest value when the rotor not move. As soon as the rotor starts rotating, this voltage created in the rotor windings begins to decrease. This voltage created in the rotor winding passes current through the rotor conductors. When a current passes through the rotor windings or rotor bars, a magnetic field is created on the rotor surface and the rotor begins to rotate by following the stator rotating field. As it is in the stator windings, the rotor winding has a resistive (R_2) and a reactive (X_2) components.

Accordingly, an asynchronous motor equivalent circuit operating without load can be drawn as in Fig. 2. In Fig. 2, N_1 and N_2 are the stator and rotor windings turns numbers respectively. E_2 is the induced voltage in the rotor one phase winding electromotive force (emf).

In Fig. 2, the voltage V_1 applied to the stator phase winding of the unloaded induction motor passes the unloaded operating current I_1 through the winding. However, since the no-load operating current is small, the voltage drops in the stator winding are neglected and this current is considered as the no-load current ($I_1=I_0$).

The unloaded current I_0 passes through the parallel R_c and X_m elements and separates into I_c and I_m components. The I_m current is the magnetizing current and creates the stator rotating field, the I_c current is compensates for the heat losses (iron losses) in the stator ferromagnetic core.

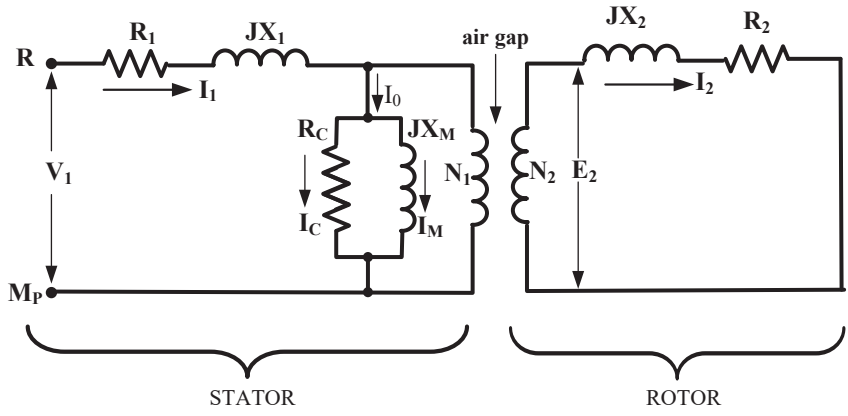

Fig. 2. Induction motor equivalent circuit running at no load.

The R_c element in Fig. 2 represents the heat losses (iron losses) occurring in the stator ferromagnetic core. The power consumed on this element is the iron losses. Since the R_c and JX_m elements are connected in parallel with the V_1 source voltage, the currents drawn by these elements are constant and do not vary with respect to motor load condition. These elements is not physically exist on the motor. However, they are symbolized with the currents they draw. When an induction motor is operating without load, the current it draws also includes the current to compensate for windage and friction losses. However, these currents are often neglected because they are small. Considering the equivalent circuit, induction motor iron losses can be calculated the power consumed by the R_c element and is found with the expression (1).

$$P_{fe} = 3 * I_c^2 * R_c \tag{1}$$

To further simplify the motor equivalent circuit in Fig. 2, the rotor section and the stator section are combined. However, when this combination is made, the rotor parameters are not directly combined with the stator. As it is in transformers, the transformation ratio of the stator and rotor phase windings is used when transferring the rotor parameters to the stator. The conversion ratio is found with the expression (2).

$$a = \frac{N_S}{N_R} \tag{2}$$

Here N_S is the stator winding number and N_R is the rotor winding number. Transferring other rotor parameters to the stator is as well as in transformers.

$$R_2' = a^2 * R_2 \tag{3}$$

$$X_r' = a^2 * X_r \tag{4}$$

$$I_r' = \frac{I_r}{a} \tag{5}$$

$$E_1 = a * E_2 \tag{6}$$

To transfer the rotor resistance and reactance to the stator side, they are multiplied by the square of the transformation ratio (expressions (3 and 4)). To transfer the rotor current to the stator side, the rotor current is divided by the square of the transformation ratio (expression (5)). In order to transfer the electromotive force

occurring in the rotor to the stator side, the rotor electromotive force is multiplied by the square of the transformation ratio (expression (6)).

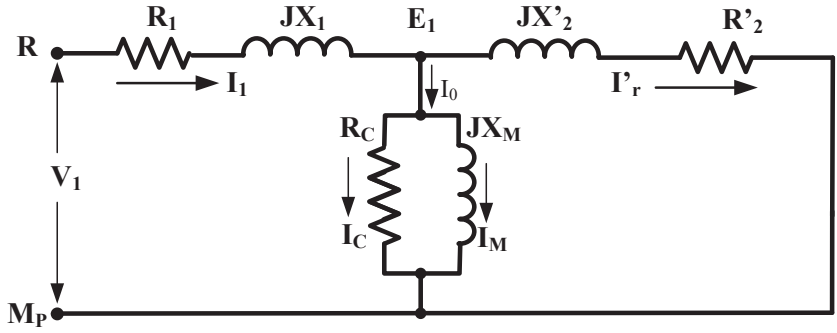

Fig. 3. Induction motor equivalent circuit with rotor parameters transferred to the stator side.

In Fig. 3, the equivalent circuit transferred to the stator side using the transformation ratio of the rotor parameters is given. However, there is no element in this equivalent circuit that represents the power produced by the motor. If an element representing the power generated by the motor *(R_L)* is added to the circuit in Fig. 3, then the motor equivalent circuit will be completed.

Since the induction motor produces active mechanical power, it should be added a passive circuit element to the equivalent circuit that represents this power and consumes active power, this element is the resistance.

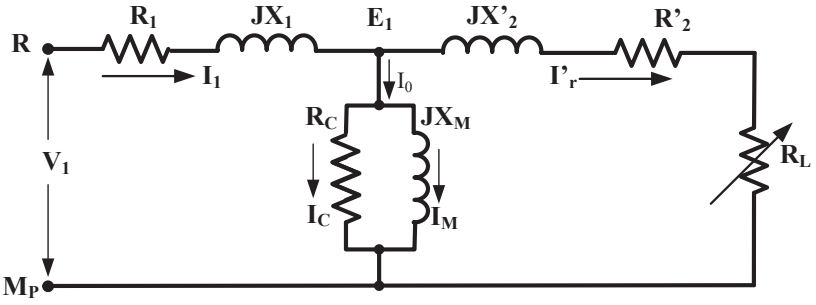

Fig. 4. Induction motor equivalent circuit.

Here, the R_L element added to the equivalent circuit represents the power developed by the motor and its value is found with the following expression (Mashar and Mudawari, 2020).

$$R_L = R_2' * \frac{(1-s)}{s} \quad (7)$$

Here R_2' is the rotor resistance transferred to the stator side and s is the slip. Since the equivalent circuit in Fig. 4 resembles the letter "T", this equivalent circuit is also called the T equivalent circuit.

1.2 POWER FLOW INDUCTION MOTORS

While electric machines convert energy, a small amount of the power given to the machine's input turns into heat in the windings, ferromagnetic core of machine and bearings. Since this heat occurs in different parts of the machine, this heat is called losses. This heat also damages the insulation of the machine and deteriorates it over time. Since the heating of the machine decreases life span and efficiency of the machine, some precautions are put into application to prevent heat damaging the induction motor, for example, adding a cooling fan to the motor shaft.

1.2.1 Stator Losses

In induction motors, losses occur in the form of core losses, copper losses, and wind and friction losses as heat. This heat generated is supplied by the electrical energy given to the induction motor and causes the entire power given to the motor not to be converted into mechanical power. Thus, the efficiency of the motor decreases.

- **Stator core (iron) losses**

These losses occur in the ferromagnetic core of the motor. Core losses are also called iron losses. Iron losses appear as heat in the ferromagnetic core. Iron losses consist of two losses. One of them is **hysteresis** and the other is **eddy** current losses (Electrical Volt, (n.d.), Sarhan, 2011).

The induction motor rotor and stator are actually electromagnets. An electromagnet is made by winding a coil around a ferromagnetic core. Ferromagnetic core of an electromagnet has very small domains called magnets that have a net magnetic field. However, as it seen in Fig. 5, these domains cancel each other's magnetic fields and the

ferromagnetic core does not create a magnetic field provided that the electromagnet coil is not inputted voltage.

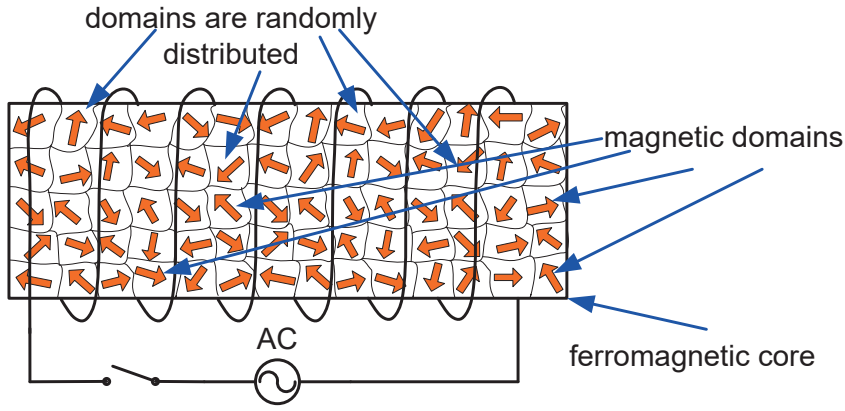

Fig. 5. The state of the domains in the ferromagnetic core with non-energized coil.

When the electromagnet coil is energized, created the magnetic field by the coil aligns the domains in the core and causes the ferromagnetic core to emit a magnetic flux. In Fig. 6(a), the positive half-cycle is given to the electromagnet coil and the current passing through the coil direction is upward. Passing current through the coil occurs a magnetic field inside winding. The created magnetic field by the coil aligns the randomly distributed domains within the magnetic core and produces a net magnetic field, with the left side of the ferromagnetic core being the *N* pole and the right side being the *S* pole.

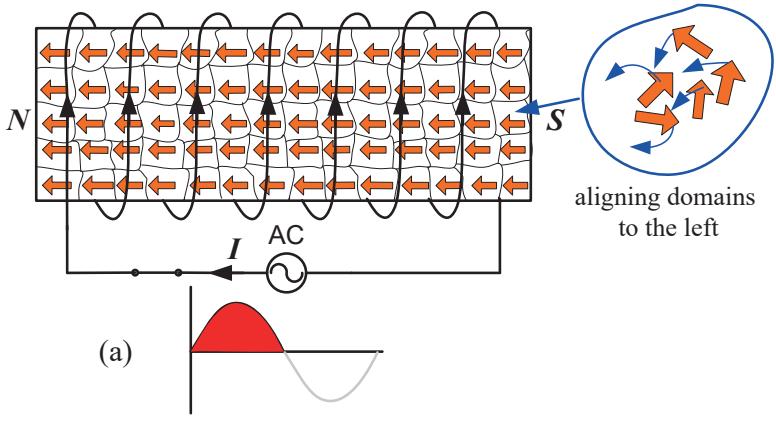

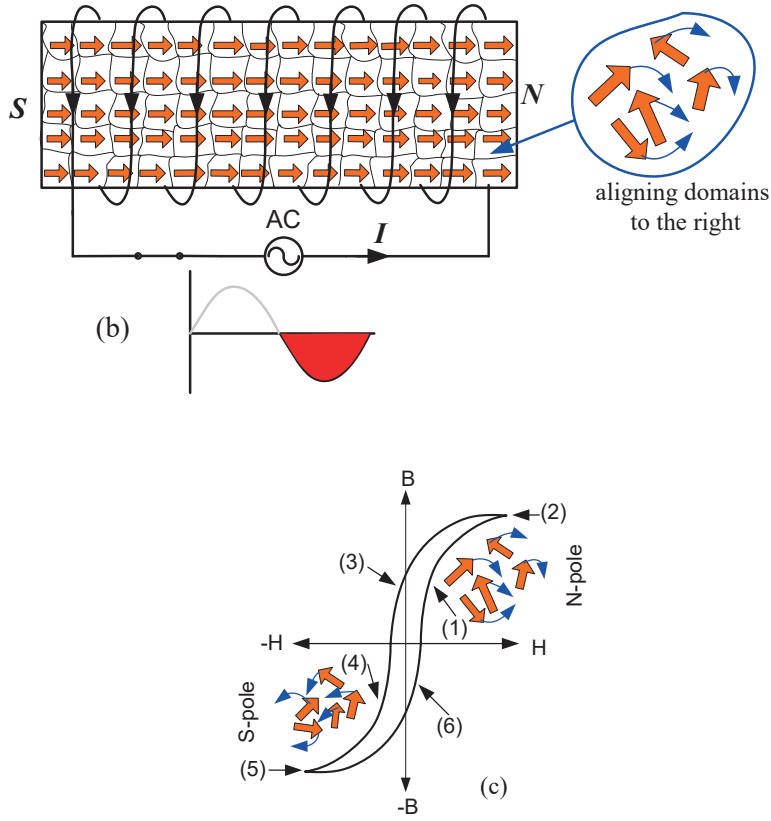

Fig. 6. Changing the direction of the domains according to alternate current passing through coil (a, b) and hysteresis loop (c).

In Fig. 6(b), the direction of the coil current has changed downwards. Because the negative half period of current is given to the coil. When the current direction is reversed, the magnetic field direction occurring inside the coil has also reversed. When magnetic field direction occurring inside the coil changes, the direction of the domains within the core also changes and the domains are aligned to the right in the reverse direction compared to the previous situation with the left side of the ferromagnetic core being the *S* pole and the right side being the *N* pole.

After the negative half period of the alternating current, the positive half period will be applied to the coil again and coil current direction will change. When the current direction changes, the magnetic domains will be aligned again as in Fig. 6(a). When the positive half-cycle is end, the negative half-cycle will be applied to the coil, the

current direction will change, therefore the magnetic domains will reverse compared to the previous situation and thus the direction of the domains will constantly change as the direction of the alternating current changes. During Changing in the directions of the domains in the magnetic core depending on the current frequency, the domains rub against each other. As a result of this friction, some heat occurs in the magnetic core. This heat generated in the magnetic core is actually fed from the electrical source. Thus, this heat generated in the core is a loss. This loss is called **hysteresis** loss. Fig. 6(c) shows the hysteresis loop created by the alternating current passing through the phase winding of the motor in one period. As the alternating current increases, the domains in the magnetic core align more and the magnetic core's flux density increases (1). During this alignment period, the domains rub against each other and create heat. The alternating current reaches its maximum value and the magnetic core produces the highest magnetic field density (2). Then the alternating current starts to decrease (3) and some domains in the magnetic core become free and the magnetic core's flux density decreases.

When the negative period of the alternating current starts, this time the domains rotate in the opposite direction. During this rotation, the domains rub against each other and heat is generated. When the alternating current starts to increase in the reverse direction, the domains rotate in the opposite direction and rub against each other (4). When the alternating current reaches it's the highest value in the reverse direction, the aligned domains also reach a maximum (5) and then when the alternating current starts to decrease from its negative maximum value, some of the domains disperse again (6). When the alternating current reaches zero from its negative value, it has completed a period. Thus, a hysteresis cycle is completed. Hysteresis loop occurs in every period of the alternating current and during this hysteresis cycle, the movement of the domains causes creep and this friction generates heat. As it illustrated in Fig. 6(c), if the frequency increases, the hysteresis cycle becomes faster and more heat is generated, which means that iron losses increase (Fitzgerald et al, 1990).

In induction motors fed from the mains, the iron losses occurring in the stator ferromagnetic core are constant. Because the mains frequency is constant. Iron losses do not vary according to the load motor load condition. In the motor equivalent circuit, the R_c resistance

represents the iron losses Since the R_c resistor is connected in parallel in the equivalent circuit, it draws constant current. In order to find the iron losses, the motor is tested for no-load operation.

Hysteresis losses are found with the following expression (8).

$$P_h = K_h * B_m^n * f * V \qquad (W) \tag{8}$$

Here, K_h is the Steinmetz coefficient that varies between 1.5 and 2.5 and depends on the structure of the magnetic material in (J/m^3), B_m is the maximum value of magnetic flux in Tesla $(^{Wb}/_{m^2})$, n is the Steinmetz exponent value that varies between 1.5 and 2.5 depending on the magnetic properties of the material, f is the alternating current frequency, in Hz and V is the magnetic core volume in m^3.

Another loss occurring in the ferromagnetic core is the eddy current loss. When making electromagnetic systems, if the magnetic core is made as a single block, it creates circulating currents within the core, known as eddy currents, as it seen in Fig. 7(a). When the core is thick, the alternating current passing through the coil creates eddy currents in the mono block material. These eddy currents cause the magnetic core to heat up and the useful magnetic flux to decrease. To prevent occurring eddy currents, thin laminated silicon steel sheets are used to reduce eddy currents.

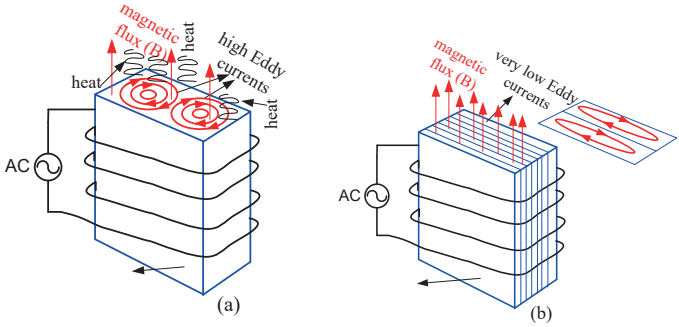

Fig. 7. Eddy currents (a), using laminated core to reduce Eddy losses (b).

The surfaces of these sheets are isolated from each other so that the eddy current does not pass to the neighboring steel sheet. As it seen in Fig. 7(b), the magnetic circuit is made of thin sheet metal packages,

which creates very high resistance for eddy currents. The thickness of silicon steel sheets can vary between 0.20 mm and 5 mm.

Heat generated by eddy currents in the magnetic core is supplied by the current given to the coil of the magnetic system. Therefore, a portion of the electric current is turned into heat in the magnetic core. Therefore, this heat is called eddy losses. Eddy losses are expressed with the following equation (9) (Electrical Volt, n.d.).

$$P_e = K_e * B_m^2 * f^2 * t^2 * V \quad (W) \tag{9}$$

Here, K_e is the eddy current constant coefficient depends on the magnetic material characteristic, t is the thickness of the thin sheet metal in meter. K_e is found with the following expression (10).

$$K_e = \frac{\pi^2}{6*\rho} \tag{10}$$

Here, ρ is the resistivity of the magnetic material in Ω*meter. If the K_e value in equation (10) is substituted into equation (9), the expression for eddy losses can be written as follows (11) (Electrical Volt, n.d.).

$$P_e = \frac{1.645}{\rho} * B_m^2 * f^2 * t^2 * V \quad (W) \tag{11}$$

In the equivalent circuit in Fig. 4, R_c resistance represents the iron losses. The power consumed by this resistance is the iron losses ($P_h + P_e$) and it is found with the expression (1) given in the previous section.

- **Stator copper losses**

The induction motor stator phase windings have a resistive resistance. When phase voltage is given to the phase winding, current passes through the phase winding. At the initial start-up, this current is 5 to 8 times the normal load current. This current also decreases until the rotor reaches its normal speed. As it is known, the current flow through a conductor occurs by moving electrons along the conductor. As electrons pass through the conductor, they rub against each other, during this friction, an amount heat is occurred along the wire. When phase voltage is given the phase windings, the phase current creates some heat in the windings. Thus, as long as current flows through the phase windings, the windings continue to heat up. The electrical power that creates this heat in the phase windings is drawn from the source and some of the electrical power is turned into

heat in the phase windings. This heat generated in the phase windings is called **stator** copper **losses** since the phase windings are made of copper conductors, and is expressed by the following mathematical equation.

$$P_{1cu} = 3 * I_1^2 * R_1 \quad (W) \tag{12}$$

Here P_{1cu} is the stator copper losses in W, I_1 is the stator phase current in $Amp.$, R_1 is the alternate current resistance of the stator phase winding in ohms.

Copper losses are not constant like iron losses and vary with respect to the current drawn by the motor. The motor current changes with respect to the mechanical load.

Up to this point, we have understood that there are two types of losses in the asynchronous motor stator. As it seen in Fig. 8, one of these losses is the iron losses that occur in heat form in the magnetic core, and the other one is the copper losses that occur in the heat form in the phase windings.

As it seen in Fig. 8, when we subtract the iron and copper losses occurring in the stator from the power given to the stator, we find the power in the stator and rotor air gap (P_{ag}). The power in the air gap is also the electrical power transferred from the stator to the rotor.

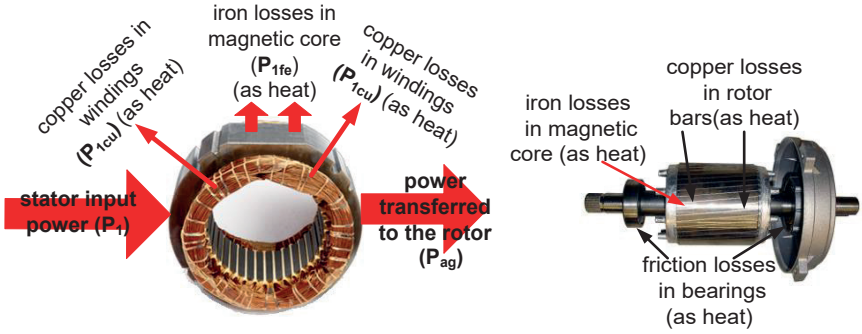

Fig. 8. Losses in asynchronous motor stator and rotor.

1.2.2 Rotor Losses

Asynchronous motors have two main parts: stator and rotor. In the previous section, the stator losses were examined. In this section, the rotor losses will be examined. The rotor structure of asynchronous motors has two types, one of which is the squirrel cage

rotor and the other one is the slip ring wound rotor. The losses occurring in the rotor are iron, copper, wind and friction losses. How iron and copper losses occur were explained in detail in the previous section. Therefore, in this section, the examination will be made by taking the rotor into consideration without focusing too much on how iron and copper losses occur.

- **Rotor core (iron) losses**

We have seen that when the rotor of induction motor starts to rotate, the voltage and frequency of the voltage in the rotor windings will decrease. When the motor reaches its nominal speed, the rotor voltage frequency will be a small value such as 2~6 *Hz*. Since the rotor voltage frequency is very low, the magnetic domains friction each other in the rotor magnetic core becomes very slow and the iron losses are very low and can negligible. Therefore, rotor iron losses are often neglected.

- **Rotor copper losses**

When the asynchronous motor is energized, the highest current passes through the rotor conductors before the rotor has even started rotating. As mentioned earlier section, current passing through a conductor produces heat as a result of the friction of electrons. Since the initial phase current is high at the first working moment, the heat generated in the conductor is high. When the rotor starts to rotate, the voltage inducted in the rotor decreases, so the rotor current decreases and therefore the heat generated in the conductors also decreases. When the rotor reaches its normal speed, the rotor current also decreases to its normal value.

This heat generated in the rotor conductors is drawn from the voltage source applied to the motor and this heat is called rotor copper loss. Rotor copper losses vary depending on the motor load and are expressed by the following equation.

$$P_{rcu} = 3 * I_2^2 * R_2 \qquad (W) \tag{13}$$

Here P_{rcu} is the rotor copper losses in W, $I_2$is the rotor phase current in $Amp.$, and R_2 is the alternate current resistance of the rotor phase winding or rotor bar in ohms.

- **Rotor mechanic (rotational) losses**

Rotor mechanical losses occur in the rotor bearings, in the friction of the fan and the rotor blades with the air. To overcome mechanical losses the motor draws a small amount of power from the source and this power is called windage and friction or rotational losses. In asynchronous motors with slip ring wound rotors, in addition to the friction occurring in the bearings and the fan, friction losses occur in the brushes and slip rings. In order to reduce friction and windage losses in asynchronous motors, high-quality with very low friction bearings and very low friction with the air cooling fans are used. (Electrical Volt, n.d.). Friction and windage losses in induction motors vary between approximately 5 percent and 15 percent of the total losses, with respect to the selection of the cooling fan and bearings (Fatima, 2021).

1.3 EFFICIENCY in INDUCTION MOTORS

To determine the induction motor efficiency as a power converter, the losses must first be known. In the previous section, the losses that occur when a motor converts power were explained in detail. The electrical power given to a three-phase induction motor is

$$P_1 = 3 * V_1 * cos\varphi_1 \quad \text{or} \quad P_1 = \sqrt{3} * V_{l-l} * I_1 * cos\varphi_1 \tag{14}$$

Here V_1 is the phase voltage, V_{l-l} is the phase-to-phase voltage, I_1 is the stator phase current. During power conversion, iron losses occur in the stator magnetic core and copper losses occur in the phase windings. Copper losses occurring in phase windings were given by equation (12) in the previous section. Hysteresis and eddy current losses establish as the iron losses in the stator magnetic core. If we subtract the stator iron and copper losses from the power given to the stator 3 phase winding, we find the electrical power transferred from the stator to the rotor. This power is also the air gap the power between the stator and the rotor. The power in the air gap (P_{ag}) is found with the expression (15).

$$P_{ag} = P_1 - ((P_h + P_e) + P_{1cu}) = P_1 - (P_{1fe} + P_{1cu}) \tag{15}$$

P_{1fe} is stator iron loss and P_{1cu} is the stator winding copper loss.

When the rotating field occurring in the air gap cuts the rotor conductors, voltage is induced in the rotor conductors. Thus, current

flows through the rotor conductors the current passing through the rotor windings or rotor bars creates copper losses. At the same time, iron losses occur in the rotor magnetic core. However, since the rotor speed in a squirrel cage asynchronous motor is close to the rotating field speed, the voltage and frequency occurring in the rotor are very low. Thus, the iron losses occurring in the rotor are also very small and are generally neglected. However, in wound rotors asynchronous motors, since the rotor speed is varied by the resistances connected to the rotor circuit, the rotor voltage and frequency will increase at speeds far from the rotating field speed, thus iron losses cannot be neglected. The powers mentioned so far are electrical powers. When we subtract the rotor iron and copper losses from the air gap power (P_{ag}), the power value obtained is the gross mechanical power produced by the motor. When we subtract the rotary mechanical losses from the gross power produced by the motor, we find the power taken from the motor shaft as it seen in Fig. 9 (Sen, 1997).

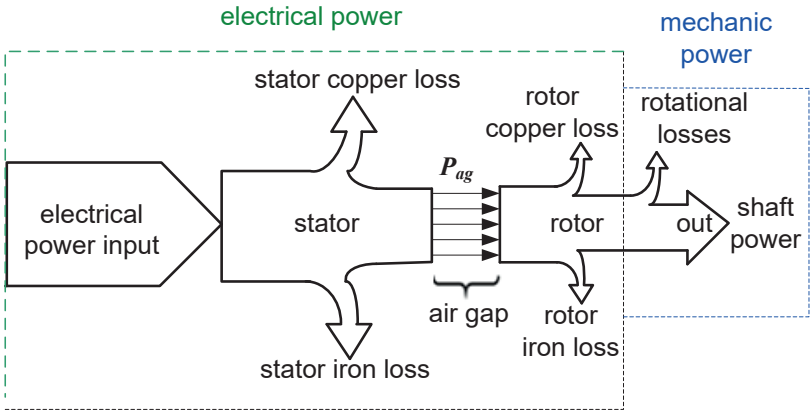

Fig. 9. Power flow and losses in an asynchronous motor.

Fig. 9 illustrates the electrical power input, losses, and power flow into an induction motor.

The air gap power (P_{ag}) is found by dividing the rotor copper losses by the slip.

$$P_{ag} = 3 * (I_r')^2 * \frac{R_2'}{s} = \frac{P_{rcu}}{s} \tag{15}$$

The power produced (P_{dev}) by the asynchronous motor is expressed by the equation (16).

$$P_{dev} = P_{ag} * (1 - s) \quad (16)$$

The gross power produced by an asynchronous motor includes the rotational losses of the motor. The motor shaft power is found by subtracting the wind and friction losses from the gross power produced by the motor.

$$P_{out} = P_{dev} - (P_{wind} + P_{fric}) \quad (17)$$

The efficiency of an induction motor is expressed by dividing the motor shaft power by the electrical power supplied to the motor. (Mashar and Mudawari, 2020).

$$\eta = \frac{P_{out}}{P_1} * 100 \quad (18)$$

The torque received from the motor shaft is found with the equation (19) below.

$$T_{out} = \frac{9.55 * P_{out}}{n_r} \qquad (Nm) \quad (19)$$

Here n_r is the rotor speed in rpm.

The gross torque is:

$$T_{dev} = \frac{9.55 * P_{dev}}{n_s} \qquad (Nm) \quad (20)$$

Here n_s is the stator rotating field speed in *rpm* (synchronous speed).

Example 1

A three-phase 460 V, 50 *Hz*, 4-pole, wye-connected asynchronous motor operates with 4% slip. The motor parameters taking the stator as reference, are R_1=0.20 Ω, $X_1 = 0.40\ \Omega$, $R_2' = 0.15\ \Omega, X_2' = 0.60\ \Omega, X_m = 40\ \Omega, R_c = 80\ \Omega$. Wind and friction losses are 1800 W. Find the followings; a-) air gap power, b-) gross power, c-) motor gross efficiency, d-) rotor cooper losses, e-) motor efficiency.

Solution

a-) to find the air gap power to determine the air gap power, the power input to the motor and the stator copper and iron losses must be calculated.

$$R_L = R_2' * \frac{(1-s)}{s} = 0{,}15 * \frac{(1-0.04)}{0.04} = 3.6\ \Omega$$

$$V_1 = \frac{V_{L-L}}{\sqrt{3}} = \frac{460}{\sqrt{3}} = 265.5\ V$$

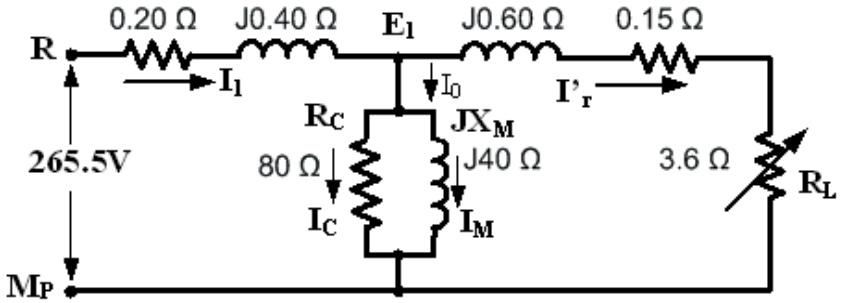

Fig. 10. Motor full equivalent circuit.

The motor phase current according to the full equivalent circuit:

$$Z_{tot} = (R_1 + JX_1) * [\frac{(R_2' + R_L + JX_2') * (R_c + JX_m)}{(R_2' + R_L + JX_2') + (R_c + JX_m)}]$$

$$Z_{tot} = (0.20 + J0.40) * \left[\frac{(0.15+3.6+J0.60)*(80+J40)}{(0.15+3.6+J0.60)+(80+J40)}\right] = 3.8+\text{J1}\ \Omega$$

$$I_1 = \frac{V_1}{Z_{tot}} = \frac{265.5}{3.8 + J1} = 65.34 - J17.2\ A = 67.56\angle - 14.74^0\ A$$

$$\varphi_1 = -14.74^{\ 0}\ and\ cos\varphi_1 = 0.967$$

Power input to the motor:

$$P_1 = \sqrt{3} * V_{l-l} * I_1 * cos\varphi_1 = \sqrt{3} * 460 * 67.56 * 0.967 = 52051.65\ W$$

To find the air gap power, it is necessary to subtract the stator iron and copper losses from the power given to the motor.

$$P_{ag} = P_1 - (P_{1cu} + P_{1fe})$$

Stator copper losses:

$$P_{1cu} = 3 * I_1^2 * R_1 = 3 * (67.56)^2 * 0.20 = 2738.6\ W$$

According to the equivalent circuit E_1 is:

$$E_1 = V_1 - I_1 * (R_1 + JX_1)$$
$$= 265.5\angle 0 - [65.34 - J17.2 * (0.20 + J0.40)]$$

$$E_1 = 265.5 - 19.94 + J22.69 = 245.56 - J22.69 = 246.6\angle - 5.28^0\ V$$

$$I_c = \frac{E_1}{R_c} = \frac{246.6\angle - 5.28^0}{80\angle 0} = 3\angle - 5.28^0\ A$$

Stator iron losses:

$$P_{1fe} = 3 * I_c^2 . R_c = 3 * 3^2 * 80 = 2160\ W$$

The current creating the stator rotating magnetic field (I_M):

$$I_M = \frac{E_1}{JX_M} = \frac{246.6\angle - 5.28^0}{40\angle 90} = -0.56 - J6.13 = 6.15\angle 84.78^0\ A$$

The power in the air gap:

$$P_{ag} = P_1 - (P_{1cu} + P_{1fe})$$

$P_{ag} = 52051.65 - (2738.6 + 2160) = 47153\ W$ This power is delivered to the rotor.

b-) the gross power (P_{dev}) produced by the asynchronous motor also includes windage and friction losses.

$P_{dev} = P_{ag} * (1 - s) = 47153 - (1 - 0.04) = 45266.88\ W.$

c-) the gross efficiency:

$$\eta_{gross} = \frac{P_{dev}}{P_1} * 100 = \frac{45266.88}{52051.65} * 100 = 87\%$$

d-) Equation (15) is used to find the rotor copper losses.

$$P_{ag} = = \frac{P_{rcu}}{s}$$

$P_{rcu} = P_{ag} * s = 47153 * 0.04 = 1886.12W$

Rotor copper losses can also be found by subtracting the developed power in the rotor from the power delivered to the rotor.

$P_{rcu} = P_{ag} - P_{dev} = 47153 - 45266.88 = 1886.12\ W$

The mechanical power (P_{dev}) produced by the motor is also found by subtracting the rotor copper losses (P_{rcu}) from the air gap power (P_{ag}).

$P_{dev} = P_{ag} - P_{rcu} = 47153 - 1886.12 = 45266.88\ W$

e-) Power received from motor shaft:

$$P_{out} = P_{dev} - (P_{wind} + P_{fric}) = 45266.88 - 1800 \\ = 43466.88\ W$$

And motor net efficiency:

$$\eta = \frac{P_{out}}{P_1} * 100 = \frac{43466.88}{52051.65} * 100 = 83\%$$

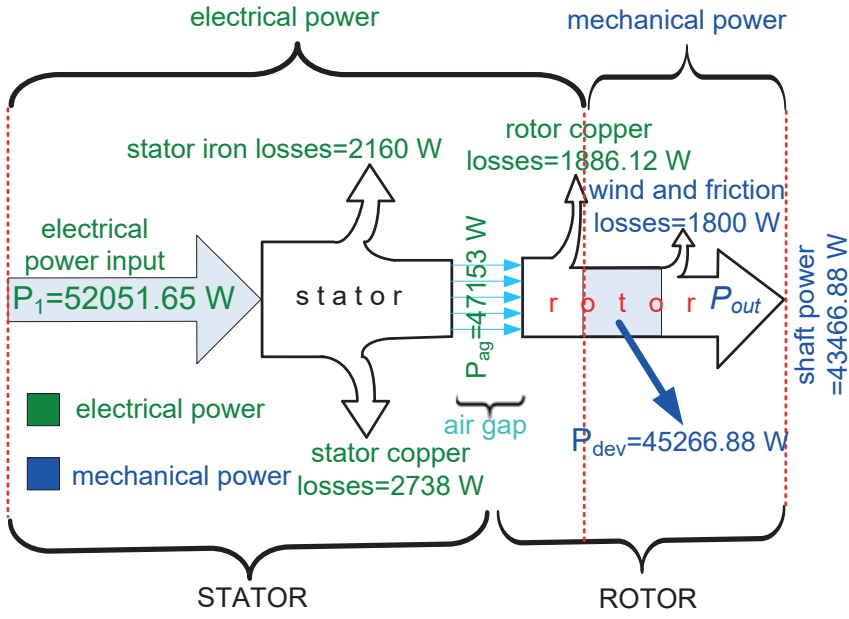

Fig. 11. Power flow diagram of the motor in Example 1.

Example 2

A three-phase 410 V, 50 Hz, 4-pole, star-connected asynchronous motor operates at 1440 rpm. The motor parameters are R_1=0.25 Ω, $X_1 = 0.50\ \Omega$, $R_2' = 0.20\ \Omega$, $X_2' = 0.60\ \Omega$, $X_m = 60\ \Omega$, $R_c = 100\ \Omega$. Wind and friction losses are 2000 W. Find the followings using the approximate L equivalent circuit in Fig. 12; a-) slip, b-) phase current, c-) power factor, d-) air gap power, e-) rotor current, f-) motor efficiency.

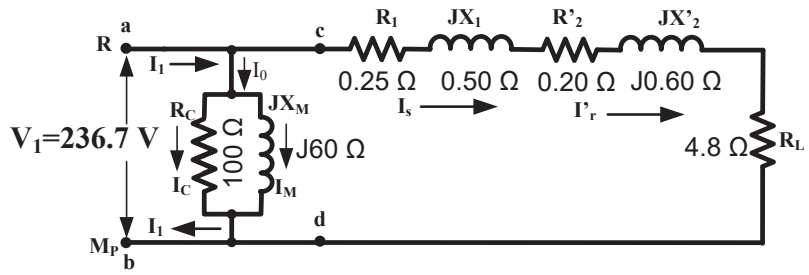

Fig. 12. Motor L equivalent circuit.

Solution

a-) $n_s = \frac{120*f}{P} = \frac{120*50}{4} = 1500\ rpm$

$s = \frac{n_s - n_r}{n_s} = \frac{1500-1440}{1500} = 0.04$

b-) $R_y = R_2' * \left(\frac{1-s}{s}\right) = 0.20 * (\frac{1-0.04}{0.04}) = 4.8\ \Omega$

$Z_{cd} = (R_1 + R_2' + R_L) + J(X_1 + X_2') = (0.25 + 0.20 + 4.8) + J(0.50 + 0.60) = 5.25 + J1.10\ \Omega = 5.36\angle 11.83^0\ \Omega$

$V_1 = \frac{V_{l-l}}{\sqrt{3}} = \frac{410}{\sqrt{3}} = 236.7\ \text{V}$

$I_s = \frac{V_1}{Z_{cd}} = \frac{236.7\angle 0^0}{5.36\angle 11.83^0} = 43.22 - J9 = 44.14\angle -11.76^0$

$I_c = \frac{V_1}{R_c} = \frac{236.7\angle 0^0}{100\angle 0^0} = 2.36\angle 0^0\ \text{A}$

$I_M = \frac{V_1}{JX_m} = \frac{236.7\angle 0^0}{60\angle 90^0} = 3.93\angle -90^0\ \text{A}$

$I_1 = I_s + I_C + I_M = 44.14 - J9 + 2.36 - J3.93 = 46.5 - J12.93 = 48.26\angle -15{,}53^0\ \text{A}$

c-) Power factor:

$cos\varphi_1 = 0{,}96$

d-) air gap power:

$P_1 = \sqrt{3} * V_{l-l} * I_1 * cos\varphi_1 = \sqrt{3} * 410 * 48.26 * 0.96 = 32900.54\ \text{W}$

$P_{1fe} = 3 * I_c^2 * R_c = 3 * 2.36^2 * 100 = 1670.88\ W$

$$P_{1cu} = 3 * I_1^2 * R_1 = 3 * 44.14^2 * 0.25 = 1461.25\ W$$

$$P_{ag} = P_1 - (P_{1cu} + P_{1fe})$$

$$P_{ag} = 32900.54 - (1461.25 + 1670.88) = 29768.41\ W$$

e-) the rotor current according to the approximate equivalent circuit is:

$$I_s = I_r' = \frac{V_1}{Z_{cd}} = \frac{236.7\angle 0^0}{5.36\angle 11.83^0} = 43.22 - J9 = 44.14\angle -11.76^0\ \text{A}$$

f-) motor efficiency:

In the equivalent circuit, the R_L resistance represents generating power by the motor. If we subtract the windage and friction losses from this power, the motor shaft power (P_{out}) is found.

$$P_{dev} = 3 * (I_r')^2 * R_L = 3 * 44.14^2 * 4.8 = 28056\ W$$

$$P_{out} = P_{dev} - \left(P_{wind} + P_{fric}\right) = 28056 - 2000 = 26056\ W$$

$$\eta = \frac{P_{out}}{P_1} * 100 = \frac{26056}{32900.54} * 100 = 79\%$$

REFERANCES

Electrical Volt, (n.d.) Losses in induction motors, Retrieved 2024 July 26 from https:// www.electricalvolt.com/losses-in-induction -motor.

Eqbal, A. (2012, Aug, 01). *Basics of 3-phase Induction Motor (part 1)*, Electrical Engineering Portal, https://electrical-engineering-portal.com/basics-of-3-phase-induction-motor-1.

Fatima, B. (2021), *Design optimization and development of energy efficient induction motor for industrial applications,* International Journal of Advanced Research, Ideas and Innovations in Technology, Volume 7, Issue 6 - V7I6-1371, p-p:336-341.

Fitzgerald, A. E., C. Kingsley, Jr., and S. D. Umans. (1990) Electric Machinery, 5th ed. New York: McGraw-Hill, 1990.

Mashar, A., Mudawari A. (2020), *Determination of Three-Phase Induction Motor Equivalent Circuit Parameters Experimentally,* International Seminar of Science and Applied Technology (ISSAT 2020), Advances in Engineering Research, volume 198, p-p:209-214.

Sarhan, H. (2011, *May) Energy Efficient Control of Three-Phase Induction Motor Drive,* Energy and Power Engineering, Vol. 3 No. 2, 2011, pp. 107-112. doi: 10.4236/epe.2011.32014.

Sen, P. C. (1997) Principles of Electric Machines and Power Electronics, Second Edition, John Wiley & Sons, 1997.

Chapter 9

COMBUSTION PERFORMANCE IN NATURAL GAS STRATIFIED CHARGE ENGINES

Müjdat FIRAT[1]
Ömer Faruk AKÇİL[2]
Cengiz ÖNER[3]

1 Doç. Dr., Fırat Üniversitesi, Teknoloji Fakültesi, Otomotiv Mühendisliği Bölümü, Elazığ, Türkiye
2 Ömer Faruk AKÇİL, Fırat Üniversitesi, Teknoloji Fakültesi, Otomotiv Mühendisliği Bölümü, Elazığ, Türkiye, omerfarukakcil@gmail.com
3 Prof.Dr. Cengiz ÖNER, Bingöl Universitesi Mühendislik-Mimarlık Fakültesi Makine Mühendisliği, Bingöl,Türkiye (ORCID: 0000-0002-3278-2831), coner@bingol.edu.tr

1 Introduction

Recently, a lot of research has been done on fuels and mixture formation, as well as the charge system structure, to increase engine performance. These systems are structurally divided as; homogeneous charge and stratified charged homogeneous charge, the aim is to mix the fuel with air in the intake manifold and spread it evenly into the cylinder. Stratified charge aims to obtain a stoichiometric mixture in the spark plug region of the cylinder as it moves away from the spark plug, and a lean mixture in the other parts. In this way, Stratified charge engines can be operated with lean mixture, just like diesel engines. A decrease in nitrogen oxide, carbon dioxide and unburned hydrocarbon emission values was observed in the gradual filling method applied in gasoline engines (Jubin et al., 2022).

Due to environmental pollution and energy crisis, many researchers are working on efficient and clean alternative fuels (such as natural gas, LPG and H_2) to replace traditional fossil fuels such as gasoline and diesel (Yang et al. 2023).

Methane, the main component of natural gas, has a low laminar flame speed, resulting in incomplete combustion and high unburned hydrocarbon emissions. Therefore, there is increasing interest in increasing the flame spread speed of natural gas SI engines while at the same time mitigating the knocking tendency under stoichiometric combustion conditions (Chen et al. 2021).

In the literature, in addition to mixture formation systems in gasoline engines, the use of alternative fuels has also taken its place in research topics. The most common of these are alternative fuels such as LPG, CNG and biogasoline. When the studies are examined;

Can (2009) made a gasoline engine run on LPG, and by making the necessary modifications to the engine cylinder head, valve and valve seats, and the mixture ramp, the mixture was taken into the cylinder

through two channels. In this way, the spark plug region was able to obtain stoichiometric and other region lean mixtures He stated that there was no significant change in the power and torque values of the engine in operation with homogeneous and stratified charge, specific fuel consumption decreased by up to 20% in operation with stratified charge, and the effective efficiency increased by 15% at high engine speeds.

In their study, Mehdiyev et al. (2004) developed a two-stage combustion mechanism in a stratified charge gasoline engineAccording to their results, the double-loop combustion mechanism increased the engine performance and efficiency and significantly reduced exhaust emissions.

Zhao et al. (1999) in their study, examined automotive ignition systems and studied stratified chargeIn their study, they modified the intake valve of a four-stroke, four-cylinder engine and managed to get the mixture into the cylinder in two different ways. Thus, a visible decrease in fuel consumption was achieved, and it was also observed that the tendency to knock decreased when operating with low-octane gasoline.

Kurtlar et al. (2000), in their study, examined lean-mixture stratified charge engines to reduce fuel consumption at partial loads in gasoline engines. They stated that there was a 35% improvement in fuel consumption in Mitshubishi's stratified charge engine, which was made by injecting fuel directly into the combustion chamber, and that fuel consumption would decrease by 5-13% with the use of multi-valve stratified charge engines.

Zeng et al. (2015) experimentally investigated the in-cylinder flow and spray interactions in a stratified charge direct injection spark ignition engine. In the experimental study, a single-cylinder four-stroke optical engine was used and high-resolution imaging was achieved with the particle velocity imaging technique. It has been observed that directing the flow into the cylinder correctly increases the kinetic energy, thus accelerating the combustion and completing it more appropriately. In

cases where the fuel is not directed correctly, low flow energy and injection interaction are observed, especially at the beginning of combustion.

Costa et al. (2016) experimentally and numerically examined the combustion performance and emission formation in a stratified charge direct injection gasoline engine. In the experimental study, experimental data were taken from the cylinder using an optical engine and high imaging techniques. As a result of the study, the combustion process and heat release were compared with experimental and numerical findings, and it was shown that the time of the second injection was effective on combustion efficiency and emission formations

Choi et al. (2016) modeled the fuel injection and combustion process in a direct injection engine using CNG. A single-cylinder four-stroke gasoline engine was used in the research. In the study where different injection pressure and different injection timing were examined, it was observed that the injection pressure did not significantly affect the average effective pressure, but the injection timing significantly affected it. It has also been observed that injection timing affects the homogeneity of the mixture, cylinder pressure and partly fuel consumption.

Aljamali et al. [10] examined the effect of injection timing on engine performance and emissions in a stratified charged engine. In the experimental study, they used CNG as fuel. Four different injection timings (120 CA, 180 CA, 300 CA, 360 CA BTDC) were used in the study, where the end of the injection was taken as reference. Experimental results are presented in graphs, including torque, specific fuel consumption, average effective pressure, CO, CO2, NO and HC. In the study, the highest power, torque, average effective pressure and lowest specific fuel consumption were obtained at 120 CA injection timing. In addition, the lowest NO and HC emissions were obtained at 120 CA injection timing, while CO2 emissions increased depending on the number of cycles.

In an engine using CNG as fuel, the effects of direct injection of CNG and port injection on volumetric efficiency and combustion

characteristics were investigated by Song et al. (2017). In the study, four different injection timings (120 CA, 210 CA, 270 CA and 330 CA BTDC) were studied. According to the results obtained in the research, it was seen that direct and port injection did not affect the volumetric efficiency in case of early fuel injection.. In addition, the best torque values were obtained due to increased volumetric efficiency and combustion speed in late injection timings.

Sankesh et al. (2017) investigated the direct injection situation and the timing of this injection, considering the problem of decreasing volumetric efficiency and torque when natural gas is injected from the port. A single-cylinder, four-stroke gasoline engine was used in the study and natural gas was chosen as the fuel. While different injection pressures were used in the study, injection timing was examined in two parts: early and late. It has been emphasized that late injection timing increases volumetric efficiency.

Liu and Dumitrescu (2018) examined the use of natural gas in a spark ignition engine experimentally and numerically. The study was carried out at different ignition times, different equivalence ratios and different engine speeds. In the study, five different gas compositions with different gas percentages were used as fuel. At the end of the research, it was seen that low methane rates increased the pressure.

2. Material and methods

The aim of the study is to numerically investigate the use of natural gas in a strafied charged gasoline engine. Within the scope of the study, startified charge conditions were achieved in a direct injection gasoline engine with two injections made at different times. In the numerical study, it was aimed to analyze engine performance and pollutant emission formations.

The aim of the study is to analyze the 3D numerical analysis of natural gas usage in a stratified charged gasoline engine. Çalışma

kapsamında kademeli dolgulu benzinli bir motorda doğalgaz kullanımının 3 boyutlu sayısal analizi amaçlanmıştır. In the study, firstly, the design of the relevant engine model was carried out This design was created as a symmetry model, including the intake manifold, exhaust manifold, cylinder head, injector, spark plug and combustion chamber. A network structure was created using the drawing model with the number of 302543 elements.

2.1. Governing Equations

In internal combustion engines, the air-fuel mixture before combustion and the end products after combustion are considered the working fluid. Analyzing these fluids and solving the related combustion problem depends on some sub-equations and models. ANSYS Forte uses the Navier-Stokes equations to provide basic fluid dynamics solutions. In addition, it uses Fick's laws for mass diffusion. It uses Fourier's laws for heat dissipation. Some of the governing equations used to perform the analyzes are shown below (ANSYS Forte Theory Manuel).

Conservation equations;

$$\frac{\partial \bar{\rho}_k}{\partial t} + \nabla.(\bar{\rho}_k \tilde{u}) = \nabla.[\overline{\rho} D \nabla \bar{y}_k] + \nabla + \phi \ (k = 1, \dots, K) \ , \tag{2.1}$$

Among the source terms resulting from the use of Fick's law expressed in the equation, ρ refers to density, k refers to the species index, and K refers to the total number of species.

Continuity equation;

$$\frac{\partial \bar{\rho}_k}{\partial t} + \nabla.(\bar{\rho}\tilde{u}) = \dot{\bar{\rho}}^S \tag{2.2}$$

Momentum conservation equation;

$$\frac{\partial \bar{\rho}\tilde{u}}{\partial t} + \nabla.(\bar{\rho}\tilde{u}\tilde{u}) = -\nabla.\bar{\rho} + \nabla.\bar{\sigma} - \frac{2}{3}\bar{\rho}\tilde{k}I + \bar{F}^S + \overline{\rho g} \ , \tag{2.3}$$

The $\bar{\sigma}$ viscous stress tensor expressed in the equation is calculated with equation (2.4).

$$\bar{\sigma} = \bar{\rho}v\left[\nabla\tilde{u} + (\nabla\tilde{u})^T - \frac{2}{3}(\nabla.\tilde{u})I\right] \quad \textbf{(2.4)}$$

Energy conservation equation;

$$\frac{\partial\bar{\rho}\tilde{I}}{\partial t} + \nabla.(\bar{\rho}\tilde{u}\tilde{I}) = -\bar{\rho}\nabla.\tilde{U} - \nabla.\bar{J} - \nabla.H + \bar{\rho}\tilde{\varepsilon} + \dot{\bar{Q}}^C + \dot{\bar{Q}}^S \quad \textbf{(2.5)}$$

According to the energy conservation equation, $\dot{\bar{Q}}^C$ denotes heat dissipation, $\dot{\bar{Q}}^S$ denotes spray interaction, I denotes specific internal energy, and J denotes heat flux. The heat flow resulting from heat conduction and enthalpy diffusion is calculated by equation (2.6).

$$\bar{J} = -\lambda\nabla\tilde{T} - \bar{\rho}D_T\sum_k \tilde{h}_k\nabla\left(\frac{\bar{\rho}_k}{\bar{\rho}}\right), \quad \textbf{(2.6)}$$

In the equation, λ corresponds to the heat conduction coefficient, T corresponds to the flow temperature, and $\tilde{h}_k$ corresponds to the specific enthalpy expressions of the species.

Gas mixture equation of state;

$$\bar{p} = R_U\tilde{T}\sum_k\left(\frac{\bar{\rho}_k}{W_k}\right) \quad \textbf{(2.7)}$$

The gas mixture equation of state for gas phase mixtures is derived by adhering to the ideal gas law. In the equation, R_U is defined as the universal gas constant, while W_k is the expression of the molecular weight of the species.

2.1 Turbulence Model

Examining in-cylinder air flow and air-fuel interaction in internal combustion engines is a very important turbulent flow problem. In order to solve the problem correctly, the turbulence models to be used and the selection of the turbulence model appropriate to the problem are important.

In this study, the RNG k-epsilon turbulence model, which is also available in ANSYS Forte, was used to model turbulent flow (ANSYS Forte Theory Manuel). This model was preferred because it gives more accurate results in the analysis of internal combustion engines. Considering that the RNG k-epsilon model takes into account smaller-scale movements than the standard k-epsilon model, it is expected to provide more sensitive results. The necessary equations for the RNG k-epsilon model are given below.

$$\Gamma = -\bar{\rho} v_t \left[\nabla \tilde{u} + \left(\nabla \tilde{U}\right)^T - \frac{2}{3}(\nabla . \tilde{u}) I\right] + \frac{2}{3}\bar{\rho}\tilde{k} I \tag{2.8}$$

$$\tilde{k} = \frac{1}{2\bar{\rho}} trace(\Gamma) = \frac{1}{2}\widetilde{u'' u''} \tag{2.9}$$

$$v_T = C_\mu \frac{\tilde{k}^2}{\tilde{\varepsilon}}, \tag{2.10}$$

$$\phi = \bar{\rho} D_T \nabla \bar{y}_k \tag{2.11}$$

$$H = -\lambda_T \nabla \bar{T} - \bar{\rho} D_T \sum_k \tilde{h}_k \nabla \bar{y}_k \tag{2.12}$$

$$D_T = \frac{v_T}{Sc_T} \tag{2.13}$$

$$\alpha_T = \frac{v_T}{Pr_T} \tag{2.14}$$

The k and ε equations for the RNG model are given in 2.15 and 2.16.

$$\frac{\partial \bar{\rho}\tilde{k}}{\partial t} + \nabla.\left(\bar{\rho}\tilde{u}\tilde{k}\right) = -\frac{2}{3}\bar{\rho}\tilde{k}\nabla.\tilde{u} + (\bar{\sigma} - \Gamma):\nabla\tilde{u} + \nabla.\left[\frac{\mu + \mu_T}{Pr_k}\nabla\tilde{k}\right] - \bar{\rho}\tilde{\varepsilon} + \dot{\bar{W}}^S, \tag{2.15}$$

$$\frac{\partial \bar{\rho}\tilde{\varepsilon}}{\partial t} + \nabla.\left(\bar{\rho}\tilde{u}\tilde{\varepsilon}\right) = -\left(\frac{2}{3}C_{\varepsilon 1} - C_{\varepsilon 3}\right)\bar{\rho}\tilde{\varepsilon}\nabla.\tilde{u} + \nabla.\left[\frac{(v + v_T)}{Pr_\varepsilon}\nabla\tilde{\varepsilon}\right]$$

$$+\frac{\tilde{\varepsilon}}{\tilde{k}}\left[C_{\varepsilon 1}(\sigma - \Gamma):\nabla\tilde{u} - C_{\varepsilon 2}\bar{\rho}\tilde{\varepsilon} + C_S\dot{\bar{W}}^S\right] - \overline{\rho R} \tag{2.16}$$

Pr_k, Pr_ε, $C_{\varepsilon 1}$, $C_{\varepsilon 2}$ and $C_{\varepsilon 3}$ in the equation are model constants. R in the last term can be defined as follows.

$$R = \frac{C_\mu(\eta)^3(1 - \eta/\eta_0)}{1 + (\beta\eta^3)}\frac{\tilde{\varepsilon}^2}{\tilde{k}}\ , \tag{2.17}$$

$$\eta = S\frac{\tilde{k}}{\tilde{\varepsilon}}\ , \tag{2.18}$$

$$S = (2\bar{S}:\bar{S})^{1/2} \tag{2.19}$$

$$\bar{S} = \frac{1}{2}(\nabla\tilde{u} + \nabla\tilde{u}^T). \tag{2.20}$$

The constants used in the above equations are determined as follows for the RNG k-epsilon model (ANSYS Forte Theory Manuel).

	C_μ	$C_{\varepsilon 1}$	$C_{\varepsilon 2}$	$C_{\varepsilon 3}$	$1/Pr_k$	$1/Pr_\varepsilon$	η_0	β
RNG k-ε	0.0845	1.42	1.68	1.44	1.39	1.39	4.38	0.012

2.2. Chemical Kinetic Formulation

In internal combustion engine simulations, chemical reactions must be solved correctly for the analysis and complete solution of the combustion phenomenon. Chemical reactions are described as chemical kinetic mechanisms. To realize this recipe, the chemical properties,

thermophysical properties and thermodynamic properties of the fuel are needed. By combining the data obtained with the chemical kinetic mechanism, reaction rates that create changes in the concentrations of the relevant species are defined. In chemical kinetic mechanisms, chemical species in reactions are calculated by the following equations.

$$\sum_{k=1}^{K} v'_{ki} X_k \Leftrightarrow \sum_{k=1}^{K} v''_{ki} X_k (i = 1, \dots, I). \tag{2.21}$$

production rateof k. species in i. reaction ;

$$\dot{\omega}_{ki} = (v''_{ki} - v'_{ki}) q_i (k = 1, \dots, K) \tag{2.22}$$

According to the production rate of all reactions, the chemical source term in the species persistence equation is obtained.

$$\dot{\rho}_k^C = W_k \sum_{i=1}^{I} \dot{\omega}_{ki} \tag{2.23}$$

In addition, the chemical heat release equation in the energy equation is obtained as follows.

$$\dot{Q}_c = \sum_{k=1}^{I} Q_i q_i = \sum_{i=1}^{I} \sum_{k=1}^{K} (v''_{ki} - v'_{ki}) \left(\Delta h_f^0\right)_k q_i \,, \tag{2.24}$$

$$Q_i = \sum_{k=1}^{K} (v''_{ki} - v'_{ki}) \left(\Delta h_f^0\right)_k \,, \tag{2.25}$$

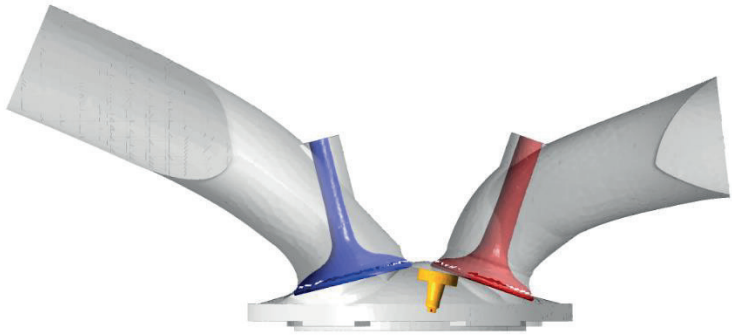

Fig. 2.1. Front view of the model

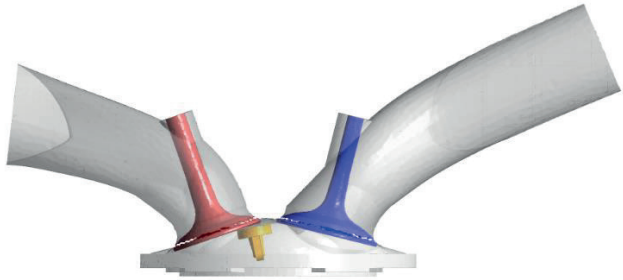

Fig. 2.2. Rear view of the model

Fig. 2.3. Bottom view of the model

In line with the literature, CH_4 was accepted for the natural gas to be used in the study. In this way, other components were neglected for numerical

studies. The thermophysical and thermodynamic properties of CH_4 used in the study are given in Table 2.1.

Table 2.1. Thermophysical and thermodynamic properties of CH_4	
Density	0,668 kg/m3 (20 °C, 1 atm)
Research Octane Number	120
Motor Octane Number	101
Boiling Point	111.5 K
Lower Calorific Value	50.009 MJ/kg
Molecular Mass	16.042 g/mol

The natural gas mechanism in the ANSYS Forte base was selected to ensure correct combustion in the creation of operating parameters. After this mechanism was determined, source files were created for the fuel used. These source files contain chemical, thermophysical, thermodynamic and transport data of the fuel. In case of working with this data and chemical kinetic mechanism, the most accurate combustion solution was tried to be obtained. In order for the study to be carried out correctly, injection conditions are p The type of injector used allows the definition of the injection pressure and different injection parameters (number of nozzles, spray angle, cone angle, etc.). The injection parameters used are given in Table 2.3.articularly important.

The type of injector used allows the definition of the injection pressure and different injection parameters (number of nozzles, spray angle, cone angle, etc.). The injection parameters used are given in Table 2.2.

Table 2.3. Technical conditions for CH_4 injection	
Injection Pressure	0.3Mpa
Injection Time	50KA
Injector Type	Hollow

Nozzle Diameter	120micron
Number of Nozzles	1
Injected Gas	CH_4

After determining all sub-models and boundary conditions, a study was started for a lean mixture homogeneous filled case where CH_4 was used as fuel under the determined engine conditions. This working condition with direct injection where a single spray is applied has been accepted as the reference study for the stratified charge conditions. Then, fuel injection was divided into two different injection timings to ensure the stratified charge conditions. In this case, a portion of the fuel was injected into the cylinder in the first injection and the air-fuel mixture was provided. Then, in the second injection, fuel was sent to the spark plug area again and a partially rich mixture was provided, especially in the spark plug area. With this applied method, the stratified charge conditions were provided and a study was carried out in the spark plug region, which was rich but generally in the lean mixture region.

In this case, the studies were repeated by injecting fuel at different rates for the first and second injections. The fuel rates and operating parameters used for this stage are shown in Table 2.3.

Table 2.3 Operating Parameters for Different Fuel Ratios

Fuel ratio	**First injection**		**Second injection**	
	CA TDC	CA	CA TDC	CA
%85-%15	300	40	120	10
%70-%30	300	35	120	15
%50-%50	300	25	120	25
%30-%70	300	15	120	35

The first injection is made towards the end of the intake stroke, 300 CA before TDC. An attempt was made to determine the ideal angle of the second spray. For this purpose, engine performance and emission formations were examined by making second injections at 220 CA (SC1), 170 CA (SC2), 120 CA (SC3) and 70 CA (SC4) before TDC. The results obtained were compared with the single spraying homogeneous charge (HC) lean mixture operating condition.

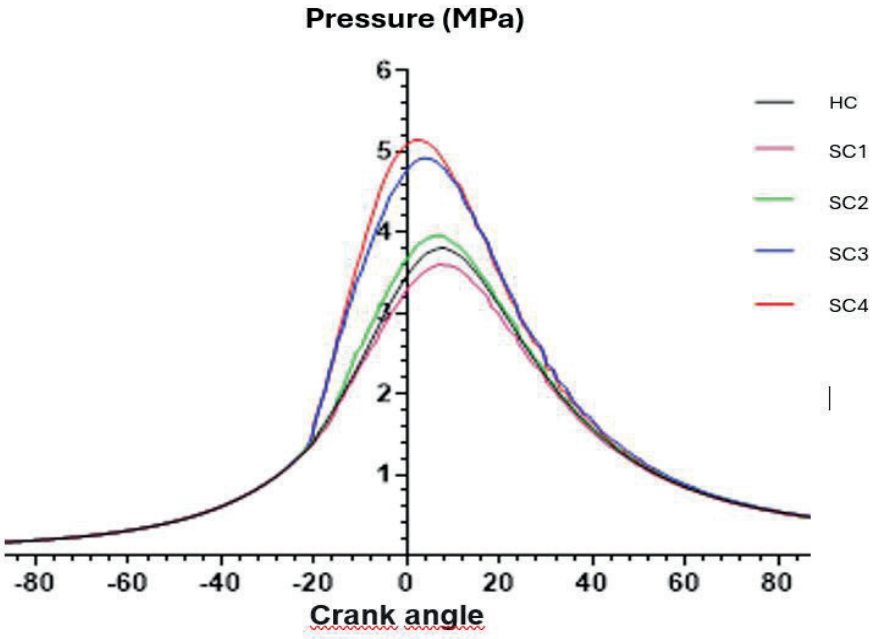

Fig. 2.4. Change in in-cylinder pres süre depending on different injection timings.

Figure 2.4 shows the in-cylinder pressure changes depending on different injection timing. As seen in the figure, in-cylinder pressure reached higher values in cases where the second injection was made late (SC3 and SC4). In the early injection cases (SC1 and SC2), it is observed that the in-cylinder pressures are closer to the homogeneous charge (HC) case. For four different second-stage early injection cases, it is observed that the maximum in-cylinder pressure occurs after TDC. In the early injection conditions of SC3 and SC4, the maximum pressure occurs just after TDC,

closer to TDC than in the SC1, SC2 and homogeneous injection conditions. As a result, it is observed that the maximum in-cylinder pressure occurs at slightly more advanced crank angles under early injection conditions. It can be said that in late injection cases, stratified charge conditions are provided more appropriately and engine performance increases. The results obtained show that the second injection timing is highly effective on the in-cylinder pressure values.

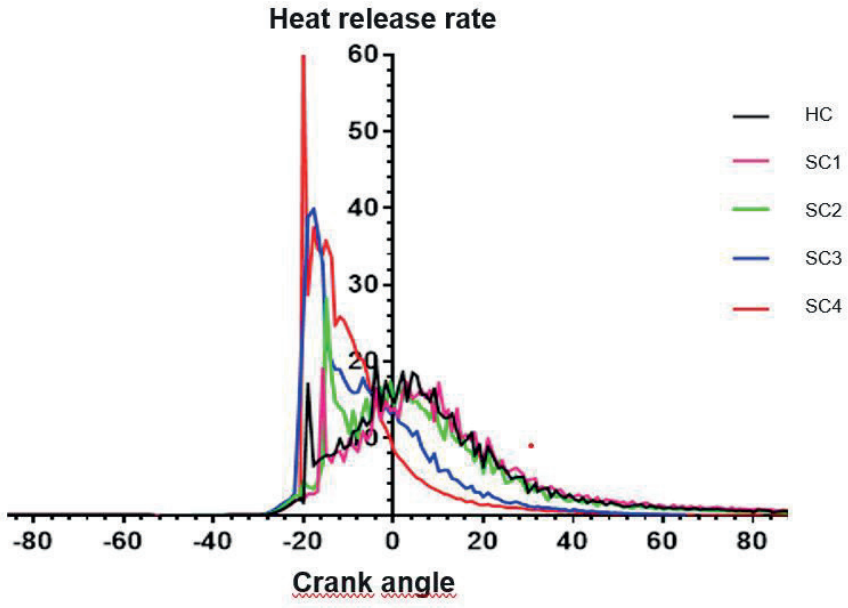

Fig. 2.5. Change in heat release rate depending on different injection timings.

The change of heat release rate depending on different spraying times is shown in Fig. 2.5. The heat release rate is also a function of the in-cylinder pressure and is an important indicator of combustion quality. It is observed that in late injection cases, heat release increases rapidly after spark ignition and most of it is completed just before TDC. It is understood from the graph that the combustion period is shorter in the second stage (SC3, SC4) late injection conditions. It is thought that this situation will increase the

engine performance but will increase the knocking tendency of the engine. In the early injection timing and homogeneous charge condition, it is observed that the heat release increases relatively more slowly after the spark plug ignition and reaches maximum values near TDC.

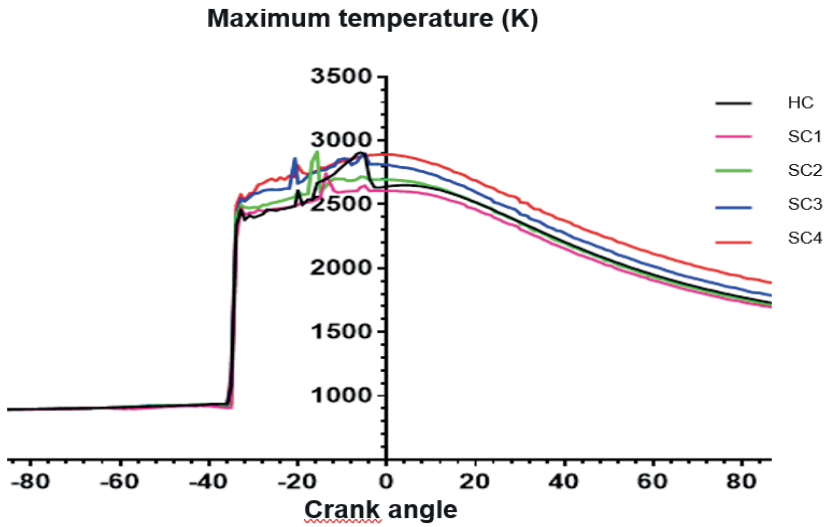

Fig. 2.6. Change in maximum in-cylinder temperature depending on different injection timings.

Figure 2.6 shows the effects of different spraying times on maximum temperatures. Combustion at similar temperatures is achieved with the combustion occurring in the cylinder due to the spark plug spark and spark plug energy. With spark ignition, in-cylinder temperatures rose rapidly for all conditions. Then the temperature curves progressed by making oscillations until TDC. This is the region where combustion begins and the flame front expands. Although similar temperature values were obtained for all injection times, slightly higher in-cylinder temperatures were obtained at late injection times. It can be said that the combustion rate is higher in the late injection (SC3, SC4) case. As a matter of fact, the heat release rate and the high temperature support this idea. Partially lower temperature values were obtained at early injection timings and in the

homogeneous charge condition. It is observed that in the early injection timings (SC1 and SC2), the maximum temperature values occur well before TDC and decrease rapidly.

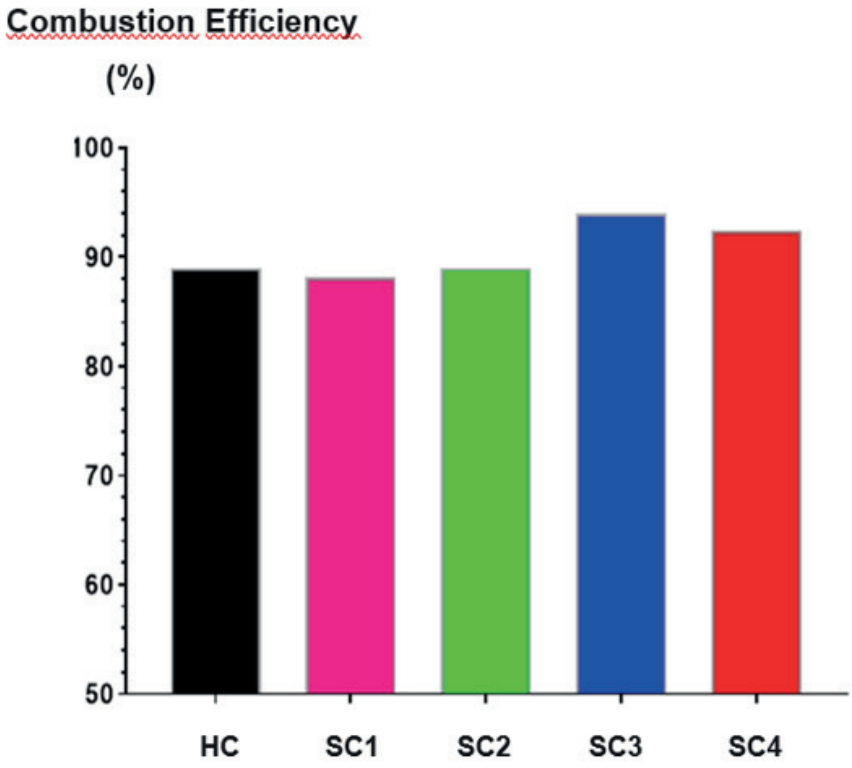

Fig. 2.7. Change in combustion efficiency depending on different injection timings.

After all the analyses performed depending on different injection timings, combustion efficiencies were calculated for the determined operating conditions (Fig. 2.7). In accordance with all the graphs obtained before, it is seen that the combustion efficiency in the SC3 case is higher than the other cases. For the HC, SC1, SC2, SC3 and SC4 Stratified Charge

conditions in which the study was carried out, combustion efficiencies of 89%, 88.2%, 89%, 93.9% and 92.4% were obtained, respectively.

References

Yang K., Wang Z., Zhang K., Wang D., Xie F., Xu Y., Yang K., 2023. Impact of natural gas injection timing on the combustion and emissions performance of a dual-direct-injection diesel/natural gas engine, Energy ,Volume 270, 126813.

Chen Z., Zhang T., Wang X., Chen H., Geng L., Zhang T., 2021**.** comparative study of combustion performance and emissions of dual-fuel engines fueled with natural gas/methanol and natural gas/ gasoline

Can, İ., 2009. LPG İle Çalışan Benzinli Bir Motora Kademeli Dolgu Yapılmasının Performans Üzerindeki Etkisinin Deneysel Olarak İncelenmesi, *Doktora Tezi*, F.Ü. Fen Bilimleri Enstitüsü, Elazığ.

Jubin V., Jose, Mayank Mittal, A. Ramesh, Gutti Gnanakotaiah, Kuduva Shanthu Vishnukumar, Shrinidhi Shridhara, 2023**,** A Novel Combustion Chamber to Physically Stratify the Charge in a Gasoline Direct Injection Engine, *SAE Int. J. Engines* 16(3):267-289.

Mehdiyev, R., Baykara, D., Arslan, H., Güdü, T., 2004. İki Aşamada Yanma Mekanizması ile Çalışan Kademeli Dolgulu Benzin Motorun Geliştirilmesi, 21-23.

Zhao F., Lai M.C. and Harrington D. L., 1999. "Automotive spark-ignited direct-injection gasoline engines",*Progress Energy of Combustion Science*, **25**, 437-562.

Kutlar, O., A., Arslan, H., Çalık, A., T., 2000. Benzin (Otto) Motorunda Kısmi Yükte Yakıt Tüketimini Azaltmaya Yönelik Bir Yöntem: Fakir Karışımlı Kademeli Dolgulu Motor, *Mühendis Makine*, **483**, 46-51.

Zeng W., Sjöberg M., Reuss D. L., 2015. Combined effects of flow/spray interactions and EGR on combustion variability for a stratified DISI engine, *Proceedings of the Combustion Institute*, **35**, Issue 3, 2907-2914.

Costa M., Sorge U., Merola S., Irimescu A., La Villetta M., Rocco V., 2016. Split injection in a homogeneous stratified gasoline direct injection engine for high combustion efficiency and low pollutants emission, *Energy*, **117**, 405-415.

Choi M., Song J., Park S., 2016. Modeling of the fuel injection and combustion process in a CNG direct injection engine, *Fuel*, **179**, 168–178.

Song J., Choi M., Park S., 2017. Comparisons of the volumetric efficiency and combustion characteristics between CNG-DI and CNG-PFI engines, *Applied Thermal Engineering*, **121**, 595–603.

Sankesh D., Edsell J., Mazlan S., Lappas P., 2017. Comparative study between early and late injection in a natural-gas fuelled spark-ignited direct-injection engine, *Energy Procedia*, **110**. 275–280.

[**Liu J., Dumitrescu C. E.,** 2018. 3D CFD simulation of a CI engine converted to SI natural gas operation using the G-equation, *Fuel,* **232**, 833–844.

ANSYS Forte Theory Manuel.

Chapter 10

STABILITY MECHANISM AND STABILITY ENHANCEMENT METHODS IN NANOFLUIDS

Fatma OFLAZ[1]

1 Dr., Fırat University, Orcid ID: 0000-0002-9636-5746

1. Introduction

The investigation of nanofluid stability is crucial in nanotechnology because the performance of nanofluids is highly dependent on how well the nanoparticles are dispersed within the base fluid. Poor nanofluid stability can have cascading negative effects on key properties such as thermal conductivity, viscosity, density, and pump efficiency (Rabby et al. 2024). These changes result in increased energy and maintenance costs, and can ultimately prevent the nanofluid from functioning as intended. If the nanoparticles settle or aggregate, it can lead to undesirable effects like clogging, which ultimately degrades properties such as thermal conductivity (Urmi et al. 2020). Scientists have observed nanofluids exhibiting stability for various timeframes, from a few hours to several months, without significant sedimentation. This shows that different factors contribute to maintaining the uniform dispersion of nanoparticles over time. Stability directly impacts nanofluid attributes like thermal efficiency, viscosity, and overall performance in practical applications (Mehta et al. 2022). To ensure the stability of nanofluids, it is essential to understand and improve key factors that influence nanoparticle dispersion. These include:

- ✓ **Particle Size and Shape**: Smaller and more uniform nanoparticles tend to remain better dispersed.
- ✓ **Surface Modifications**: Coating nanoparticles with stabilizing agents or functional groups can enhance their compatibility with the base fluid and reduce agglomeration.
- ✓ **pH Adjustment**: Altering the pH of the nanofluid can affect the electrostatic repulsion between nanoparticles, preventing clumping.
- ✓ **Use of Surfactants**: Surfactants or dispersants help in reducing the surface tension between the nanoparticles and the base fluid, improving stability.

Ultrasonication: Applying ultrasonic waves to break up agglomerates and redistribute nanoparticles evenly within the fluid (Mehta et al. 2022).

Various analysis techniques, such as zeta potential measurements (to assess the charge on nanoparticles), sedimentation observations, and light scattering methods, are used to measure and improve stability and are described in subsequent sections. These approaches help monitor the long-term homogeneity of nanofluids and are used to guide the development of more stable formulations.

2. Stability mechanisms of nanofluids

For nanofluids to be practically applied, maintaining a stable dispersion of nanoparticles over a certain period is essential. The stability of colloidal

suspensions can be described by the theory developed by Derjaguin, Landau, Verwey, and Overbeek (DLVO). This theory operates under several key assumptions: (1) the particle dispersion is considered to be dilute, (2) only Van der Waals attractive forces and electrostatic forces influence the suspended particles, (3) the effects of gravity and buoyancy are disregarded, (4) the colloidal suspension is assumed to be homogeneous, and (5) the distribution of ions within the colloidal system is governed by electrostatic forces, Brownian motion, and entropy-driven dispersion (Chakraborty and Panigrahi 2020). The DLVO theory helps explain the forces at play in this context, showing that both attractive (suction) and repulsive potential energies exist between particles suspended in a liquid. As shown in Figure 1, the DLVO theory demonstrates how changes in potential energy, based on separation distance, govern the interactions between particles. When the total interaction potential is low, particles are more likely to settle at a faster rate (Fig.1a). Conversely, when the total interaction potential is high, particles resist clumping and maintain their stability (Fig.1b). The overall system potential energy is determined by the balance between repulsive and attractive forces. When the repulsive force exceeds the gravitational force, it prevents nanoparticles from colliding, thus maintaining the stability of the nanofluid. However, when the repulsive force is too weak to counteract gravity, the nanoparticles begin to clump together, leading to aggregation and a loss of stability in the nanofluid. By modifying the balance between gravitational and repulsive forces, the stability of the nanofluid can be controlled and optimized (Wang et al. 2023).

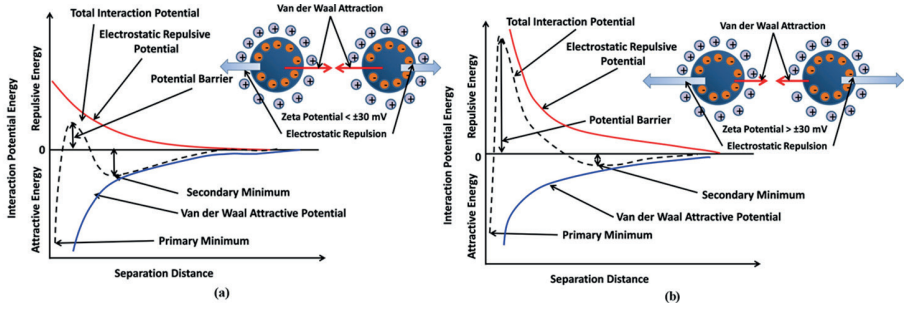

Fig.1. The variation in interaction potential energy based on the separation distance between nanoparticles in two different situations (Chakraborty and Panigrahi 2020).

3. Stability enhancement techniques

The stability of nanofluids is crucial for achieving improved thermal performance. The loss of stability in nanofluids can lead to the settling of nanoparticles. Nanoparticles typically exhibit electrostatic and van der Waals

force interactions. Instability arises from the agglomeration of nanoparticles (driven by van der Waals forces) and sedimentation (due to the density difference between the nanoparticles and the base fluid). Additionally, factors such as the nature and morphology of the nanoparticles, duration of ultrasonication, Brownian motion, interactions between particles, interactions between the particles and the base fluid, and the Soret effect (caused by temperature gradients) contribute to instability as shown in Figure 2 (Kumar et al. 2022). Furthermore, nanoparticle agglomeration can negatively affect the thermal properties of the fluid.

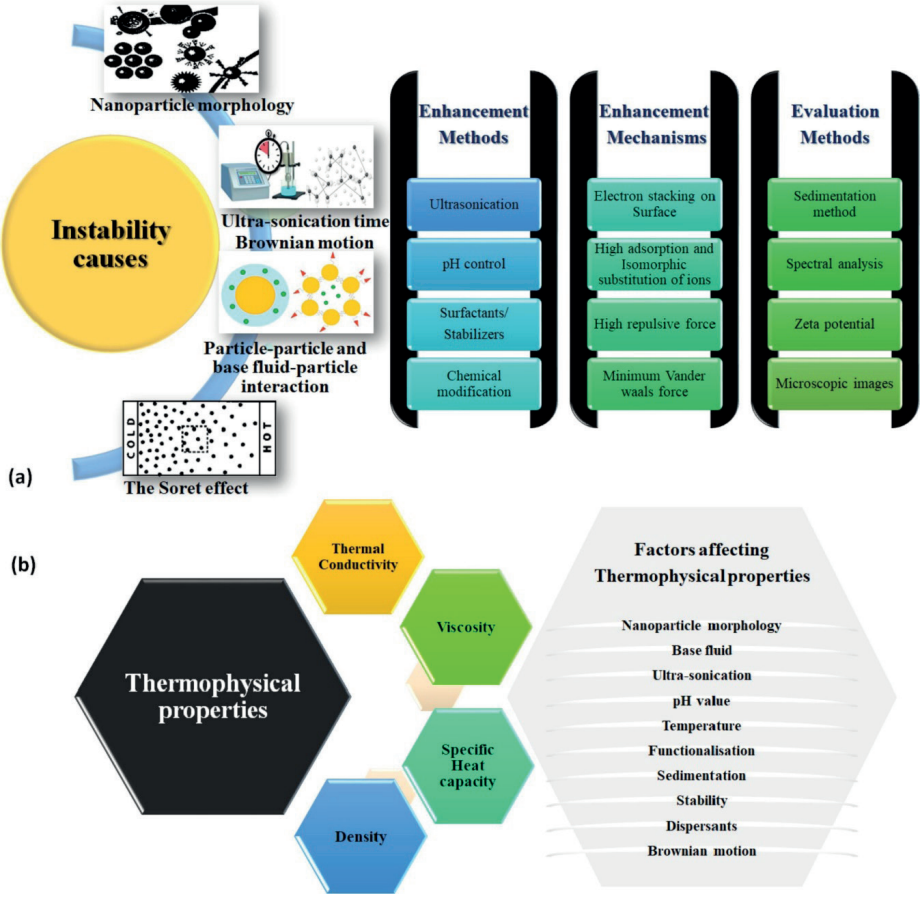

Fig.2. (a) Instability, notable enhancement, and assessment features related to nanofluid stability, (b)Factors affect the thermophysical properties of nanofluids (Kumar et al. 2022).

3.1. Ultrasonication

To improve the stability of nanofluids, breaking down the agglomeration of nanoparticles is crucial. Ultrasonicator probes or baths are commonly used

to physically disperse the nanoparticles (Urmi et al. 2020). Many researchers employ both probe and bath sonicators to achieve uniform dispersion of the nanoparticles (Ouikhalfan et al. 2020). Typically, ultrasonication is performed at varying power levels and frequencies over different time periods. The duration of sonication depends on factors such as the type, size, shape, concentration, and mixing ratio of the nanoparticles with the base fluid, as well as the preparation method (Yu and Xie 2012). Therefore, ultrasonication is a key technique that uses sound energy at different frequencies and durations to break up nanoparticle clusters in various nanofluids. Additionally, the type, size, concentration, mixing ratio, and preparation method of the nanoparticles, along with the choice of base fluid, influence the optimal sonication conditions. Figure 3 shows the methods used to increase the stability of nanofluids (Singh and Sood 2024).

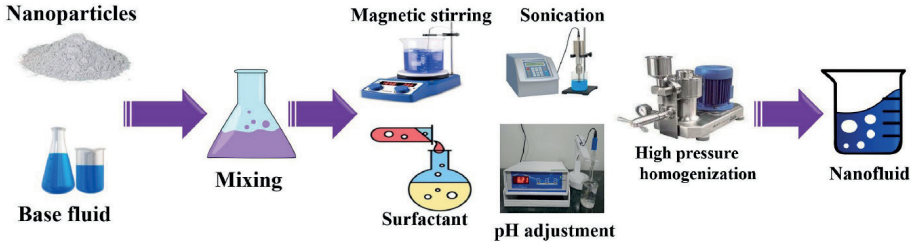

Fig.3. Methods used to increase nanofluid stability (Singh and Sood 2024).

3.2. Mechanical stirring

Mechanical stirring is a fundamental physical method for distributing nanoparticles (NPs) in a fluid. It relies on external shear forces or collision forces to ensure the NPs are evenly dispersed throughout the medium. However, when particle concentration is high, stirring stability can become problematic, potentially leading to unfavorable results. Careful control of stirring speed is essential to produce high-quality nanofluids (NFs), as excessive speed can cause bubble formation due to rapid circulation. Despite these challenges, mechanical stirring effectively disperses solid particles within the base fluid at the microscopic level, preventing immediate particle agglomeration (Wang et al. 2023).

3.3. Surfactant addition

Adding surfactants is a widely used and cost-effective approach to improving the stability of nanoparticles in a base fluid. Surfactants lower the surface tension of the fluid, which helps nanoparticles remain suspended for longer periods, preventing them from settling quickly. This increased suspension time enhances the overall stability of the nanofluids. Surfactants can be categorized into different

types based on the charge of their hydrophilic (water-attracting) head, and each type interacts with nanoparticles uniquely. During the preparation of nanofluids, three types of surfactants are commonly used to enhance nanoparticle stability; Anionic Surfactants (Sodium Dodecyl Benzene Sulfonate-SDBS), Cationic Surfactants (Cetyltrimethylammonium Bromide - CTAB), Polymeric Surfactants (Gum Arabic - GA) (Sajid and Bicer 2022).

3.4. Changing the Ph value

The pH of a nanoparticle suspension is closely linked to its zeta potential, both of which play a key role in determining the stability of nanofluids. The pH level directly impacts the surface charge density of the nanoparticles, which influences how well the particles repel each other and remain dispersed. When the pH reaches the isoelectric point (IEP), the particles have no overall net charge, and the zeta potential drops to nearly zero. At this point, the nanofluid becomes unstable because there is no repulsion between particles, leading to aggregation (Babita, Sharma, and Gupta 2016). Additionally, the pH can influence the size and shape of nanoparticles during synthesis, further affecting the long-term stability of the nanofluid. Adjusting the pH away from the IEP can help maintain a higher zeta potential, promoting a more stable dispersion of nanoparticles. In a study aimed at ensuring nanofluid stability (Kamalgharibi et al. 2016), nanofluids were prepared by adjusting different pH levels as shown in Figure 4. The pH value that resulted in the least sedimentation was identified as the most stable. Following this, ultrasonic mixing times were varied, and the optimal stability was achieved by fine-tuning this parameter. It was concluded that the highest zeta potential, which corresponds to the best stability, was obtained at a pH of 10.2, where the nanofluid displayed the most appropriate stability characteristics.

Fig.4. Effect of pH regulation on the stability of CuO/water nanofluids (Kamalgharibi et al. 2016).

4. Methods of measuring stabilitiy in nanofluids

Common methods used in the literature to assess the stability of nanofluids include sedimentation analysis, zeta potential measurement, UV spectroscopy, dynamic light scattering (DLS), and electron microscopy techniques such as SEM and TEM. These techniques are widely employed to evaluate nanoparticle dispersion and overall stability in nanofluid systems.

4.1. Sedimentation and centrifugation

Sedimentation is a widely employed method for assessing the stability of nanofluids. This technique relies on the accumulation of sediment at the bottom of a liquid column as a result of gravitational forces. A longer duration for the nanofluid to develop a precipitate suggests enhanced stability. An alternative to this method is centrifugation, which offers a quicker evaluation of nanofluid stability. In centrifugation, the centrifugal force significantly exceeds the normal gravitational force, thereby accelerating the sedimentation process and allowing for faster results(Singh and Raykar 2008). Figure 1 provides a schematic representation of the stability evaluation method based on sedimentation.

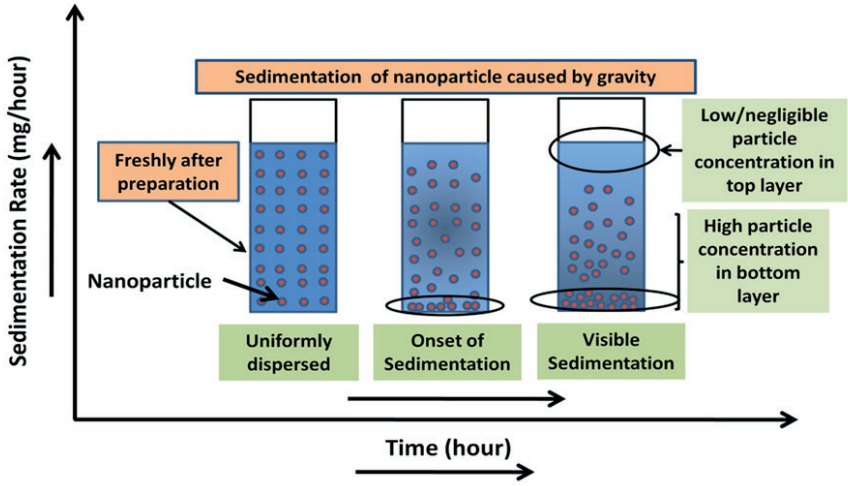

Fig.5. Sedimentation measurement (Chakraborty and Panigrahi 2020).

4.2. Zeta potential measurement

Zeta potential measures the electric potential at the surface of colloidal particles suspended in a liquid. Essentially, a higher zeta potential signifies enhanced stability and stronger repulsive forces between particles. Suspensions with a high zeta potential tend to be more stable due to this increased repulsion, preventing particles from aggregating. In contrast, suspensions with a low zeta potential have weaker repulsive forces, leading to

quicker aggregation and instability (Singh and Sood 2024). A stable nanofluid is characterized by a zeta potential greater than ±30 mV, regardless of whether it is positive or negative. This level of zeta potential reflects strong electrostatic interactions between nanoparticles, which helps maintain their dispersion and prevents aggregation (Mukesh Kumar, Palanisamy, and Vijayan 2020). Figure 5 illustrates the relationship between zeta potential values and pH levels across various stability regimes of nanofluids. Nanofluids are deemed stable when their zeta potential values are high, indicating strong repulsive forces that prevent particle aggregation. Conversely, when zeta potential values are low, as indicated in Figure 5, the nanofluids are classified as unstable, leading to potential clustering and sedimentation of the particles.

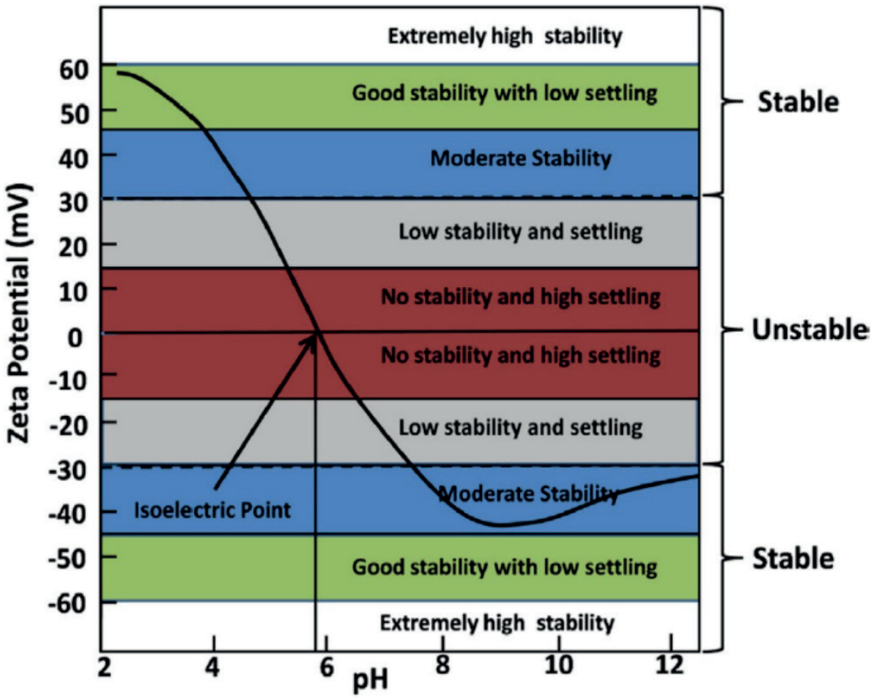

Fig. 5. Variation of zeta potential as a function of pH (Chakraborty and Panigrahi 2020).

4.3. UV spectroscopy

Ultraviolet-visible (UV-Vis) spectrophotometry is employed to evaluate the stability of nanofluids by analyzing the absorption characteristics of the solid phase within the wavelength range of 200 to 900 nm. This technique tracks changes in the sediment volume in the fluid over time, providing insights into the dispersion and stability of the nanoparticles suspended in the

nanofluid (Tavakoli et al. 2022). As sedimentation occurs, the volume of settled particles increases, which can lead to changes in the absorbance of the fluid. A stable nanofluid will show minimal variations in absorption, indicating that the nanoparticles remain well-dispersed. Conversely, significant changes in absorbance suggest instability, with particles aggregating and settling. This makes UV-Vis spectrophotometry a useful method for evaluating the stability and performance of nanofluids in various applications.

4.4. Dynamic light scattering (DLS)

Light scattering techniques are commonly employed to analyze dispersions, particularly to assess nanoparticle (NP) stability in suspensions. The presence of particle attractions can impact the stability of nanofluids (NFs), and tracking changes in particle size and distribution helps monitor particle aggregation. However, imaging methods like SEM or TEM, while useful for visualizing dried samples, do not accurately reflect the behavior of particles in fluid suspensions and are therefore unsuitable for studying nanoparticles in their natural state (Shima, Philip, and Raj 2015). Dynamic light scattering (DLS) collects scattered laser light to analyze particle behavior. This technique is based on the principle that particles in a liquid undergo random thermal motion, known as Brownian motion. The speed of this motion is influenced by particle size, with smaller, less dense particles moving faster than larger, denser ones. DLS measures the hydrodynamic diameter of particles by analyzing the intensity fluctuations in the scattered light. In contrast to imaging methods, DLS provides data for a larger volume of the sample, giving a more representative measurement of particle size (Ajeena, Víg, and Farkas 2022). The principle of Dynamic Light Scattering (DLS) involves directing a laser beam at particles suspended in a liquid as shown in Fig.6. A high-resolution detector then captures the intensity of the light scattered at a specific angle, θ. The intensity of the scattered light fluctuates over time as a result of the particles' Brownian motion, which reflects their random thermal movement in the suspension (Rodriguez-Loya, Lerma, and Gardea-Torresdey 2024).

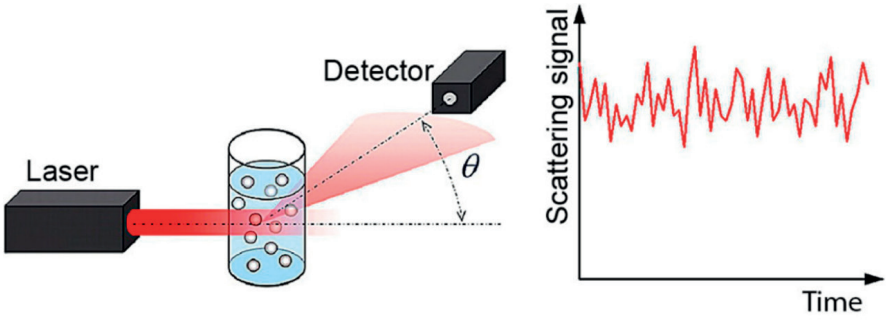

Fig.6. DLS principle of operation (Rodriguez-Loya et al. 2024).

4.5. Electron microscopy

Electron microscopy and light scattering are widely used methods for examining the stability of nanofluids by visualizing the distribution and aggregation of nanoparticles. The Transmission Electron Microscope (TEM) offers extremely high resolution, capable of reaching around 0.1 nm in lattice imaging. It produces digital images, referred to as electron micrographs. TEM allows for the direct observation of nanoparticle aggregation within nanofluids, providing detailed insights into their clustering and behavior in suspension (Mukherjee 2013).

5. Effect of stability in heat transfer applications

In many experimental studies, stability-enhancing methods have been applied considering the stability issue of nanofluids, and comparison data with the base fluid have been presented by measuring heat transfer coefficients. One of these studies experimentally investigated the stability and thermophysical properties of Aluminium Oxide (Al_2O_3) nanofluids in methanol. The stability was evaluated over time for various weight percentages (wt.%) of nanoparticles and surfactants, keeping the ratios consistent. Zeta potential measurements ranging from −44 to −64 mV were recorded for Al_2O_3–methanol nanofluids with three different surfactants. Notably, the use of CTAB as a surfactant provided stability for up to 6 months in Al_2O_3–methanol nanofluids (Mostafizur, Rasul, and Nabi 2022). Chakraborty et al. found that incorporating SDS into Cu-Zn-Al LDH nanofluids enhances the zeta potential, indicating improved stability, while also increasing the thermal conductivity (Chakraborty et al. 2019). Li et al. investigated the impact of pH adjustment and surfactant addition on the stability and thermal conductivity of Cu-H2O nanofluids. Their findings showed that as the pH increases from 3 to 9.5, the zeta potential value increases, resulting in improved stability (Su et al. 2016). In another study, Sarafraz et al. investigated the thermal performance of COOH-functionalized CNT-water nanofluids in a heat exchanger and reported that Nonylphenol ethoxylate (NPE) provided stable performance over a period of 21 days (Sarafraz, Hormozi, and Nikkhah 2016). The stability of water-based graphene nanoplatelets (GNP) nanofluids was evaluated using four different surfactants: sodium dodecyl benzene sulfonate (SDBS), sodium dodecyl sulfate (SDS), cetyl trimethylammonium bromide (CTAB), and gum arabic (GA). GNPs were dispersed in distilled water with the aid of an ultrasonication probe. Various analytical techniques, including UV-vis spectrometry, zeta potential measurements, particle size analysis, and Transmission Electron Microscopy (TEM), were employed to assess and characterize the stability of the nanofluids. Among the samples, the GNPs dispersed with SDBS after 60 minutes of ultrasonication (1–1 ratio) demonstrated the highest stability (Sarsam et al. 2016). In the other study, the stability of Al2O3/water nanofluid was evaluated using zeta potential analysis

and visual inspection. The study explored the influence of pH levels and sonication duration on the nanofluid's stability, with sodium dodecyl sulfate serving as the surfactant. Results showed that the zeta potential was greater at both the acidic and basic extremes of the pH scale for sonication times of 120 and 180 minutes. Additionally, it was found that the optimal sonication time, where maximum stability is achieved, increased as the concentration of the nanofluids increase (Choudhary et al. 2017).

6. Conclusion

Nanofluids, which consist of nanoparticles dispersed in base fluids, have attracted significant interest due to their ability to improve heat transfer and other properties in various applications. The stability of nanofluids is a crucial factor that influences their effectiveness, as instability can lead to issues like sedimentation, particle aggregation, or system clogging, diminishing performance. The stability of nanofluids depends on several factors, including particle concentration, surfactants, ultrasonication, pH, temperature, and particle size. Techniques such as adding surfactants, controlling pH, and optimizing ultrasonication parameters have been shown to enhance stability. However, long-term stability and the effects of temperature fluctuations in real-world applications remain areas of active research. The inclusion of surfactants or dispersants greatly increases the stability of nanofluids by preventing the aggregation of nanoparticles and maintaining their uniform distribution. Ultrasonication is commonly employed to disperse nanoparticle agglomerates and achieve uniform distribution in nanofluids. However, to avoid potential nanoparticle damage or excessive temperature rise, it's essential to carefully control both the duration and intensity of the process for optimal results. The pH of a nanofluid is a key factor in maintaining stability, as it affects the surface charge of nanoparticles and their interactions. By adjusting the pH to specific levels, electrostatic repulsion between particles can be enhanced, reducing the likelihood of aggregation. Ensuring long-term stability is a persistent challenge, particularly for nanofluids used in industrial applications. Research indicates that although certain nanofluids remain stable for weeks or even months, problems such as sedimentation and aggregation tend to arise over time, highlighting the need for further advancements in stabilization methods.

REFERENCES

Ajeena, Ahmed M., Piroska Víg, and Istvan Farkas. 2022. "A Comprehensive Analysis of Nanofluids and Their Practical Applications for Flat Plate Solar Collectors: Fundamentals, Thermophysical Properties, Stability, and Difficulties." *Energy Reports* 8:4461–90. doi: 10.1016/j.egyr.2022.03.088.

Babita, S. K. Sharma, and Shipra Mital Gupta. 2016. "Preparation and Evaluation of Stable Nanofluids for Heat Transfer Application: A Review." *Experimental Thermal and Fluid Science* 79:202–12. doi: 10.1016/j.expthermflusci.2016.06.029.

Chakraborty, Samarshi, and Pradipta Kumar Panigrahi. 2020. "Stability of Nanofluid: A Review." *Applied Thermal Engineering* 174(December 2019). doi: 10.1016/j.applthermaleng.2020.115259.

Chakraborty, Samarshi, Iman Sengupta, Ishita Sarkar, Surjya K. Pal, and Sudipto Chakraborty. 2019. "Effect of Surfactant on Thermo-Physical Properties and Spray Cooling Heat Transfer Performance of Cu-Zn-Al LDH Nanofluid." *Applied Clay Science* 168(September 2018):43–55. doi: 10.1016/j.clay.2018.10.018.

Choudhary, Rajesh, Deepak Khurana, Aditya Kumar, and Sudhakar Subudhi. 2017. "Stability Analysis of Al2O3/Water Nanofluids." *Journal of Experimental Nanoscience* 12(1):140–51. doi: 10.1080/17458080.2017.1285445.

Kamalgharibi, M., F. Hormozi, Seyed Amir Hossein Zamzamian, and M. M. Sarafraz. 2016. "Experimental Studies on the Stability of CuO Nanoparticles Dispersed in Different Base Fluids: Influence of Stirring, Sonication and Surface Active Agents." *Heat and Mass Transfer/Waerme- Und Stoffuebertragung* 52(1):55–62. doi: 10.1007/s00231-015-1618-z.

Kumar, L. Harish, S. N. Kazi, H. H. Masjuki, and M. N. M. Zubir. 2022. "A Review of Recent Advances in Green Nanofluids and Their Application in Thermal Systems." *Chemical Engineering Journal* 429(August 2021):132321. doi: 10.1016/j.cej.2021.132321.

Mehta, Bhavin, Dattatraya Subhedar, Hitesh Panchal, and Zafar Said. 2022. "Synthesis, Stability, Thermophysical Properties and Heat Transfer Applications of Nanofluid – A Review." *Journal of Molecular Liquids* 364:120034. doi: 10.1016/j.molliq.2022.120034.

Mostafizur, R. M., M. G. Rasul, and M. N. Nabi. 2022. "Effect of Surfactant on Stability, Thermal Conductivity, and Viscosity of Aluminium Oxide–Methanol Nanofluids for Heat Transfer Applications." *Thermal Science and Engineering Progress* 31(April):101302. doi: 10.1016/j.tsep.2022.101302.

Mukesh Kumar, P. C., K. Palanisamy, and V. Vijayan. 2020. "Stability Analysis of Heat Transfer Hybrid/Water Nanofluids." *Materials Today: Proceedings* 21:708–12. doi: 10.1016/j.matpr.2019.06.743.

Mukherjee, Sayantan. 2013. "Preparation and Stability of Nanofluids-A Review." *IOSR Journal of Mechanical and Civil Engineering* 9(2):63–69. doi: 10.9790/1684-0926369.

Ouikhalfan, Mohammed, Abdelouhab Labihi, Mohamed Belaqziz, Hassan Chehouani, Brahim Benhamou, Ahmet Sarı, and Ahmed Belfkira. 2020. "Stability and Thermal Conductivity Enhancement of Aqueous Nanofluid Based on Surfactant-Modified TiO2." *Journal of Dispersion Science and Technology* 41(3):374–82. doi: 10.1080/01932691.2019.1578665.

Rabby, Md Insiat Islam, Md Wasi Uddin, N. M. S. Hassan, Maglub Al Nur, Rokib Uddin, Sadman Istiaque, and Md Mirazul Mahmud Abir. 2024. "Recent Progresses in Tri-Hybrid Nanofluids: A Comprehensive Review on Preparation, Stability, Thermo-Hydraulic Properties, and Applications." *Journal of Molecular Liquids* 408(June):125257. doi: 10.1016/j.molliq.2024.125257.

Rodriguez-Loya, Jesus, Maricarmen Lerma, and Jorge L. Gardea-Torresdey. 2024. "Dynamic Light Scattering and Its Application to Control Nanoparticle Aggregation in Colloidal Systems: A Review." *Micromachines* 15(1). doi: 10.3390/mi15010024.

Sajid, Muhammad Usman, and Yusuf Bicer. 2022. "Impacts of Ultrasonication Time and Surfactants on Stability and Optical Properties of CuO, Fe3O4, and CNTs/Water Nanofluids for Spectrum Selective Applications." *Ultrasonics Sonochemistry* 88(June):106079. doi: 10.1016/j.ultsonch.2022.106079.

Sarafraz, M. M., F. Hormozi, and V. Nikkhah. 2016. "Thermal Performance of a Counter-Current Double Pipe Heat Exchanger Working with COOH-CNT/Water Nanofluids." *Experimental Thermal and Fluid Science* 78:41–49. doi: 10.1016/j.expthermflusci.2016.05.014.

Sarsam, Wail Sami, Ahmad Amiri, S. N. Kazi, and A. Badarudin. 2016. "Stability and Thermophysical Properties of Non-Covalently Functionalized Graphene Nanoplatelets Nanofluids." *Energy Conversion and Management* 116:101–11. doi: 10.1016/j.enconman.2016.02.082.

Shima, P. D., John Philip, and Baldev Raj. 2015. "Proceedings of OCEANS'94." 1_1. doi: 10.1109/oceans.1994.363814.

Singh, Ashok K., and Vijay S. Raykar. 2008. "Microwave Synthesis of Silver Nanofluids with Polyvinylpyrrolidone (PVP) and Their Transport Properties." *Colloid and Polymer Science* 286(14–15):1667–73. doi: 10.1007/s00396-008-1932-9.

Singh, Bikram, and Shilpa Sood. 2024. "Hybrid Nanofluids Preparation, Thermo-Physical Properties, and Applications: A Review." *Hybrid Advances* 6(April):100192. doi: 10.1016/j.hybadv.2024.100192.

Su, Yu, Le Gong, Bi Li, Zhiqiang Liu, and Dandan Chen. 2016. "Performance Evaluation of Nanofluid MQL with Vegetable-Based Oil and Ester Oil as Base Fluids in Turning." *International Journal of Advanced Manufacturing Technology* 83(9–12):2083–89. doi: 10.1007/s00170-015-7730-x.

Tavakoli, Atefeh, Keivan Rahimi, Farzin Saghandali, Jason Scott, and Emma Lovell. 2022. "Nanofluid Preparation, Stability and Performance for CO2 Absorption and Desorption Enhancement: A Review." *Journal of Environmental Management* 313(April):114955. doi: 10.1016/j.jenvman.2022.114955.

Urmi, Wajiha Tasnim, M. M. Rahman, K. Kadirgama, D. Ramasamy, and M. A. Maleque. 2020. "An Overview on Synthesis, Stability, Opportunities and Challenges of Nanofluids." *Materials Today: Proceedings* 41:30–37. doi: 10.1016/j.matpr.2020.10.998.

Wang, Jin, Xian Yang, Jiří Jaromír Klemeš, Ke Tian, Ting Ma, and Bengt Sunden. 2023. "A Review on Nanofluid Stability: Preparation and Application." *Renewable and Sustainable Energy Reviews* 188(September). doi: 10.1016/j.rser.2023.113854.

Yu, Wei, and Huaqing Xie. 2012. "A Review on Nanofluids: Preparation, Stability Mechanisms, and Applications." *Journal of Nanomaterials* 2012. doi: 10.1155/2012/435873.